



Universitat Autònoma de Barcelona

**ADVERTIMENT.** L'accés als continguts d'aquesta tesi queda condicionat a l'acceptació de les condicions d'ús establertes per la següent llicència Creative Commons:  [http://cat.creativecommons.org/?page\\_id=184](http://cat.creativecommons.org/?page_id=184)

**ADVERTENCIA.** El acceso a los contenidos de esta tesis queda condicionado a la aceptación de las condiciones de uso establecidas por la siguiente licencia Creative Commons:  <http://es.creativecommons.org/blog/licencias/>

**WARNING.** The access to the contents of this doctoral thesis it is limited to the acceptance of the use conditions set by the following Creative Commons license:  <https://creativecommons.org/licenses/?lang=en>



# **Molecular Modeling of Encapsulation and Catalysis in Supramolecular Metallocages**

Academic dissertation for the Degree of Doctor of Philosophy  
in Chemistry at Autonomous University of Barcelona

Gantulga Norjmaa

December 2021





# **Molecular Modeling of Encapsulation and Catalysis in Supramolecular Metallocages**

Gantulga Norjmaa

Prof. Jean-Didier Maréchal

Prof. Gregori Ujaque Pérez

December 2021



## **Acknowledgements**

First of all, my sincere thanks go to my supervisors Prof. Jean-Didier Maréchal and Prof. Gregori Ujaque Pérez. I am deeply grateful for all your support and guidance during the last four years.

I would like to thank to Prof. Agustí Lledós for his valuable advice and insightful comments during my Ph.D study.

My gratitude extends to all former and present members of the InSiliChem and computational BioNanoCat for encouraging and helping me in all the time of my academic research and daily life.

I also want to thank to Prof. Fahmi Himo for his advice and guidance during my short-term stay in his research group and Dr. Pietro Vidossich for his advice and guidance.

I would like to express my sincere gratitude to the UAB-PIF scholarship for the financial support.



## Abbreviations

APR	Attach-Pull-Release approach
COM	Center of mass
CC	Coupled cluster
CCSD(T)	Coupled cluster singles and doubles including perturbative triples
CI	Configuration interaction
B3LYP	Becke's three-parameter functional with LYP correlation
DFT	Density functional theory
DFT-D3	Density functional theory corrected with Grimme's dispersion corrections
ES	Enzyme-substrate complex
HF	Hartree-Fock
LYP	Lee, Yang and Parr, referring to the correlation functional developed by those authors
MEP	Molecular electrostatic potential
MCPB	Metal center parameter builder
MM	Molecular mechanics
MD	Molecular dynamics
MO	Molecular orbital
QM	Quantum mechanics
QM/MM	Quantum mechanics/molecular mechanics
PMF	Potential of mean force
PCM	Polarizable continuum method
RESP	Restrained electrostatic potential
RRHO	Rigid-rotor harmonic-oscillator model
SAS	Solvent accessible surface
SCF	Self-consistent field
SDD	Stuttgart Dresden pseudopotentials and basis sets
SES	Solvent excluded surface
SMD	Solvation model based on the solute electron density
SOC	Supramolecular organometallic cage
TS	Transition state
WHAM	Weighted histogram analysis method





## List of publications

- I. Microsolvation and Encapsulation Effects on Supramolecular Catalysis: C–C Reductive Elimination inside [Ga<sub>4</sub>L<sub>6</sub>]<sup>12-</sup> Metallocage.**  
Gantulga Norjmaa, Jean-Didier Maréchal, Gregori Ujaque  
*J. Am. Chem. Soc.* **2019**, *141*, 13114–13123.
- II. Reaction Rate Inside the Cavity of [Ga<sub>4</sub>L<sub>6</sub>]<sup>12-</sup> Supramolecular Metallocage is Regulated by the Encapsulated Solvent.**  
Gantulga Norjmaa, Jean-Didier Maréchal, Gregori Ujaque  
*Chem. Eur. J.* **2020**, *26*, 6988-6992.
- III. Modeling Kinetics and Thermodynamics of Guest Encapsulation into the [M<sub>4</sub>L<sub>6</sub>]<sup>12-</sup> Supramolecular Organometallic Cage.**  
Gantulga Norjmaa, Pietro Vidossich, Jean-Didier Maréchal, Gregori Ujaque  
*J. Chem. Inf. Model.* **2021**, *61*, 4370-4381.
- IV. Origin of the Rate Acceleration in the C-C Reductive Elimination from Pt(IV)-complex in a [Ga<sub>4</sub>L<sub>6</sub>]<sup>12-</sup> Supramolecular Metallocage.**  
Gantulga Norjmaa, Jean-Didier Maréchal, Gregori Ujaque  
*Chem. Eur. J.* **2021**, in press.
- V. Enzymelike Acceleration in the Nazarov Cyclization by a [Ga<sub>4</sub>L<sub>6</sub>]<sup>12-</sup> Supramolecular Organometallic Cage: the Basicity of Complexed Alcohol is Key.**  
Gantulga Norjmaa, Fahmi Himo, Jean-Didier Maréchal, Gregori Ujaque  
*Manuscript*



# Contents

Acknowledgements .....	v
Abbreviations .....	vii
List of publications .....	ix

## CHAPTER 1. General introduction.

1.1 Introduction to supramolecular chemistry .....	1
1.2 Noncovalent interactions in supramolecular chemistry .....	3
1.3 Supramolecular Organometallic Cages (SOC) .....	5
1.4 Encapsulation process and host-guest binding .....	9
1.5 Introduction to supramolecular catalysis .....	11
1.6 Reactivity by encapsulation in SOCs .....	14
1.7 $K_{12}[Ga_4L_6]$ supramolecular organometallic cage .....	17
1.8 Encapsulation by the $[Ga_4L_6]^{12-}$ .....	19
References .....	21

## CHAPTER 2. Theories and methods.

2.1 Computing Energy .....	27
2.1.1. Quantum Mechanics .....	27
2.1.2. Molecular Mechanics .....	36
2.1.3. QM/MM .....	39
2.2 Exploring the Conformational Space .....	42
2.2.1. Introduction .....	42
2.2.2. Molecular Dynamics .....	43
2.3 Specific Additional Aspects for Host-Guest Systems .....	47
2.3.1. Calculating cavity volumes .....	47
2.3.2. Counting the number of solvent molecules embedded .....	48
References .....	50

**CHAPTER 3. Objectives. ....56**

**CHAPTER 4. Cationic guest encapsulation by the [Ga<sub>4</sub>L<sub>6</sub>]<sup>12-</sup>.**

4.1 Force field parametrization .....	59
4.2 Assessing the force field parametrization .....	62
4.3 Modeling the encapsulation of NEt <sub>4</sub> <sup>+</sup> by [Ga <sub>4</sub> L <sub>6</sub> ] <sup>12-</sup> .....	64
References .....	68
Publication .....	69

**CHAPTER 5. C-C reductive eliminations catalyzed by the [Ga<sub>4</sub>L<sub>6</sub>]<sup>12-</sup>.**

5.1 Reductive eliminations from (Et <sub>3</sub> P)(I)Au <sup>III</sup> (CH <sub>3</sub> ) <sub>2</sub> complex	
5.1.1. Reaction in solution .....	72
5.1.2. Reaction in the [Ga <sub>4</sub> L <sub>6</sub> ] <sup>12-</sup> .....	73
5.1.3. Origin of the catalysis .....	76
5.2 Reductive eliminations from (Me <sub>3</sub> P)(I)Au <sup>III</sup> (CH <sub>3</sub> ) <sub>2</sub> complex	
5.1.1. Reaction in solution .....	78
5.1.2. Reaction in the [Ga <sub>4</sub> L <sub>6</sub> ] <sup>12-</sup> .....	79
5.1.3. Origin of the catalysis and effect of ligand size .....	79
5.3 Reductive eliminations from (Me <sub>3</sub> P)(I)Pt <sup>IV</sup> (CH <sub>3</sub> ) <sub>2</sub> complex	
5.1.1. Reaction in solution .....	81
5.1.2. Reaction in the [Ga <sub>4</sub> L <sub>6</sub> ] <sup>12-</sup> .....	82
5.1.3. Origin of the catalysis and effect of metal ion .....	83
References .....	85
Publications .....	87

**CHAPTER 6. The Nazarov cyclization catalyzed by the [Ga<sub>4</sub>L<sub>6</sub>]<sup>12-</sup>.**

6.1 Reaction in solution .....	91
6.2 Reaction in the [Ga <sub>4</sub> L <sub>6</sub> ] <sup>12-</sup> .....	93
6.3 Origin of the catalysis and effects of encapsulation .....	96
References .....	99

<b>CHAPTER 7. General conclusions. ....</b>	<b>101</b>
---	------------



# Chapter 1.

## General introduction.

Nature embodies a diverse range of intricate complexities. From a molecular point of view, such complexities originate from intra- and intermolecular bonding networks. For the latter, shape comes into play in addition to size. The intermolecular interaction based on both size and shape complementarities can be either unique or highly specific. A perfect example of this in nature is a formation of an enzyme-substrate complex in which the substrate (guest) is hosted by the enzyme for a specific chemical transformation. These transformations are more than million times faster than the one without the enzyme.<sup>1-3</sup> The development of “enzyme-like” molecular entities is thus one of the main directions in the field of catalysis. In this direction, several supramolecular host environments have been succeeded over the last few decades, indicating a promising and emerging role of supramolecular chemistry inspired by nature.<sup>4-13</sup>

### 1.1. Introduction to supramolecular chemistry.

The term “supramolecule” (übermolekül in German) appeared in the literature for the first time in 1937 by Karl Lothar Wolf and coworkers to describe the intermolecular interaction of dimers such as hydrogen bonded carboxylic acid dimers.<sup>14</sup> An enzyme-substrate complex (ES) forms when an enzyme binds its specific substrate, is a unique example of supramolecular complexation driven by nature. From the introduction of the “übermolekül” term to the first definition of supramolecular chemistry by Jean-Marie Lehn, it took more than 40 years.<sup>15</sup> In 1978, Jean-Marie Lehn described the field of supramolecular chemistry as the “chemistry of molecular assemblies and of the intermolecular bonds”.<sup>16</sup> One of the reasons why it took more than 40 years to Lehn’s definition of supramolecular chemistry from the introduction of the term “übermolekül” is that the importance of the environment for the properties of a molecule was revealed with an increasing number of examples in the late 1960s.<sup>17</sup>



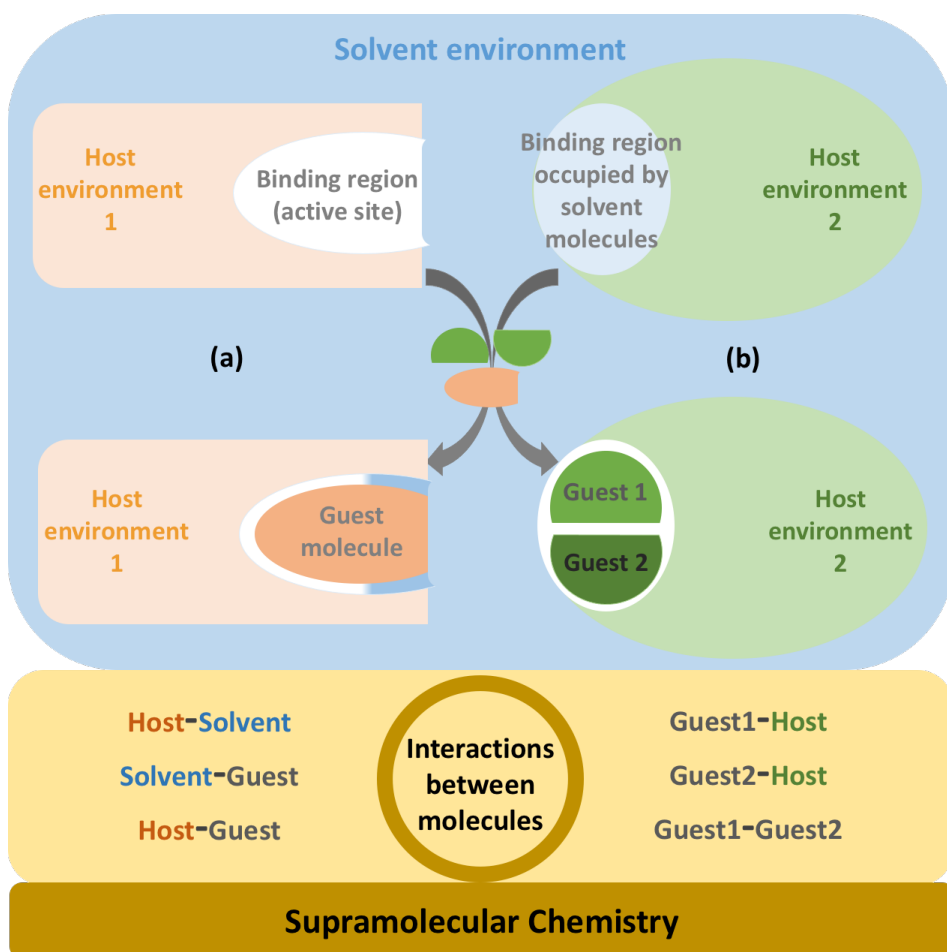


**Figure 1.1.** General schematic illustrations for forming supramolecular host-guest systems.

In a simple way, we could say that a supramolecular system consists of at least two molecules. In general, one of the two molecules provides a comfortable environment for the other under a certain range of conditions which is called a host and the other is called a guest during a host-guest binding event. The comfortable environment provided by the host for the guest is usually called a binding region (binding site) of the host. For the natural enzymes, their binding sites have a very specific size, shape, and chemical behavior which leads to the enzyme-substrate specificity.

However, this enzyme-substrate bonding specificity can be expanded for a self-assembled or a synthetic host to which many different guest molecules could bind, it is clear that there is no universal host for all guest molecules. The interaction between the host and the guest, and/or their size and shape complementarity play important roles in host-guest chemistry. Two schematic examples are illustrated in Figure 1.1. The number of guest molecules needed to form a specific supramolecular host-guest system depends on the nature of the binding region of the host environment, one (Figure 1.1a), two (Figure 1.1b), three, etc. The binding region of the host can be occupied by solvent molecules before binding of the guest molecule in a solvent environment. The solvent molecules in the binding region of the host not only could play significant roles in molecular processes but they also could behave differently than the ones in the bulk solvent due to the environmental change. When the specific guest molecule binds to the host, those solvent molecules in the binding region of the host are replaced by the guest and merged into the bulk solvent (Figure 1.1b). It is also possible to find the solvent molecules with the guest molecule in the binding region of the host (Figure 1.1a).

## **1.2. Noncovalent interactions in supramolecular chemistry.**

The intermolecular driving forces that form supramolecular systems are usually the attractive noncovalent interactions. The most common types of these interactions in the field of supramolecular chemistry are presented in Figure 1.2.

- Electrostatic interactions are considered as the strongest among them, can be classified into three sub-types: ion-ion, ion-dipole, and dipole-dipole. Bond energies of the ion-ion interactions range from ca. 100 kJ/mol to 350 kJ/mol.

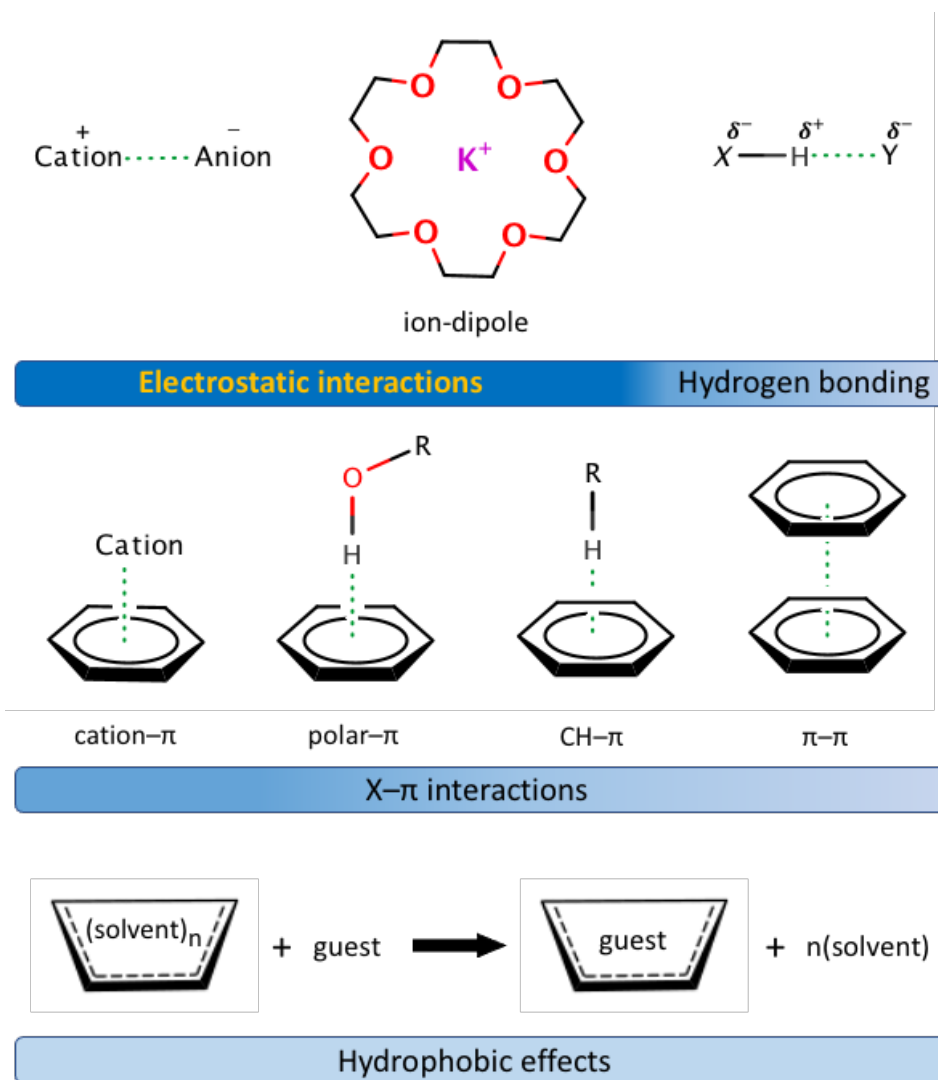


**Figure 1.2.** Common attractive noncovalent interactions in supramolecular chemistry.

- The ion-dipole interactions are somewhat weaker than the ion-ion interactions, with the range of ca. 50 kJ/mol to 200 kJ/mol, while the dipole-dipole interactions are even weaker than the ion-dipole forces (5 kJ/mol to 50 kJ/mol).<sup>17</sup>
- Hydrogen bonding is a special case of the dipole-dipole attractive interaction, involves a hydrogen atom covalently bonded to a more

electronegative atom. It can also be classified as follows: strong hydrogen bonds (60 kJ/mol to 120 kJ/mol), moderate hydrogen bonds (15 kJ/mol-60 kJ/mol), and weak hydrogen bonds (less than 15 kJ/mol).

- $\pi$ -systems are considered as an important part of both chemical and biological recognition.<sup>18</sup> They have also been employed in artificial supramolecules. The electron rich  $\pi$ -systems can interact with a cation, an anion, and a neutral species. Some common attractive interactions involving the  $\pi$ -systems (X- $\pi$  interactions) are shown in Figure 1.2. The cation- $\pi$  type is the strongest among the X- $\pi$  interactions (ca. 5 kJ/mol to 80 kJ/mol).<sup>19</sup>
- Hydrophobic effect can also be one of the driving forces for forming supramolecular systems. For example, in general, nonpolar guest molecules are better fit than polar solvent molecules for a supramolecular host with a hydrophobic binding region.
- Van der Waals forces (less than 5 kJ/mol) are found on the weak end of noncovalent forces. Despite being the weakest among the noncovalent interactions, it can play a fundamental role in many fields.

### 1.3. Supramolecular Organometallic Cages (SOC).

Using the attractive noncovalent forces, chemists have synthesized many supramolecular hosts and host-guest complexes which can be included in the type of inclusion compound.<sup>20</sup> The first type of inclusion compounds, zeolites, were reported by Axel Fredrik Cronstedt in 1756.<sup>21</sup> Whereas the first type of supramolecular hosts applied successfully in catalysis, cyclodextrins, were first described in 1891 by Antoine Villiers,<sup>22</sup> and its successful application to catalysis was reported as an “artificial enzyme” in 1970 by Ronald Breslow.<sup>23</sup>

Between 1967 and 1973, synthetic host environments for cation-binding, including crown ethers by Charles John Pederson in 1967, cryptands by Jean-Marie Lehn in 1969, and spherands by Donald James Cram in 1973 were designed and developed.<sup>24-26</sup> They received jointly the Nobel Prize

in Chemistry “for their development and use of molecules with structure-specific interactions of high selectivity” in 1987.

Supramolecular organometallic cages (SOCs) represent one of the most important developments in host design. They are usually synthesized from organic linkers and metal ions in solution. Some examples of the organic linkers and the metal ions are presented in Figure 1.3.

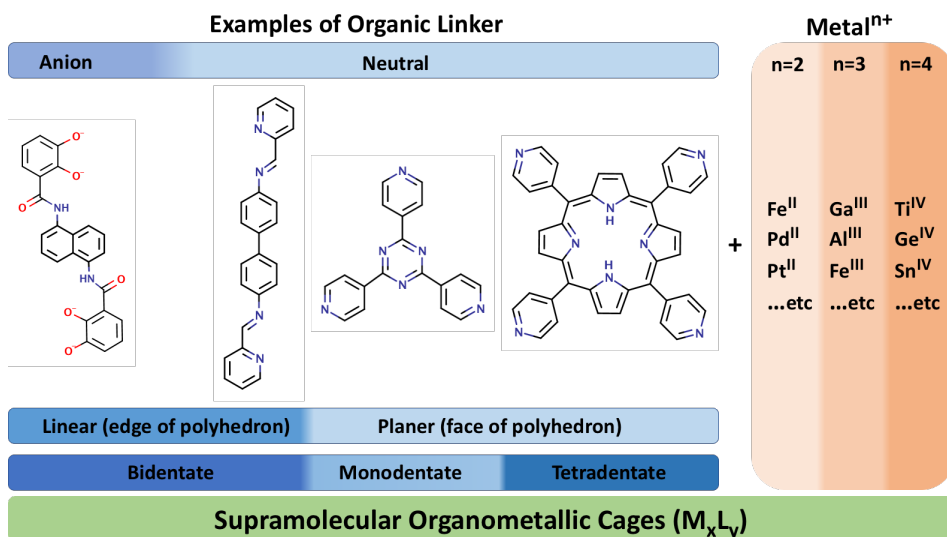


**Figure 1.3.** Examples of organic linkers and metal ions of supramolecular organometallic cages.

The organic linkers of the supramolecular organometallic cages can be anionic and/or neutral compounds. They also can be monodentates or polydentates.

Synthesis of supramolecular organometallic cages have been developed from the simplest regular polyhedron (examples include 10 components, 4 metal ions and 6 organic linkers) to complex Goldberg polyhedrons (examples include up to 144 small components).<sup>27</sup>

In a family of supramolecular organometallic cages, Platonic polyhedrons are the most common geometrical shapes, which are tetrahedron, octahedron, cube, dodecahedron, and icosahedron. Examples of these Platonic polyhedron SOC are illustrated in Figure 1.4.

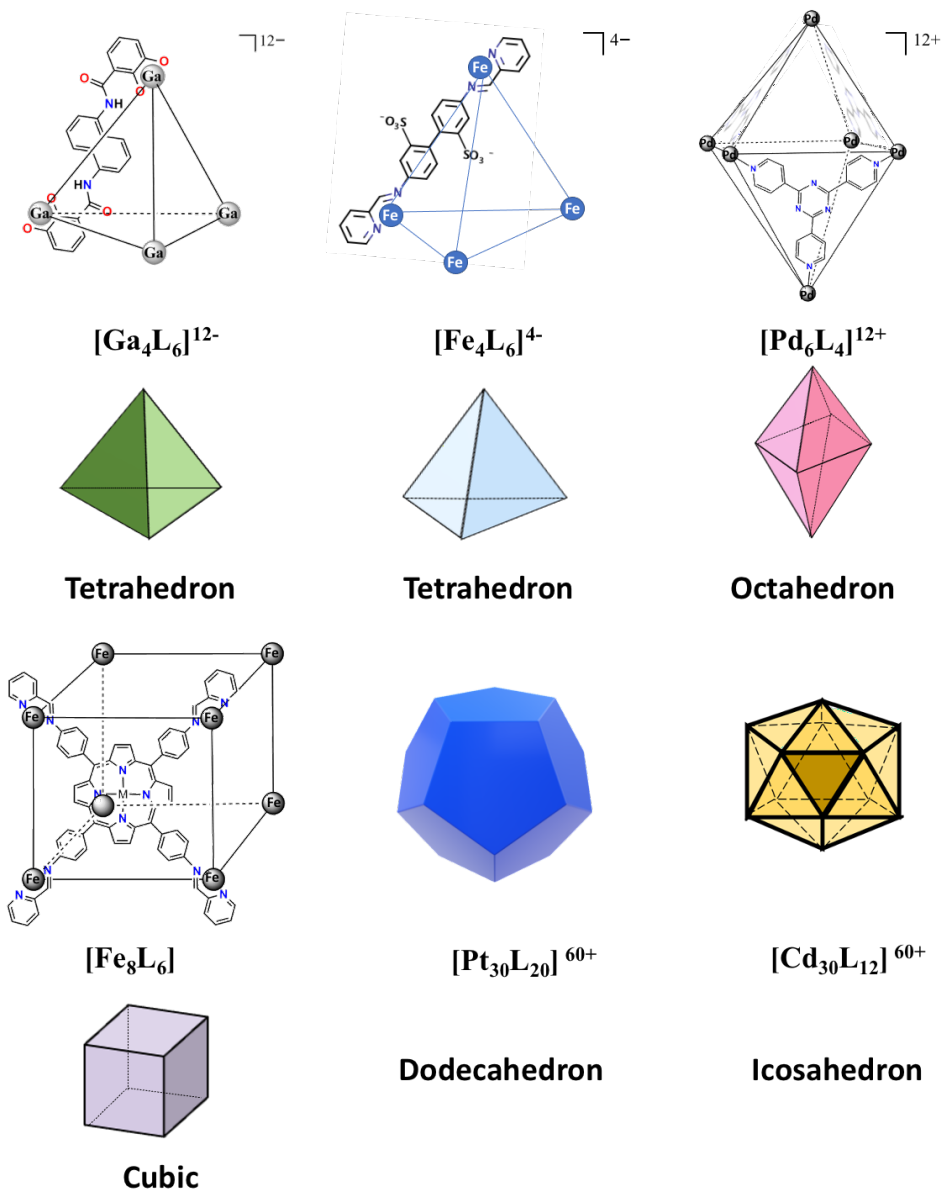


**Figure 1.4.** Examples of Platonic polyhedron supramolecular organometallic cages.

If the organic linkers are relatively linear, the number of the organic linkers forming a tetrahedron SOC with metal ions should be the same as the number of the edges of a tetrahedron. For example, [Ga<sub>4</sub>L<sub>6</sub>]<sup>12-</sup> cages developed by the Raymond group or [Fe<sub>4</sub>L<sub>6</sub>]<sup>4-</sup> cages developed by the

Nitschke group are tetrahedron SOCs, containing the same number of organic linkers which is equal to the number of the edges of a tetrahedron; however, they are synthesized employing different organic linkers and different metal ions (Figure 1.4). If the organic linkers of the SOCs are relatively planar, they are usually in the faces of the polyhedrons. In this case, the number of the organic linkers does not have to be the same as the number of the edges or the faces of a polyhedron because a face of the polyhedron includes at least three edges and three vertices of the polyhedron. In other words, a planar organic linker is a link between at least three metal ions of a SOC. One example is a  $[\text{Pd}_6\text{L}_4]^{12+}$ , an octahedron SOC developed by the Fujita group. In this case, it consists of 6  $\text{Pd}^{2+}$  ions (6 vertices) and 4 neutral organic linkers (4 of 8 faces) because those four planar organic linkers are enough for twelve interpalladium links between six  $\text{Pd}^{2+}$  ions.

The geometries optimized with implicit solvation of the  $[\text{Ga}_4\text{L}_6]^{12-}$ , the  $[\text{Fe}_4\text{L}_6]^{4-}$ , and  $[\text{Pd}_6\text{L}_4]^{12+}$  SOCs are shown in Figure 1.5.

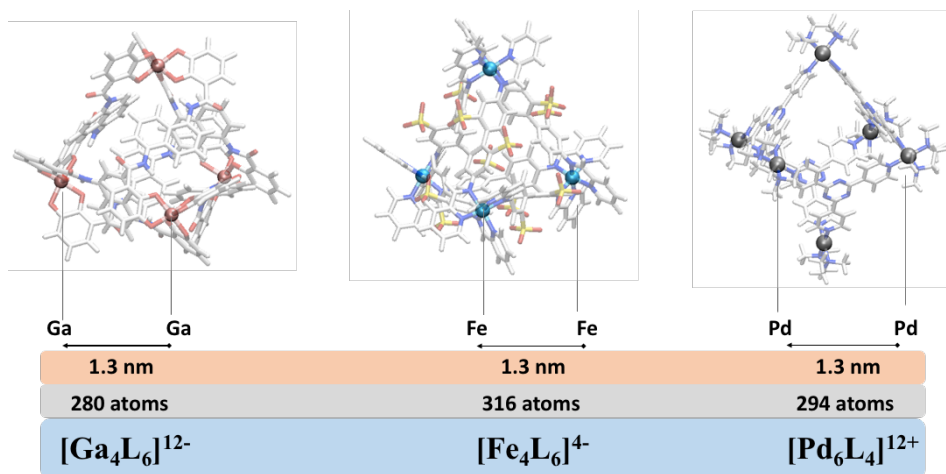


**Figure 1.5.** Optimized geometries of three Platonic polyhedron supramolecular organometallic cages at B3LYP-D3/SDD/SMD.

These supramolecular organometallic cages are formed from around 300 atoms and metal ion-metal ion distances are approximately 1.3 nm which indicates that it is a not only experimental but also computational challenge to deal with. But understanding their behaviors and abilities should lead to

potential applications in many fields such as molecular recognition, supramolecular catalysis, molecular architectures, etc.

#### 1.4. Encapsulation process and host-guest binding.

One of the fundamental properties of the supramolecular organometallic cages is encapsulation of other molecules. What kind of substrate do they encapsulate? and how do they encapsulate them? These are interesting questions, and it is clear that it depends on the nature of the supramolecular organometallic cage. The encapsulation of guest molecules into the host (guest-encapsulation) can be driven enthalpically and/or entropically in solution. A general schematic illustration of guest-encapsulation process is presented in Figure 1.6.

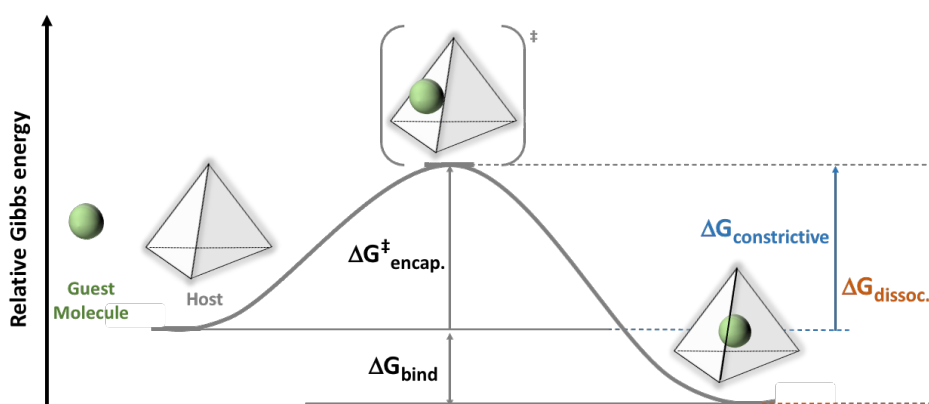


**Figure 1.6.** General encapsulation process.

Charged molecules can bind strongly to oppositely charged supramolecular organometallic cages, taking advantage of strong attractive electrostatic forces. While discussing host-guest bindings, it should not be forgotten that there can be a significant difference between two binding affinities obtained for different guest molecules with the same total charge. This implies that size and shape complementarities can be important for the stability of supramolecular host-guest complexes.

One factor that could lead to the entropy-driven host-guest binding is that in the guest-unbound state, where the guest molecule is far from the host in solution, the host contains a greater number of solvent molecules than



the number of guests. In this case, upon host-guest binding, more molecules (solvent molecules) are released from the host than it binds.

If a supramolecular organometallic cage is highly charged, such as a highly anionic  $[\text{Ga}_4\text{L}_6]^{12-}$  or a highly cationic  $[\text{Pd}_6\text{L}_4]^{12+}$  SOCs, more than one oppositely charged molecules and/or counter ions can bind on both: the outer surface, and inside the cavity of the supramolecular organometallic cage. The overall guest-encapsulation process can be generally described by two consecutive processes: (i) exterior association in which the guest molecule interacts with the outside of the supramolecular organometallic cage, forming an ion-pair complex state, and (ii) encapsulation in which the guest molecule enters to the inside the supramolecular organometallic cage, forming a guest-encapsulated state in solution. It was proposed as a guest dissociation mechanism, based on experimental observations for a host-guest complex,  $\text{Cp}^*(\text{PMe}_3)\text{Ir}(\text{Me})(\text{cis-2-butene})^+[\text{Ga}_4\text{L}_6]^{12-}$ .<sup>28</sup> A schematic representation of this process in the direction of encapsulation is shown in Figure 1.7.

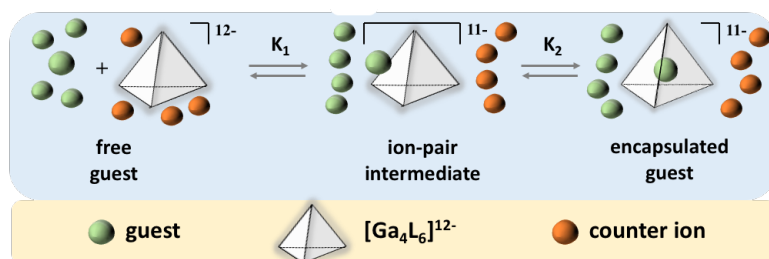


**Figure 1.7.** Example of exterior (exterior association) and interior binding (encapsulation) into highly charged SOC,  $[\text{Ga}_4\text{L}_6]^{12-}$ , adapted from refs 28 and 29.

Interestingly, in the presence of an anionic trap (triphenylphosphine trisulfonate, TPPTS), the rate-determining step of this process is the ion-pair formation from the free guest state in solution ( $\text{TS}_{\text{ion-pair}}$ ), whereas in the presence of a neutral ligand (1,3,5-triaza-7-phosphaadamantane, PTA), it was proposed to be the encapsulation of the guest (ion-pair formation from the encapsulated guest).<sup>28</sup> This indicates that not only the nature of guest molecules but also the nature of other systems in solution can affect the Gibbs energy barriers of the process.

One of other interesting observations is that initial encapsulation of  $\text{NEt}_4^+$  by  $[\text{Ga}_4\text{L}_6]^{12-}$  is too fast for  $^1\text{H}$  NMR monitoring, whereas when a ratio between the host and the guest is 1:6, a Gibbs energy barrier of ca.18.2 kcal/mol was estimated for a guest self-exchange process of  $\text{NEt}_4^+$ - $[\text{Ga}_4\text{L}_6]^{12-}$  host-guest complex.<sup>29</sup> This shows that the Gibbs energy barrier for guest-encapsulation from the ion-pair intermediate can also be affected by the number of guest molecules in solution for this case. Despite these experimental observations, there is still a lack of computational studies to model these dynamic processes with a certain level of accuracy and to provide insights at molecular level. Therefore, the first part of the work described in this thesis is devoted to modelling the encapsulation by the supramolecular organometallic cage,  $[\text{Ga}_4\text{L}_6]^{12-}$ .

### **1.5. Introduction to supramolecular catalysis.**

Reaching an enzyme-like acceleration with synthetic environments is indeed a challenge. In general, natural enzymes accelerate specific chemical transformations at least a million times. The work reported by Breslow and Overman in 1970 was one of the first remarkable rate accelerations (up to  $10^9$ ) achieved by supramolecular host systems.<sup>23</sup> Successful applications of supramolecular host environments to catalysis are increasing. The term “supramolecular catalysis” was introduced to refer to a discipline bridging the gap between homogeneous catalysis and enzymatic catalysis (Figure 1.8).<sup>30</sup>

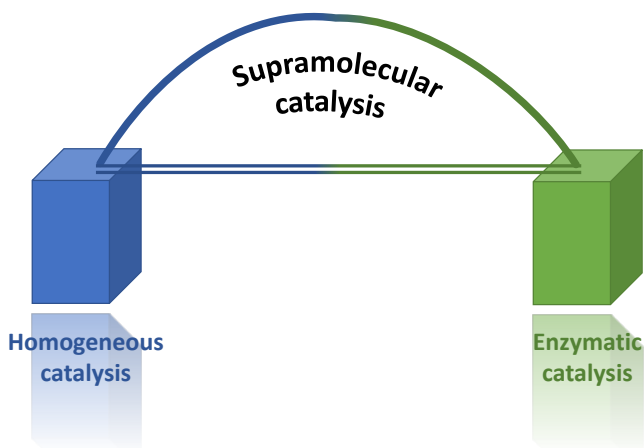


**Figure 1.8.** Supramolecular catalysis bridging homogeneous catalysis and enzymatic catalysis.

The relation between the reaction rate constant and the activation energy at certain temperature is given by the Arrhenius equation:

$$k = Ae^{-E_a/(RT)} \quad (\text{Eq.1.1})$$

where  $k$  is the rate constant,  $A$  is a factor,  $E_a$  is the activation energy,  $T$  is the temperature.

One can estimate the activation energy (the Gibbs energy barrier) from the rate constant obtained from experiments using the Eyring equation.

$$k = \frac{k_B T}{h} e^{-\Delta G^\ddagger/(RT)} \quad (\text{Eq.1.2})$$

where  $k_B$  is the Boltzmann constant,  $h$  is the Planck constant.

For single step reactions, the origin of a rate acceleration (or decrease in Gibbs energy barrier) observed by experiments can be classified as follows: (i) reactant destabilization, (ii) transition state (TS) stabilization, or (iii) both, reactant destabilization and TS stabilization (Figure 1.9a).

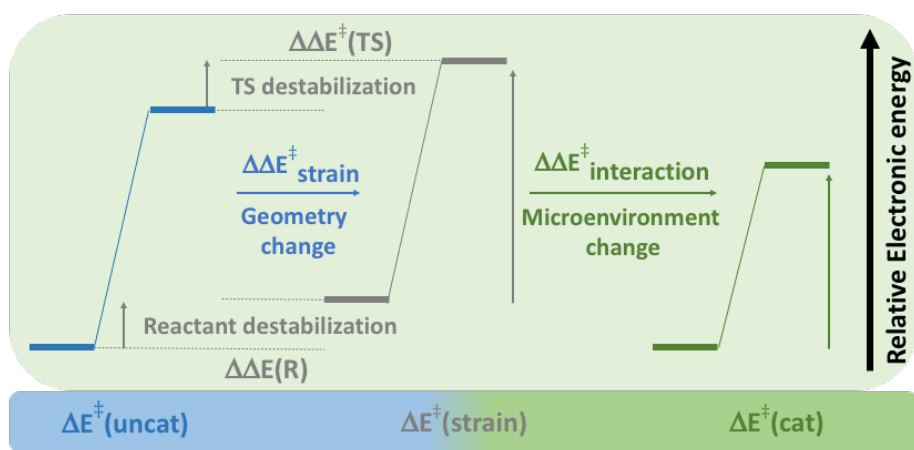
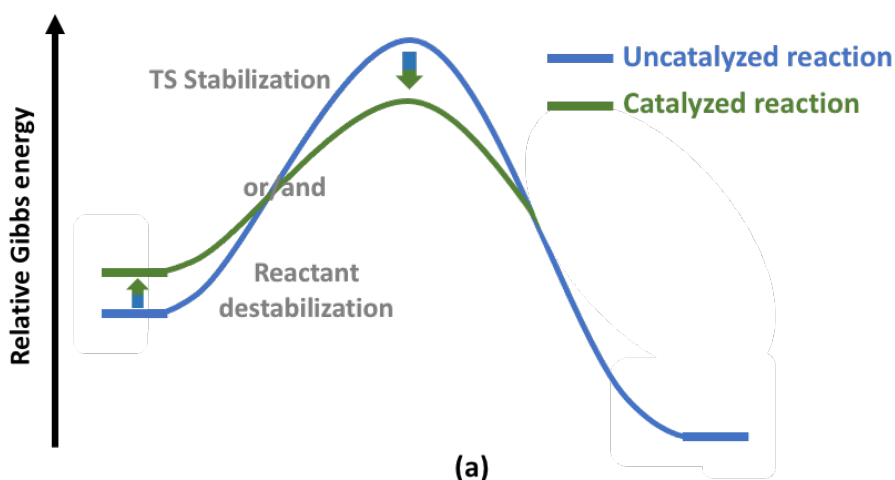


**Figure 1.9.** Examples (a) of catalyzed and uncatalyzed reaction profile, and (b) of analyzing the effects from supramolecular environments on energy barriers.

For multistep reactions, the effect from supramolecular environments can also be evaluated for every step of a reaction profile by comparing the catalyzed reaction with uncatalyzed reaction. This single-step comparison between the catalyzed and the uncatalyzed reactions can be further analyzed by separating the strain effect (geometry change of the reactant and the TS caused by supramolecular environments) from the interaction effect between the guest and the supramolecular environment

(Figure 1.9b). In general, the interaction term,  $\Delta\Delta E^\ddagger$ , is considered as a main contribution to rate accelerations in enzymatic catalysis.<sup>31</sup>

The supramolecular organometallic cages usually accelerate reactions by encapsulating and performing chemical transformations inside their cavity. Substrate-encapsulation is thus the first step of reactions catalyzed in supramolecular organometallic cages. More general examples are shown in Figure 1.10.

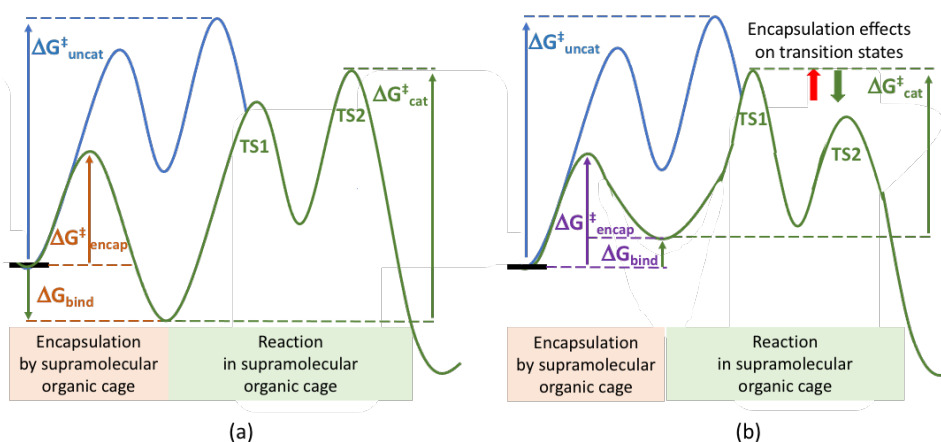


**Figure 1.10.** Examples of generic reaction profiles for uncatalyzed and catalyzed by supramolecular encapsulation processes. (a) spontaneous binding and stabilizations of transition states and (b) non-spontaneous binding and transition state stabilization and destabilization.

A variety of substrates (guest molecules) can be encapsulated in the supramolecular organometallic cages compared to the enzyme-substrate specificity. Therefore, binding Gibbs energies of distinct substrates in the same supramolecular organometallic cage can be very different. Two general cases are illustrated in Figure 1.10 (binding Gibbs energies,  $\Delta G_{\text{bind}}$ , in orange and in purple in encapsulation parts of generic reaction profiles). For multistep reactions, it is possible that every step of the reaction can be affected differently by encapsulation. Thus, there can be a modification of the rate-limiting steps of the reaction in solution and in the supramolecular organometallic cage (Figure 1.10b).

## 1.6. Reactivity by encapsulation in SOCs.

In the last two decades, supramolecular organometallic cages have been successfully applied for chemical reactions as molecular containers (molecular flasks or nanoreactors); they induce enhanced reactivity and improved selectivity in their confined environments.<sup>32–36</sup> Most of these achievements employed anionic or cationic supramolecular organometallic cages as a host. Some examples with anionic supramolecular organometallic cages are shown in Table 1.1.

**Table 1.1.** Examples of reactivity and selectivity in anionic SOC.<sup>7,37–50</sup>

	SOC	Proposed role of the SOC	Enhanced reactivity and/or selectivity	Reaction
Anionic	[Ga <sub>4</sub> L <sub>6</sub> ] <sup>12-</sup>	Stabilization	Rate acceleration up to 10 <sup>7</sup>	C-C reductive elimination by Au(III) and Pt(IV) <sup>37</sup>
	[Ga <sub>4</sub> L <sub>6</sub> ] <sup>12-</sup>	Stabilization	Rate acceleration up to 10 <sup>6</sup>	Nazarov cyclization <sup>7</sup>
	[Ga <sub>4</sub> L <sub>6</sub> ] <sup>12-</sup>	Stabilization	not observed in solution	Carbonyl-ene cyclization <sup>38</sup>
	[Ga <sub>4</sub> L <sub>6</sub> ] <sup>12-</sup>	Stabilization	Rate acceleration up to 10 <sup>5</sup>	Prins cyclization <sup>39</sup>
	[Ga <sub>4</sub> L <sub>6</sub> ] <sup>12-</sup>	Stabilization	not observed in solution	Aza-Prins cyclization <sup>40</sup>
	[Ga <sub>4</sub> L <sub>6</sub> ] <sup>12-</sup>	Stabilization	Rate acceleration up to 854	Aza-Cope <sup>41</sup>
	[Ga <sub>4</sub> L <sub>6</sub> ] <sup>12-</sup>	Stabilization	Rate acceleration up to 3900	Orthoformate hydrolysis <sup>42</sup>
	[Ga <sub>4</sub> L <sub>6</sub> ] <sup>12-</sup>	Stabilization	stereoselectivity up to 44:1	Aza-Darzens coupling <sup>43</sup>
	[Ga <sub>4</sub> L <sub>6</sub> ] <sup>12-</sup>	Catalyst encapsulation	site-selectivity up to 92% yield	Hydrogenations <sup>44</sup>
	[Ga <sub>4</sub> L <sub>6</sub> ] <sup>12-</sup>	Catalyst encapsulation	site-selectivity up to 95% yield	Allylic Alcohol Isomerization <sup>45</sup>
	[Ga <sub>4</sub> L <sub>6</sub> ] <sup>12-</sup>	Catalyst encapsulation	yield increase up to 41%	Hydroalkoxylation of allenes <sup>46</sup>
	[Ga <sub>4</sub> L <sub>6</sub> ] <sup>12-</sup>	Stabilization	yield increase up to 56% regio-selectivity up to 20:1	Pyridine-borane reductions <sup>47</sup>
	[Ga <sub>4</sub> L <sub>6</sub> ] <sup>12-</sup>	Stabilization	not observed in solution	Oxidative addition with Cu(I) and Pd(II) <sup>48</sup>
	[Fe <sub>4</sub> L <sub>6</sub> ] <sup>4-</sup>	Stabilization	yield increase up to 60%	Aldehyde reduction <sup>49</sup>
	[Fe <sub>4</sub> L <sub>6</sub> ] <sup>4-</sup>	Stabilization	yield increase up to 60%	Hydroxybutenolide to fumaraldehydic acid <sup>50</sup>

Among the anionic supramolecular organometallic cages, Raymond's [Ga<sub>4</sub>L<sub>6</sub>]<sup>12-</sup> and Nitschke's [Fe<sub>4</sub>L<sub>6</sub>]<sup>4-</sup> have already been applied successfully for chemical transformations by encapsulation.<sup>36,51</sup> Remarkably, enzyme-like rate accelerations have been reported for the carbon-carbon reductive

eliminations (rate acceleration up to  $10^7$ ) from high valent transition metal complexes ( $\text{Au}^{\text{III}}$  and  $\text{Pt}^{\text{IV}}$ ) and for the Nazarov cyclization of 1,4-pentadien-3-ols (rate acceleration up to  $10^6$ ) inside the  $[\text{Ga}_4\text{L}_6]^{12-}$  supramolecular organometallic cage.<sup>7,37</sup> The origins of these two rate accelerations are investigated computationally in Chapter 5 and Chapter 6 of this thesis. Understanding the origin of these rate accelerations should help for the development of host-guest catalysis.

Compared to the number of the anionic supramolecular organometallic cages already successfully used in host-guest catalysis, the number of cationic supramolecular organometallic cages is significantly greater, and some examples are shown in Table 1.2.

**Table 1.2.** Examples of reactivity and selectivity in cationic SOC.<sup>8,11,52–62</sup>

	SOC	Proposed role of the SOC	Enhanced reactivity and/or selectivity	Reaction
<b>Cationic</b>	$[\text{Pd}_6\text{L}_4]^{12+}$	Pre-organization	not observed in solution	Naphthalene Diels-Alder <sup>8</sup>
	$[\text{Pd}_6\text{L}_4]^{12+}$	Stabilization	yield increase up to 92%	Knoevenagel <sup>52</sup>
	$[\text{Pd}_2\text{L}_4]^{4+}$	Stabilization	Rate acceleration $> 10^3$	Diels-Alder <sup>53</sup>
	$[\text{Fe}_4\text{L}_6]^{8+}$	Stabilization	Rate acceleration up to $10^3$	Acetal solvolysis <sup>54</sup>
	$[\text{Fe}_4\text{L}_6]^{8+}$	Stabilization	yield increase up to 20%	Organophosphate hydrolysis <sup>11</sup>
	$[\text{Pd}_6\text{L}_3]^{12+}$	Stabilization	yield increase up to 74%	Dehydrations <sup>55</sup>
	$[\text{Co}_8\text{L}_{12}]^{16+}$	Stabilization	Rate acceleration up to $10^5$	Kemp elimination <sup>56</sup>
	$[\text{Zn}_8\text{L}_6]^{16+}$	Stabilization	Rate acceleration up to 38000	Cascade (condensation and cyclization of anthranilamide and aromatic aldehydes) <sup>57</sup>
	$[\text{Pd}_8\text{L}_4]^{16+}$	Spatial constraints	up to 79% ee	Selective hydroformylation <sup>58</sup>
	$[\text{Mn}_2\text{Cr}_2\text{L}_6]^{6+}$	Stabilization	up to 99.9% ee	Alkene epoxidation <sup>59</sup>
	$[\text{Zn}_2\text{L}_{12}]^{16+}$	Shape and size	up to 99.3% ee	Oxidative kinetic resolution of 2° alcohol <sup>60</sup>
	$[\text{Pd}_{12}\text{L}_{24}]^{24+}$	Catalyst isolation	up to 93% ee	Cascade (allylic oxidation followed by Diels–Alder cyclization) <sup>61</sup>
	$[\text{Ag}_3\text{L}_2]^{3+}$	Effect from metal ions	yield increase up to 98%	Cyanosilylation of imines <sup>62</sup>

Among them, the Kemp elimination has been catalyzed highly efficiently in a cationic supramolecular organometallic cage,  $[\text{Co}_8\text{L}_{12}]^{16+}$ , (rate

acceleration of five orders of magnitude).<sup>59</sup> In addition to the enhanced reactivity, the improved selectivity, and increased yields, some reactions that do not occur in a specific solvent have been enabled in supramolecular organometallic cages by encapsulation. These examples include carbonylene and aza-Prins cyclizations in the  $[\text{Ga}_4\text{L}_6]^{12-}$  and naphthalene Diels-Alders in the  $[\text{Pd}_6\text{L}_4]^{12+}$ .<sup>8,45</sup>

### 1.7. The $\text{K}_{12}[\text{Ga}_4\text{L}_6]$ supramolecular organometallic cage.

A self-assembled tetrahedral supramolecular organometallic cage,  $\text{K}_{12}[\text{Ga}_4\text{L}_6]$  was designed and developed by the Raymond group and coworkers in a family of  $\text{M}_4\text{L}_6$  supramolecular organometallic cages.<sup>63</sup> The organic linker (L) of this metallocage, N,N'-bis(2,3-dihydroxybenzoyl)-1,5-diaminonaphthalene, is synthesized as follows:

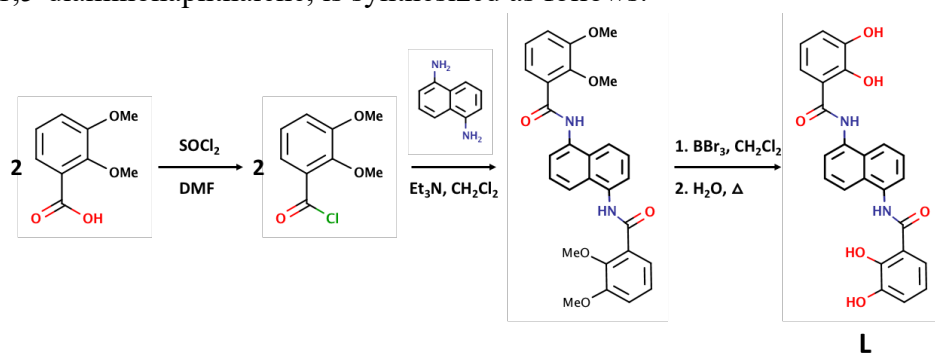


**Figure 1.11.** Synthesis of the organic linker (L) of the  $\text{K}_{12}[\text{Ga}_4\text{L}_6]$  supramolecular organometallic cage, N,N'-bis(2,3-dihydroxybenzoyl)-1,5-diaminonaphthalene.

From this organic linker (L) and several transition metal ions (M),  $[\text{ML}_3]^{(6-n)-}$ ,  $[\text{M}_2\text{L}_3]^{2(6-n)-}$ , and  $[\text{M}_4\text{L}_6]^{4(6-n)-}$  systems are synthesized based on their stoichiometric ratio (Figure 1.12).



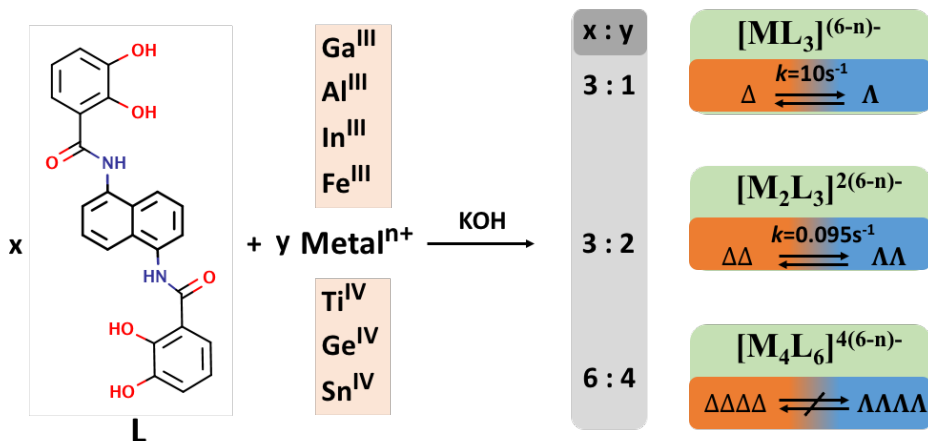


**Figure 1.12.** Schematic representation for formation of  $[\text{ML}_3]^{(6-n)-}$ ,  $[\text{M}_2\text{L}_3]^{2(6-n)-}$ , and  $[\text{M}_4\text{L}_6]^{4(6-n)-}$  systems from several transition metal ions, and N,N'-bis(2,3-dihydroxybenzoyl)-1,5-diaminonaphthalene (L) organic linker.

Each of these systems assembles as a racemic mixture of  $\Delta$  (the right-handed propeller twist of L) and  $\Lambda$  (the left-handed propeller twist of L) isomers. The interchange between these two isomers is possible for the  $[\text{ML}_3]^{(6-n)-}$  and the  $[\text{M}_2\text{L}_3]^{2(6-n)-}$  systems, but it is not possible for the  $[\text{M}_4\text{L}_6]^{4(6-n)-}$  systems. The geometries optimized with implicit solvent, of two isomers of the  $[\text{Ga}_4\text{L}_6]^{12-}$  are shown in Figure 1.13.

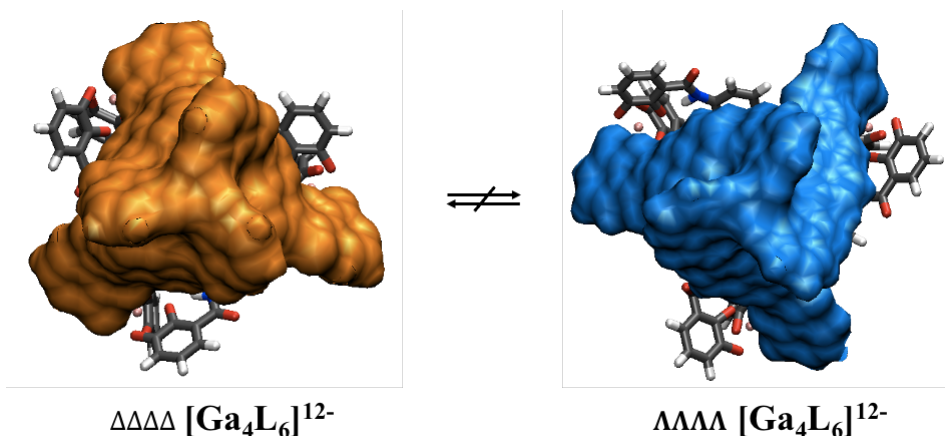


**Figure 1.13.** Optimized geometries of  $\Delta\Delta\Delta\Delta$   $[\text{Ga}_4\text{L}_6]^{12-}$  and  $\Lambda\Lambda\Lambda\Lambda$   $[\text{Ga}_4\text{L}_6]^{12-}$  at B3LYP-D3/SSD/SMD level. Three organic linkers (L) of  $[\text{Ga}_4\text{L}_6]^{12-}$  are shown by surface representation for clarity.

### 1.8. Encapsulation by $[\text{Ga}_4\text{L}_6]^{12-}$ supramolecular organometallic cage.

Due to the highly anionic nature of the  $[\text{Ga}_4\text{L}_6]^{12-}$  supramolecular organometallic cage, it is surrounded by counter ions in solution and an overall charge of -4 and -3 have been measured experimentally.<sup>63,64</sup> Thus, there can still be strong attraction between cationic molecules and the  $[\text{Ga}_4\text{L}_6]^{12-}$  surrounded by counter ions. This electrostatic interaction could help the  $[\text{Ga}_4\text{L}_6]^{12-}$  to encapsulate cationic molecules from bulk solvent. In fact, not only cationic molecules but also neutral molecules have been observed in the cavity of the  $[\text{Ga}_4\text{L}_6]^{12-}$ . The  $[\text{Ga}_4\text{L}_6]^{12-}$  offers a cavity with a volume range between  $300 \text{ \AA}^3$  and  $500 \text{ \AA}^3$  to its guest molecules.<sup>65</sup> Between these sizes, a wide range of guest molecules have been encapsulated. Recently, a site selective encapsulation by the  $[\text{Ga}_4\text{L}_6]^{12-}$  has been reported for even larger biomolecules (for example a lysine partially encapsulated).<sup>39</sup> Some of guest molecules encapsulated in the  $[\text{Ga}_4\text{L}_6]^{12-}$  are shown in Figure 1.14.<sup>65-68</sup>

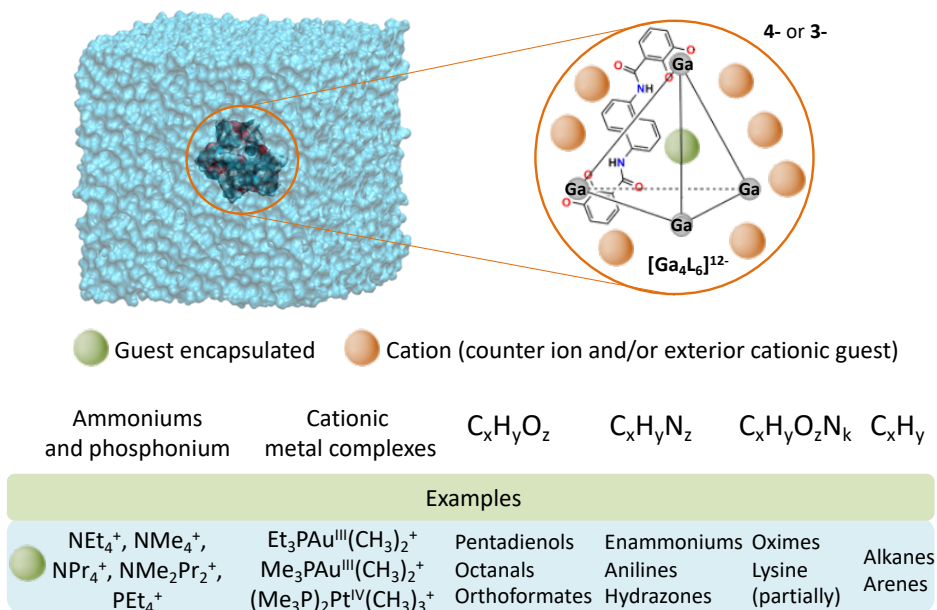


**Figure 1.14.** Examples of guest molecules encapsulated in the  $[Ga_4L_6]^{12-}$  supramolecular organometallic cage.

Among these wide range of guest molecules encapsulated in the  $[Ga_4L_6]^{12-}$ , the ammoniums and the phosphonium ( $NEt_4^+$ ,  $NMe_4^+$ ,  $NPr_4^+$ ,  $PEt_4^+$ , etc.) are investigated experimentally ( $\Delta G_{bind}^0$  range is from -2.75 to -6.85 kcal/mol) in detail and their binding affinities as well as activation parameters for guest-exchange dynamics have been measured.<sup>67</sup> For this reason, in the fourth chapter of this thesis, the binding of these ammoniums and the phosphonium in the  $[Ga_4L_6]^{12-}$  is investigated computationally in order to obtain a reliable protocol for modelling the host-guest binding with this specific supramolecular organometallic cage. In addition to this the encapsulation process is also computationally modelled to provide molecular insights to the process. In the fifth and sixth chapters, the origin of the “enzyme-like” rate accelerations in the  $[Ga_4L_6]^{12-}$  are investigated by computational means on alkyl-alkyl reductive eliminations from high valent transition metal complexes ( $Au^{III}$  and  $Pt^{IV}$ ) and on the Nazarov cyclization of 1,4-pentadien-3-ol respectively.<sup>7,37</sup>

## References:

- (1) Knowles, J. R. Enzyme Catalysis: Not Different, Just Better. *Nature*. **1991**, *350*, 121–124.
- (2) Warshel, A.; Sharma, P. K.; Kato, M.; Xiang, Y.; Liu, H.; Olsson, M. H. M. Electrostatic Basis for Enzyme Catalysis. *Chem. Rev.* **2006**, *106*, 3210–3235.
- (3) Martí, S.; Roca, M.; Andrés, J.; Moliner, V.; Silla, E.; Tuñón, I.; Bertrán, J. Theoretical Insights in Enzyme Catalysis. *Chem. Soc. Rev.* **2004**, *33*, 98–107.
- (4) Kang, J.; Rebek Jr., J. Acceleration of a Diels-Alder Reaction by a Self-Assembled Molecular Capsule. *Nature*. **1997**, *385*, 50–52.
- (5) Raynal, M.; Ballester, P.; Vidal-Ferran, A.; Van Leeuwen, P. W. N. M. Supramolecular Catalysis. Part 1: Non-Covalent Interactions as a Tool for Building and Modifying Homogeneous Catalysts. *Chem. Soc. Rev.* **2014**, *43*, 1660–1733.
- (6) Raynal, M.; Ballester, P.; Vidal-Ferran, A.; Van Leeuwen, P. W. N. M. Supramolecular Catalysis. Part 2: Artificial Enzyme Mimics. *Chem. Soc. Rev.* **2014**, *43*, 1734–1787.
- (7) Hastings, C. J.; Pluth, M. D.; Bergman, R. G.; Raymond, K. N. Enzymelike Catalysis of the Nazarov Cyclization by Supramolecular Encapsulation. *J. Am. Chem. Soc.* **2010**, *132*, 6938–6940.
- (8) Murase, T.; Horiuchi, S.; Fujita, M. Naphtalene Diels-Alder in a Self-Assembled Molecular Flask. *J. Am. Chem. Soc.* **2010**, *132*, 2866–2867.
- (9) Kuijpers, P. F.; Otte, M.; Dürr, M.; Ivanović-Burmazović, I.; Reek, J. N. H.; de Bruin, B. A Self-Assembled Molecular Cage for Substrate-Selective Epoxidation Reactions in Aqueous Media. *ACS Catal.* **2016**, *6*, 3106–3112.
- (10) Leenders, S. H. A. M.; Gramage-Doria, R.; de Bruin, B.; Reek, J. N. H. Transition Metal Catalysis in Confined Spaces. *Chem. Soc. Rev.* **2015**, *44*, 433–448.
- (11) Bolliger, J. L.; Belenguer, A. M.; Nitschke, J. R. Enantiopure Water-Soluble [Fe<sub>4</sub>L<sub>6</sub>] Cages: Host-Guest Chemistry and Catalytic Activity. *Angew. Chem. Int. Ed.* **2013**, *52*, 7958–7962.
- (12) Young, T. A.; Martí-Centelles, V.; Wang, J.; Lusby, P. J.; Duarte, F. Rationalizing the Activity of an “Artificial Diels-Alderase”: Establishing Efficient and Accurate Protocols for Calculating Supramolecular Catalysis. *J. Am. Chem. Soc.* **2020**, *142*, 1300–

- 1310.
- (13) Pahima, E.; Zhang, Q.; Tiefenbacher, K.; Major, D. T. Discovering Monoterpene Catalysis Inside Nanocapsules with Multiscale Modeling and Experiments. *J. Am. Chem. Soc.* **2019**, *141*, 6234–6246.
  - (14) Wolf, K. L.; Frahm, H.; Harms, H. Über Den Ordnungszustand Der Moleküle in Flüssigkeiten. *Z. Phys. Chem.* **1937**, *36*, 237-287.
  - (15) Steed, J. W.; Atwood, J. L. *Supramolecular Chemistry*, Wiley, New York **2000**.
  - (16) Lehn, J. M. Cryptates: Inclusion Complexes of Macropolycyclic Receptor Molecules. *Pure Appl. Chem*, **1978**, *50*, 871-892.
  - (17) Schalley, C. A. *Analytical Methods in Supramolecular Chemistry*, Wiley, **2007**.
  - (18) Meyer, E. A.; Castellano, R. K.; Diederich, F. Interactions with Aromatic Rings in Chemical and Biological Recognition. *Angew. Chem. Int. Ed.*, **2003**, *42*, 1210-1250.
  - (19) Ma, J. C.; Dougherty, D. A. The Cation- $\pi$  Interaction. *Chem. Rev.* **1997**, *97*, 1303–1324.
  - (20) IUPAC. *Compendium of Chemical Terminology*, 2nd Ed. (the “Gold Book”). Glossary of Class Names of Organic Compounds and Reactivity Intermediates Based on Structure (IUPAC Recommendations **1995**), *67*, 1307, p1344.
  - (21) Cronstedt, A. F. *Natural Zeolite and Minerals*. Svenska Vetenskaps Akademiens Handlingar Stockholm. **1756**, *17*, 120.
  - (22) Villiers, A. Sur La Transformation de La Fécule En Dextre Par Le Ferment Butyrique. *Compt. Rend. Acad. Sci.* **1891**, 536–538.
  - (23) Breslow, R.; Overman, L. E. “Artificial Enzyme” Combining a Metal Catalytic Group and a Hydrophobic Binding Cavity. *J. Am. Chem. Soc.* **1970**, *92*, 1075-1077.
  - (24) Pedersen, C. J. Cyclic Polyethers and Their Complexes with Metal Salts. *J. Am. Chem. Soc.* **1967**, *89*, 2495-2496.
  - (25) Dietrich, B.; Lehn, J. M.; Sauvage, J. P. “Les Cryptates”. *Tetrahedron Letters*. **1969**, *10*, 2889–2892.
  - (26) Kyba, E. P.; Siegel, M. G.; Sousa, L. R.; Sogah, G. D. Y.; Cram, D. J. Chiral, Hinged, and Functionalized Multiheteromacrocycles, *J. Am. Chem. Soc.* **1973**, *95*, 2691-2692.
  - (27) Fujita, D.; Ueda, Y.; Sato, S.; Mizuno, N.; Kumasaka, T.; Fujita, M. Self-Assembly of Tetravalent Goldberg Polyhedra from 144 Small Components. *Nature*, **2016**, *540*, 563–566.

- (28) Leung, D. H.; Bergman, R. G.; Raymond, K. N. Leung, D. H.; Bergman, R. G.; Raymond, K. N. Scope and Mechanism of the C-H Bond Activation Reactivity within a Supramolecular Host by an Iridium Guest: A Stepwise Ion Pair Guest Dissociation Mechanism. *J. Am. Chem. Soc.* **2006**, *128*, 9781–9797.
- (29) Davis, A. V.; Fiedler, D.; Seeber, G.; Zahl, A.; van Eldik, R.; Raymond, K. N. Guest Exchange Dynamics in an M<sub>4</sub>L<sub>6</sub> Tetrahedral Host. *J. Am. Chem. Soc.* **2006**, *128*, 1324–1333.
- (30) Ballester, P.; Scarso, A. Editorial: Supramolecular Aspects in Catalysis. *Front. Chem.* **2019**, *7*, 174.
- (31) Warshel, A.; Sharma, P.K.; Kato, M.; Xiang, Y.; Liu, H.; Olsson, M. H. M. Electrostatic Basis of Enzyme Catalysis. *Chem. Rev.* **2006**, *106*, 3210–3235.
- (32) Brown, C. J.; Toste, F. D.; Bergman, R. G.; Raymond, K. N. Supramolecular Catalysis in Metal–Ligand Cluster Hosts. *Chem. Rev.* **2015**, *115*, 3012–3035.
- (33) Ballester, P.; Fujita, M.; Rebek Jr., J. Molecular Containers. *Chem. Soc. Rev.* **2015**, *44*, 392–393.
- (34) Fang, Y.; Powell, J. A.; Li, E.; Wang, Q.; Perry, Z.; Kirchon, A.; Yang, X.; Xiao, Z.; Zhu, C.; Zhang, L.; Huang, F.; Zhou, H-C. Catalytic Reactions within the Cavity of Coordination Cages. *Chem. Soc. Rev.* **2019**, *48*, 4707–4730.
- (35) Pluth, M. D.; Bergman, R. G.; Raymond, K. N. Proton-Mediated Chemistry and Catalysis in a Self-Assembled Supramolecular Host. *Acc. Chem. Res.* **2009**, *42*, 1650–1659.
- (36) Hong, C. M.; Bergman, R. G.; Raymond, K. N.; Toste, F. D. Self-Assembled Tetrahedral Hosts as Supramolecular Catalysts. *Acc. Chem. Res.* **2018**, *51*, 2447–2455.
- (37) Kaphan, D. M.; Levin, M. D.; Bergman, R. G.; Raymond, K. N.; Toste, F. D. A Supramolecular Microenvironment Strategy for Transition Metal Catalysis. *Science*, **2015**, *350*, 1235–1238.
- (38) Hart-Cooper, W. M.; Clary, K. N.; Toste, F. D.; Bergman, R. G.; Raymond, K. N. Selective Monoterpene-like Cyclization Reactions Achieved by Water Exclusion from Reactive Intermediates in a Supramolecular Catalyst. *J. Am. Chem. Soc.* **2012**, *134*, 17873–17876.
- (39) Hart-Cooper, W. M.; Zhao, C.; Triano, R. M.; Yaghoubi, P.; Ozores, H. L.; Burford, K. N.; Toste, F. D.; Bergman, R. G.; Raymond, K. N. The Effect of Host Structure on the Selectivity and Mechanism of Supramolecular Catalysis of Prins Cyclizations. *Chem. Sci*, **2015**,

- 6, 1383-1393.
- (40) Kaphan, D. M.; Toste, F. D.; Bergman, R. G.; Raymond, K. N. Enabling New Modes of Reactivity via Constrictive Binding in a Supramolecular-Assembly-Catalyzed Aza-Prins Cyclization. *J. Am. Chem. Soc.* **2015**, *137*, 9202–9205.
- (41) Fiedler, D.; van Halbeek, H.; Bergman, R. G.; Raymond, K. N. Supramolecular Catalysis of Unimolecular Rearrangements: Substrate Scope and Mechanistic Insights. *J. Am. Chem. Soc.* **2006**, *128*, 10240–10252.
- (42) Pluth, M. D.; Bergman, R. G.; Raymond, K. N. Supramolecular Catalysis of Orthoformate Hydrolysis in Basic Solution: An Enzyme-Like Mechanism. *J. Am. Chem. Soc.* **2008**, *130*, 11423–11429.
- (43) Bierschenk, S. M.; Bergman, R. G.; Raymond, K. N.; Toste, F. D. A Nanovessel-Catalyzed Three-Component Aza-Darzens Reaction. *J. Am. Chem. Soc.* **2020**, *142*, 733–737.
- (44) Bender, T. A.; Bergman, R. G.; Raymond, K. N.; Toste, F. D. A Supramolecular Strategy for Selective Catalytic Hydrogenation Independent of Remote Chain Length. *J. Am. Chem. Soc.* **2019**, *141*, 11806–11810.
- (45) Leung, D. H.; Bergman, R. G.; Raymond, K. N. Highly Selective Supramolecular Catalyzed Allylic Alcohol Isomerization. *J. Am. Chem. Soc.* **2007**, *129*, 2746–2747.
- (46) Wang, Z. J.; Brown, C. J.; Bergman, R. G.; Raymond, K. N.; Toste, F. D. Hydroalkoxylation Catalyzed by a Gold(I) Complex Encapsulated in a Supramolecular Host. *J. Am. Chem. Soc.* **2011**, *133*, 7358-7360.
- (47) Morimoto, M.; Cao, W.; Bergman, R. G.; Raymond, K. N.; Toste, F. D. Chemoselective and Site-Selective Reductions Catalyzed by a Supramolecular Host and a Pyridine–Borane Cofactor. *J. Am. Chem. Soc.* **2021**, *143*, 2108-2114.
- (48) Bender, T. A.; Morimoto, M.; Bergman, R. G.; Raymond, K. N.; Toste, F. D. Supramolecular Host-Selective Activation of Iodoarenes by Encapsulated Organometallics. *J. Am. Chem. Soc.* **2019**, *141*, 1701-1706.
- (49) Paul, A.; Shipman, M. A.; Onabule, D. Y.; Sproules, S.; Symes, M. D. Selective Aldehyde Reductions in Neutral Water Catalysed by Encapsulation in a Supramolecular Cage, *Chem. Sci.*, **2021**, *12*, 5082-5090.
- (50) Salles A. J. Jr.; Zarra, S.; Turner, R. M.; Nitschke, J. R. A Self-

- Organizing Chemical Assembly Line. *J. Am. Chem. Soc.*, **2013**, *135*, 19143-19146.
- (51) Roberts, D. A.; Pilgrim, B. S.; Nitschke, J. R. Covalent Post-Assembly Modification in Metallosupramolecular Chemistry. *Chem. Soc. Rev.* **2018**, *47*, 626–644.
- (52) Murase, T.; Nishijima, Y.; Fujita, M. Cage-Catalyzed Knoevenagel Condensation under Neutral Conditions in Water. *J. Am. Chem. Soc.* **2012**, *134*, 162–164.
- (53) Martí-Centelles, V.; Lawrence, A. L.; Lusby, P. J. High Activity and Efficient Turnover by a Simple, Self-Assembled “Artificial Diels-Alderase.” *J. Am. Chem. Soc.* **2018**, *140*, 2862–2868.
- (54) Holloway, L. R.; Bogie, P. M.; Lyon, Y.; Ngai, C.; Miller, T. F.; Julian, R. R.; Hooley, R. J. Tandem Reactivity of a Self-Assembled Cage Catalyst with Endohedral Acid Groups. *J. Am. Chem. Soc.* **2018**, *140*, 8078–8081.
- (55) Das, P.; Kumar, A.; Howlader, P.; Mukherjee, P. S. A Self-Assembled Trigonal Prismatic Molecular Vessel for Catalytic Dehydration Reactions in Water. *Chem. Eur. J.*, **2017**, *23*, 12565–12574.
- (56) Cullen, W.; Misuraca, M. C.; Hunter, C. A.; Williams, N. H.; Ward, M. D. Highly Efficient Catalysis of the Kemp Elimination in the Cavity of a Cubic Coordination Cage. *Nat. Chem.* **2016**, *8*, 231–236.
- (57) Jiao, J. J.; Li, Z.; Qiao, Z.; Li, X.; Liu, Y.; Dong, J.; Jiang, J.; Cui, Y. Design and Self-Assembly of Hexahedral Coordination Cages for Cascade Reactions. *Nat. Commun.*, **2018**, *9*, 4423.
- (58) Gadzikwa, T.; Bellini, R.; Dekker, H. L.; Reek, J. N. H. Self-Assembly of a Confined Rhodium Catalyst for Asymmetric Hydroformylation of Unfunctionalized Internal Alkenes. *J. Am. Chem. Soc.* **2012**, *134*, 2860–2863.
- (59) Jiao, J.; Tan, C.; Li, Z.; Liu, Y.; Han, X.; Cui, Y. Design and Assembly of Chiral Coordination Cages for Asymmetric Sequential Reactions. *J. Am. Chem. Soc.* **2018**, *140*, 2251–2259.
- (60) Tan, C.; Jiao, J.; Li, Z.; Liu, Y.; Han, X.; Cui, Y. Design and Assembly of a Chiral Metallosalen-Based Octahedral Coordination Cage for Supramolecular Asymmetric Catalysis. *Angew. Chem. Int. Ed.* **2018**, *57*, 2085–2090.
- (61) Ueda, Y.; Ito, H.; Fujita, D.; Fujita, M. Permeable Self-Assembled Molecular Containers for Catalyst Isolation Enabling Two-Step Cascade Reactions. *J. Am. Chem. Soc.* **2017**, *139*, 6090–6093.
- (62) Wang, D.; Zhang, B.; He, C.; Wu, P.; Duan, C. A New Chiral N-



- Heterocyclic Carbene Silver(i) Cylinder: Synthesis, Crystal Structure and Catalytic Properties. *Chem. Commun.* **2010**, *46*, 4728–4730.
- (63) Caulder, D. L.; Brückner, C.; Powers, R. E.; König, S.; Parac, T. N.; Leary, J. A.; Raymond, K. N. Design, Formation and Properties of Tetrahedral  $M_4L_4$  and  $M_4L_6$  Supramolecular Clusters. *J. Am. Chem. Soc.* **2001**, *123*, 8923–8938.
- (64) Andersen, U. N.; Seeber, G.; Fiedler, D.; Raymond, K. N.; Lin, D.; Harris, D. Characterization of Self-Assembled Supramolecular  $[Ga_4L_6]$  Host-Guest Complexes by Electrospray Ionization Mass Spectrometry. *J. Am. Soc. Mass Spectrom.* **2006**, *17*, 292–296.
- (65) Biros, S. M.; Bergman, R. G.; Raymond, K. N. The Hydrophobic Effect Drives the Recognition of Hydrocarbons by an Anionic Metal-Ligand Cluster. *J. Am. Chem. Soc.* **2007**, *129*, 12094–12095.
- (66) Parac, T. N.; Caulder, D. L.; Raymond, K. N. Selective Encapsulation of Aqueous Cationic Guests into a Supramolecular Tetrahedral  $[M_4L_6]^{12-}$  Anionic Host. *J. Am. Chem. Soc.* **1998**, *120*, 8003–8004.
- (67) Pluth, M. D.; Raymond, K. N. Reversible Guest Exchange Mechanisms in Supramolecular Host-Guest Assemblies. *Chem. Soc. Rev.* **2007**, *36*, 161–171.
- (68) Levin, M. D.; Kaphan, D. M.; Hong, C. M.; Bergman, R. G.; Raymond, K. N.; Toste, F. D. Scope and Mechanism of Cooperativity at the Intersection of Organometallic and Supramolecular Catalysis. *J. Am. Chem. Soc.* **2016**, *138*, 9682–9693.

# Chapter 2.

## Theories and methods.

Anything that has mass exists in three-dimension space and gathered under the term, matter, in natural science. Materialism says that the mode of the existence of matter is motion and general forms of the existence of matter are space and time. A theory of everything from massless particles to the whole universe remains unsolved. There are four main theories describing the motion of matter in lieu (Figure 2.1).

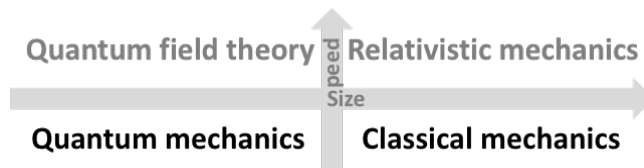


**Figure 2.1.** Four main domains in physics.

In case we deal with things at speed much lower than the speed of light, quantum mechanics explains the natural world. Even though, quantum mechanics provides better accuracy than classical mechanics, its application to large systems is limited due to the complexity of the system that requires enormous computational resources and time to solve. Thus, classical mechanics is used almost exclusively at nanoscale, whereas quantum mechanics is essential to chemical reactions.

### 2.1 Computing energy.

#### 2.1.1. Quantum Mechanics.

##### 2.1.1.1. Introduction to quantum mechanics.

Quantum mechanics introduces a particle-wave duality and uncertainty into science. The uncertainty principle is a key principle of the quantum mechanics as Prof. Hawking said, “Quantum mechanics allows us in principle to predict nearly everything around us within the limits set by

uncertainty principle”.<sup>1</sup> The general uncertainty principle is given below (Eq.2.1).

$$\sigma_A^2 \sigma_B^2 \geq \left( \frac{1}{2i} \langle [\hat{A}, \hat{B}] \rangle \right)^2 \quad (\text{Eq.2.1})$$

where  $\hat{A}, \hat{B}$  are Hermitian operators and  $\sigma_A$  and  $\sigma_B$  are standard deviations associated with A and B respectively.

When  $\hat{A} = \hat{x}$ , position,  $\hat{B} = \hat{p}$ , momentum, then it is Heisenberg uncertainty principle:

$$\sigma_x \sigma_p \geq \frac{\hbar}{2} \text{ using } [\hat{x}, \hat{p}] = i\hbar \text{ where } \hbar \text{ is the reduced Planck constant.}$$

The fundamental equation of the quantum mechanics is the Schrödinger equation. Its most compact form is given by the Eq.2.2

$$\hat{H}\Psi = E\Psi \quad (\text{Eq.2.2})$$

In mathematics, it is an eigenvalue equation.  $\hat{H}$  is the Hamiltonian (total energy operator) and E is energy (eigenvalue of the equation).  $\Psi$  is the wave function which contains all the information about the system. The Hamiltonian can be expressed as the sum of the kinetic and potential energy operators of the system and therefore the one-dimension time-independent Schrödinger equation for single nonrelativistic particle is written as

$$\hat{H}\psi(x) = \left( -\frac{\hbar^2}{2m} \nabla^2 + V(x) \right) \psi(x) = E\psi(x) \quad (\text{Eq.2.3})$$

where  $-\frac{\hbar^2}{2m} \nabla^2$  is the kinetic energy operator ( $\nabla^2$ -Laplacian and m-mass of the particle) and  $V(x)$  is the potential energy operator.

### 2.1.1.2. Hartree-Fock and post-Hartree-Fock theories.

Since the nuclear motion is much slower than electron motion, we can treat only the electrons as quantum particles in the field of fixed nuclei which is called the Born-Oppenheimer (BO) approximation. Within this approximation, the one-electron Hamiltonian for the  $i$ th electron is given by

$$\hat{H}(i) = \left( -\frac{\hbar^2}{2m_e} \nabla(i)^2 - \sum_{k=1}^n \frac{Z_k e^2}{r_{ik}} \right) \quad (\text{Eq.2.4})$$

where  $m_e$  is the electron mass,  $e$  is the electron charge,  $Z$  is atomic number of nucleus and  $r$  is the distance between the charges.

If there is more than one electron, the electronic Hamiltonian includes the electron-electron interaction which is problematic. It can be expressed in the general form

$$\hat{H} = \left( \sum_{i=1}^N \hat{H}(i) + \sum_{i<j}^N V_{int}(i, j) \right) \quad (\text{Eq.2.5})$$

where  $V_{int}(i, j)$  is the part of the Hamiltonian that describes the interaction between the electrons.

An approximation for the interaction between electrons is treating each electron as independent in an average way, neglecting the correlated motion of the electrons. This is the fundamental approximation of the Hartree-Fock method (self-consistent field approach, SCF) in which the many-electron wave function is expressed as an anti-symmetrized product of one-electron molecular orbitals (MOs), so-called Slater determinant. The main weakness of this method is that it does not include the electron correlation and therefore it can be inaccurate in any process in which the nature of the bond significantly changes. Also, charge distributions calculated at the Hartree-Fock level tend to be overpolarized and hence it is not suitable for modeling highly ionic systems. At any rate, it is the base of much of electronic structure theory.

In order to improve the accuracy of the Hartree-Fock method, the configuration-interaction (CI), perturbation and coupled-cluster (CC) methods have been developed (the post-Hartree-Fock wave function theory). At present, the coupled cluster theory represents the most successful method for accurate many-electron molecular wave functions. The coupled cluster singles and doubles including perturbative triples method (CCSD(T)) is considered as the “gold standard” in quantum chemistry. It is a truncated model of the coupled cluster theory.<sup>2</sup> In order to account a pair interaction more effectively than a generic interaction, coupled cluster wave function ( $\Psi_{CC}$ ) is defined by the Eq.2.6

$$\Psi_{CC} = e^{\hat{T}} \Psi_{HF} = \sum_{i=0}^N \hat{C}_i \Psi_{HF} \quad (\text{Eq.2.6})$$

where,  $\hat{T}$ : cluster operator, expressed by  $\hat{T} = \hat{T}_1^{single} + \hat{T}_2^{double} + \hat{T}_3^{triple} + \dots$ .  $\hat{T}_1^{single}$  is the operator of all single excitations and  $\hat{T}_2^{double}$  is the operator of all double excitations, and so on. The general  $n$ -fold cluster operator ( $\hat{T}_n$ ) can be written as follows:

$$\hat{T}_n = \frac{1}{(n!)^2} \sum_{o_1, o_2, \dots, o_n} \sum_{v_1, v_2, \dots, v_n} t_{o_1, o_2, \dots, o_n}^{v_1, v_2, \dots, v_n} \hat{a}_{v_1}^\dagger \hat{a}_{v_2}^\dagger \dots \hat{a}_{v_n}^\dagger \hat{a}_{o_1} \hat{a}_{o_2} \dots \hat{a}_{o_n}$$

where,  $o$ : occupied and  $v$ : virtual (unoccupied) orbitals,  $t$ : coefficient,  $\hat{a}_v^\dagger$ : creation and  $\hat{a}_o$ : annihilation operators

Therefore, the cluster operator of all single excitations ( $\hat{T}_1$ ) is given by

$$\hat{T}_1 = \sum_{vo} t_o^v \hat{a}_v^\dagger \hat{a}_o = \sum_{vo} t_o^v E_{vo} \quad (\text{Eq.2.7})$$

where,  $E_{vo}$  is the singlet one-electron excitation operator

The configuration excitation operators ( $\hat{C}$ ) are expressed by cluster operators. For instance,  $\hat{C}_2 = \hat{T}_2 + \frac{1}{2} \hat{T}_1^2$

The coupled cluster singles and doubles energy ( $E_{CCSD}$ ) is expressed by the Eq.2.8.<sup>2</sup>

$$E_{CCSD} = E_{HF} + \frac{1}{2} \langle \Psi_{HF} | [[\hat{H}, \hat{T}_1], \hat{T}_1] | \Psi_{HF} \rangle + \langle \Psi_{HF} | [[\hat{H}, \hat{T}_2]] | \Psi_{HF} \rangle (\text{Eq.2.8})$$

### 2.1.1.3. Density functional theory.

The problem about the exact application of the quantum mechanics on many-body systems has been discussed since the theory was introduced. In 1964, the density functional theory was established by Pierre Hohenberg and Walter Kohn, suggesting the usage of electron density.<sup>3</sup>

$$E_\rho = \left\{ \int V(r) \rho(r) d^3r + F[\rho(r)] \right\} \quad (\text{Eq.2.9})$$

The first Hohenberg-Kohn theorem shows that the non-degenerate ground state density is uniquely related to the wave function, indicating an existence of the  $F[\rho(r)]$  function and the second theorem of Hohenberg-Kohn states that the density obeys variational principle, the ground state energy can thus be obtained variationally.<sup>4</sup>

Practical use of the density functional theory started with Kohn-Sham self-consistent field approach. The Kohn-Sham equation (Eq.2.10) introduces the exchange-correlation term which also includes the correction to the kinetic energy from non-interacting to interacting in addition to all non-classical corrections to electron-electron interaction.

$$E_\rho = E_{kin}^{KS}[\rho(r)] + E_{ne}[\rho(r)] + E_{ee}[\rho(r)] + E_{xc}[\rho(r)] (\text{Eq.2.10})$$

where  $\rho(r)$  is the density given by  $\rho(r) = \sum_{i=1}^N |\chi_i(r)|^2$  where  $\chi$  basis functions.

The Eq.2.10 can thus be written as follows:

$$E_{\rho} = \sum_i^N \left( \langle \chi_i | -\frac{1}{2} \nabla_i^2 | \chi_i \rangle - \langle \chi_i | \sum_n^{nuclei} \frac{Z_n}{|r_i - r_n|} | \chi_i \rangle \right) + \sum_i^N \langle \chi_i | \frac{1}{2} \int \frac{\rho(r')}{|r_i - r'|} dr' | \chi_i \rangle + E_{xc}[\rho(r)] \quad (\text{Eq.2.11})$$

When the exchange and the correlation potentials only depend on the density, the local approximation can be written by the Eq.2.12 called the local spin density approximation (LSDA) which was discussed by Kohn and Sham:

$$E_{\rho}^{LSDA} = E_{kin}^{KS} + E_{ne} + E_{ee} + \int d^3r \rho(r) \{ \varepsilon_x[\rho(r)] + \varepsilon_c[\rho(r)] \} \quad (\text{Eq.2.12})$$

Currently, there are around 200 density functionals reported. We used a hybrid (HF-DFT) exchange-correlation (XC) functional, namely the B3LYP functional<sup>5,6</sup>, for DFT calculations which is expressed by the following equation:

$$E_{xc}^{B3LYP} = (1 - a)E_x^{LSDA} + aE_x^{HF} + b\Delta E_x^B + (1 - c)E_c^{LSDA} + cE_c^{LYP} \quad (\text{Eq.2.13})$$

where,  $a, b, c$  are (0.20, 0.72, 0.81, respectively) optimized parameters by Becke  
 $E_c^{LYP}$  is the Lee – Yang – Parr correlation energy

Despite the limitation of the B3LYP functional in some fields such as the spin state splitting, it is by far one of the most accurate functionals for the calculation involving organometallic complexes such as reactivity in bioinorganic systems.

#### 2.1.1.4. Dispersion corrections.

The dispersion should be accounted for geometry calculations at QM level unless the functional includes it. Let's describe a general view of three atoms by their interatomic distances ( $\mathbf{R}_{ij}$ ) and bond angles ( $\theta$ ) (Figure 2.2).

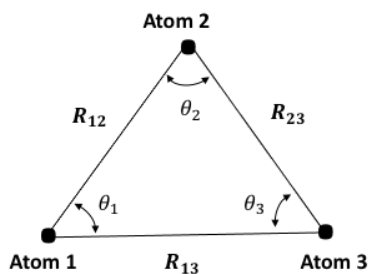


**Figure 2.2.** Schematic representation of three atoms.

The three-body dispersion energy is given by the Axilrod-Teller potential<sup>10,11</sup> (Eq. 2.14).

$$E_{inter} \cong \frac{3(V_1 + V_2 + V_3)V_1V_2V_3\alpha_1\alpha_2\alpha_3(3\cos\theta_1\cos\theta_2\cos\theta_3 + 1)}{2(V_1 + V_2)(V_2 + V_3)(V_1 + V_3)R_{12}^3R_{23}^3R_{13}^3} \quad (\text{Eq.2.14})$$

where,  $V_1, V_2, V_3$  are the first ionization potentials of atom 1, atom 2, atom 3  
 $\alpha_1, \alpha_2, \alpha_3$  are the static polarizabilities of atom 1, atom 2, atom 3.

The significance of this correction increases with the size of the system. It is thus recommended to include it for calculating the energetics of the process that involves supramolecular systems. This has not been implemented in the Gaussian 09 program,<sup>12</sup> but it can be calculated with the dftd3 program<sup>7</sup> developed by the Grimme group using the optimized geometries and the functional used. The two-body terms of the DFT-D3 dispersion correction are implemented in the Gaussian 09 software.

### 2.1.1.5. Entropy correction.

In order to calculate a Gibbs energy, entropy contributions should be computed at first with a quantum chemical vibrational frequencies calculation and then appropriate corrections can be applied. In general, translational, rotational and vibrational entropies are computed by the quantum chemical vibrational frequencies calculation. The vibrational entropy of a harmonic oscillator is given by the following equation:

$$S_{vib} = R \left( \frac{h\omega}{k_B(\exp(\frac{h\omega}{k_B T}) - 1)} - \ln(1 - \exp(\frac{-h\omega}{k_B T})) \right) \quad (\text{Eq.2.15})$$

where  $\omega$  is the frequency

when the frequency approaches to zero, the first term of the right side of the Eq.2.15 approaches asymptotically infinity. It is thus proposed by Grimme to replace the low-frequency contribution to the vibrational entropy by corresponding rotational entropy, which is *quasi-rigid rotor harmonic oscillator approach (quasi-RRHO)*.<sup>7</sup>

Here, the reduced mass ( $\mu^r$ ) was determined by the average molecular moment of inertia ( $\bar{I}$ ) introduced in order to define effective moment of inertia. The entropy of the low-frequency mode was expressed in this approximation by the Eq.2.16.

$$S_{low-v} = R \left( \frac{1}{2} + \ln \left[ \left( \frac{8\pi^3 \mu^r kT}{h^2} \right)^{\frac{1}{2}} \right] \right) \quad (\text{Eq.2.16})$$

where  $\bar{I}$  is an average molecular moment of inertia,  $\mu^r = \frac{\mu \bar{I}}{\mu + \bar{I}}$  and  $\mu = \frac{h}{8\pi^2 \omega}$

Then, to combine  $S_{vib}$  and  $S_{low-v}$ , a weighting function of the frequency was used as follows:

$$S_v = f(\omega)S_{vib} + (1 - f(\omega))S_{low-v} \quad (\text{Eq.2.17})$$

The  $f(\omega)$  is the Head-Gordon dumping function<sup>8</sup> expressed by the Eq.2.18 and  $\alpha$  is equal to 4.

$$f(\omega) = \frac{1}{1 + (\frac{\omega_0}{\omega})^\alpha} \quad (\text{Eq.2.18})$$

In this work, this correction was performed using the GoodVibes.py program.<sup>9</sup>

### 2.1.1.6. Solvation effects.

It is widely accepted that solvation is an important process and can affect the kinetics and thermodynamics of the process (Figure 2.3).



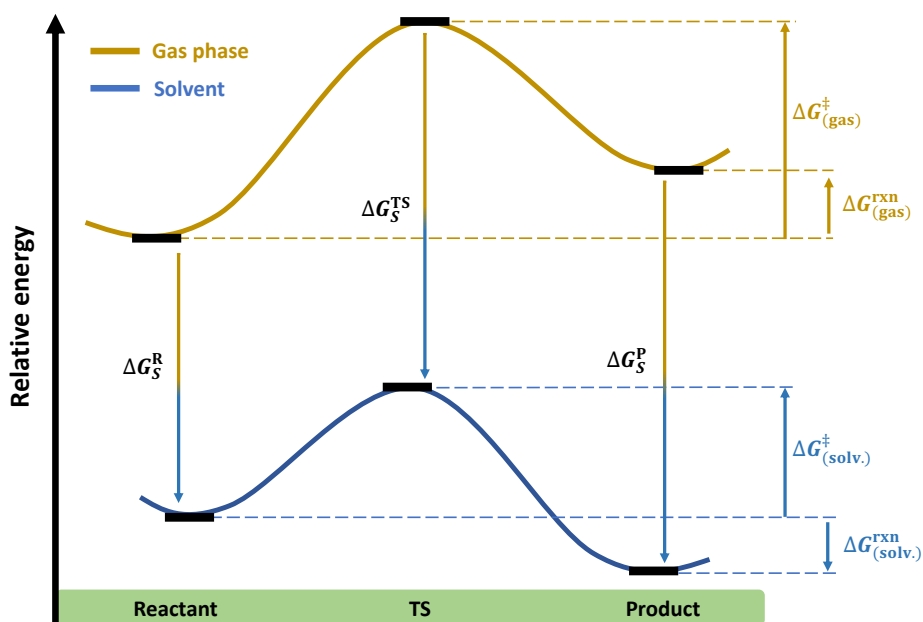


**Figure 2.3.** A hypothetical Gibbs energy cycle associated with solvation.

Several types of intermolecular interactions between the solvent and solute may play a significant role throughout the process. Depending on the interaction between the solvent and solute, the wave function or the electron density of the system in solution can be very different from the one in vacuum. Thus, it should be as accurate as possible for modeling the energetics of the process in solution. But there is still a limitation at pure QM level for computing energies of large systems together with their solvent environment all explicit due to its complexity and computational time. Therefore, implicit or continuum solvent models are broadly used to take into account the solvation effects.<sup>13</sup> They are aimed at reflecting the effect of the solvent environment on the solute. One of these models is the SMD solvation model.<sup>14</sup> In this model, the Gibbs energy of solvation is described as follows (Figure 2.4):

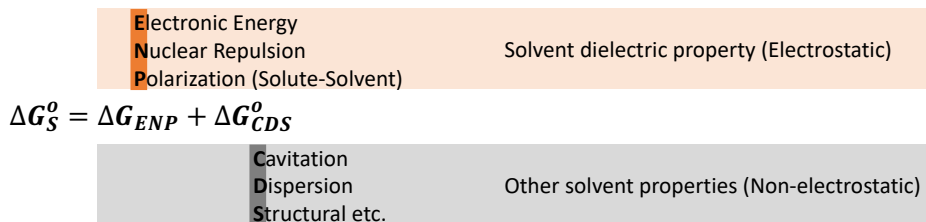


**Figure 2.4.** Solvation Gibbs energy of the SMD continuum solvent model.

The electrostatic term of the Gibbs energy of solvation is generally based on the solvent dielectric whereas the non-electrostatic term is parametrized based on experimental data and set of solvent descriptors such as refractive index, surface tension, carbon aromaticity, electronegative halogenicity, hydrogen bond acidity/basicity. In general, continuum solvation models provide a better agreement between the calculation and experiment for neutral molecules than ions. To improve the results for ions, so-called hybrid or mixed explicit-implicit (cluster) approaches have been reported.<sup>15–18</sup> In brief, all solvation approaches can be generalized into three categories as shown in Figure 2.5.

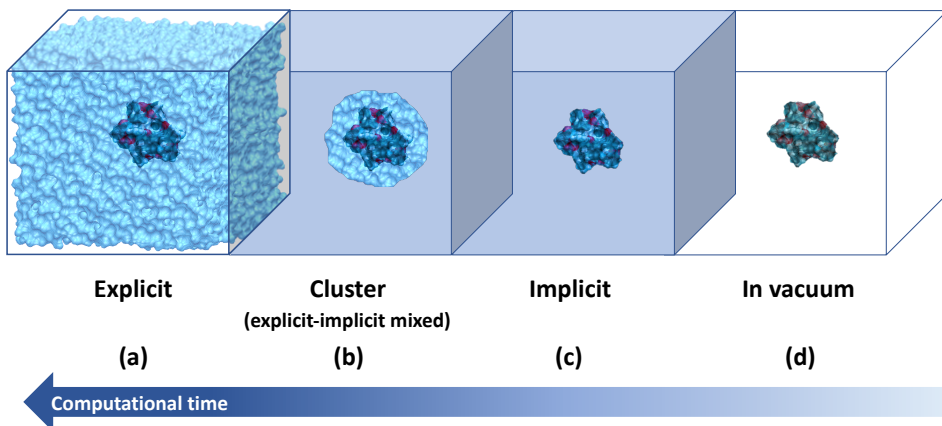


**Figure 2.5.** General solvation approaches.

## 2.1.2. Molecular Mechanics.

### 2.1.2.1. Introduction to molecular mechanics.

Application of classical mechanics to molecular systems is called classical molecular mechanics. In classical molecular mechanics, atoms obey the following laws of classical physics:

(i) Newton's laws of motion:

$$\text{if } \sum F = 0, \text{ then } \frac{dv}{dt} = 0 \quad (\text{Eq.2.19})$$

where  $F$  is the force,  $v$  is the velocity,  $t$  is the time

$$F = \frac{dp}{dt} = \frac{d(mv)}{dt} = m \frac{dv}{dt} = ma = m \frac{d^2r}{dt^2} \quad (\text{Eq.2.20})$$

where  $m$  is the mass,  $a$  is the acceleration

(ii) Hooke's law

$$F = -kx \quad (\text{Eq.2.21})$$

where  $k$  is the force constant,  $x$  is the displacement

(iii) Coulomb's law

$$|F| = \frac{|q_1 q_2|}{4\pi\epsilon_0 r^2} \quad (\text{Eq.2.22})$$

where  $q$  is the charge,  $r$  is the distance between two charges

In addition, the Leonard-Jones potential<sup>19</sup> is often used to define an intermolecular potential, given by Eq.2.23.

$$V_{LJ} = \epsilon \left[ \left( \frac{R}{r} \right)^{12} - \left( \frac{R}{r} \right)^6 \right] \quad (\text{Eq.2.23})$$

where  $\epsilon$  is the depth of  $V$ ,  $R$  is the distance when  $V = 0$

### 2.1.2.2. Force fields.

In order to model a molecular system using classical molecular mechanics, bonding and non-bonding terms (parameters) of all atoms of the system are required. In general, this set of parameters is called a force field. Several types of force fields have been developed with simulation programs such as Amber,<sup>20</sup> CHARMM,<sup>21</sup> GROMOS,<sup>22</sup> and OPLS-AA<sup>23</sup> and widely used to model biomolecular systems. The total energy of the

system can be separated into the total kinetic energy and the total potential energy.

$$E_{total} = E_{Kin} + E_{Pot} = \left(\frac{mv^2}{2}\right) + (E_{bonded} + E_{non-bonded}) \quad (\text{Eq.2.24})$$

where  $m$  is the mass,  $v$  is the velocity

The total potential energy can also be divided into two parts:  $E_{bonded}$  and  $E_{non-bonded}$  part. All bonding energies can be expressed by the following equation:

$$E_{bonded} = \sum_{all\ bonds} k_r(\Delta r)^2 + \sum_{all\ angles} k_\theta(\Delta\theta)^2 + \sum_{all\ torsions} k_\omega(1 + \cos(n\omega - \varphi)) \quad (\text{Eq.2.25})$$

where  $k_r, k_\theta, k_\omega$  are bond, bond angle, torsion angle force constants, corresponding to  $r$  distance,  $\theta$  bond angle,  $\omega$  torsion angle equilibrium positions,  $n$  and  $\varphi$  are periodicity and phase

The bond and the bond angle terms are usually described by harmonic (parabolic) equations whereas the torsion (dihedral) term is represented using a Fourier expansion since it is most often periodic.

The non-bonding term consists of the Coulomb potential and the Leonard-Jones potential as mentioned (Eq.2.26).

$$E_{non-bonded} = E_{Coulomb} + V_{LJ} = \left(\sum \frac{|q_1q_2|}{4\pi\epsilon_0 r}\right) + \left(\epsilon \left[\left(\frac{R}{r}\right)^{12} - \left(\frac{R}{r}\right)^6\right]\right) (\text{Eq.2.26})$$

### 2.1.2.3. Metals and Force Fields.

At present, classical force fields have all the parameters (standardized) for organic systems, but not for most of metal-organic systems. Therefore, when we study metal-containing systems with classical force fields, the derivation of non-standard parameters (force constants, equilibrium geometries and atomic charges) for metal centers is needed. These parameters can be derived from QM calculations (so-called the Seminario method).<sup>24</sup> In this method, bond, bond angle and torsion angle force constants are derived in the following way:

(i) bond force constants: the interatomic force constant is obtained directly from Cartesian second derivatives (Hessians) computed at QM level. The force constant matrix calculated at full QM level can be written as

$$\begin{bmatrix} \frac{\partial^2 E}{\partial x_i \partial x_j} & \cdots & \frac{\partial^2 E}{\partial x_i \partial z_j} \\ \vdots & \ddots & \vdots \\ \frac{\partial^2 E}{\partial z_i \partial x_j} & \cdots & \frac{\partial^2 E}{\partial z_i \partial z_j} \end{bmatrix} = [k_{ij}] \quad (\text{Eq.2.27})$$

where  $i$  is the atom 1,  $j$  is the atom 2

Then, the bond force constant between  $i$  (atom 1) and  $j$  (atom 2) is given by the equation 2.28:

$$k_{ij} = \sum_{n=1}^3 \lambda_n^{ij} |\hat{u}^{ij} \cdot \hat{v}_n^{ij}| \quad (\text{Eq.2.28})$$

where  $\hat{u}^{ij}$  is the unit vector;  $\lambda_n^{ij}$  is the eigenvalue and  $\hat{v}_n^{ij}$  is the eigenvector of  $[k_{ij}]$  matrix.

(ii) bond angle force constants: by assuming that two bonds as two springs connected in series, the angle force constant can be approximated by the following equation:

$$k_\theta = \left( \frac{1}{r_{ij}^2 \sum_{n=1}^3 \lambda_n^{ij} |(\hat{u}^N \times \hat{u}^{ij}) \cdot \hat{v}_n^{ij}|} + \frac{1}{r_{kj}^2 \sum_{n=1}^3 \lambda_n^{kj} |(\hat{u}^{kj} \times \hat{u}^N) \cdot \hat{v}_n^{kj}|} \right)^{-1} \quad (\text{Eq.2.29})$$

where  $i$  is the atom 1,  $j$  is the atom 2,  $k$  is the is atom 3,  $r_{ij}$  is the bond length,  $\hat{u}^N$  is the unit vector  $\perp ijk$

(iii) torsion angle force constants: using the same approximation, the torsion (dihedral) angle force constant can also be obtained (Eq.2.30).

$$k_\omega = \left( \frac{1}{r_{ij}^2 |\hat{u}^{ij} \times \hat{u}^{jk}|^2 \sum_{n=1}^3 \lambda_n^{ij} |(\hat{u}^N)_{ijk} \cdot \hat{v}_n^{ij}|} + \frac{1}{r_{lk}^2 |\hat{u}^{jk} \times \hat{u}^{kl}|^2 \sum_{n=1}^3 \lambda_n^{lk} |(\hat{u}^N)_{jkl} \cdot \hat{v}_n^{lk}|} \right)^{-1} \quad (\text{Eq.2.30})$$

where  $\hat{u}^N_{ijk} = \frac{\hat{u}^{kj} \times \hat{u}^{ij}}{|\hat{u}^{kj} \times \hat{u}^{ij}|}$  and  $\hat{u}^N_{jkl} = \frac{\hat{u}^{lk} \times \hat{u}^{jk}}{|\hat{u}^{lk} \times \hat{u}^{jk}|}$

Atomic charges derived from electrostatic potential computed at QM level are considered to be suitable for reproducing intermolecular interactions. However, direct use of these charges for MD simulations may cause some problems if their magnitudes are large or affected significantly by conformational changes. Therefore, in order to fix these problems, a restrained electrostatic potential (RESP) fitting procedure was introduced

and has been used broadly for MD simulations.<sup>25</sup> In this procedure, the classical electrostatic potential ( $V_i^C$ ) generated by charges is fitted to the pre-calculated QM molecular electrostatic potential ( $V_i^{QM}$ ) using the method of least-squares. The fitting scoring function ( $\chi_{ESP}^2$ ) is thus defined as follows:

$$\chi_{ESP}^2 = \sum_i (V_i^{QM} - V_i^C)^2 \quad (\text{Eq.2.31})$$

where  $V_i^C$  is the classical electrostatic potential,  $V_i^{QM}$  is QM molecular electrostatic potential.

Then, a penalty function ( $\chi_{restrain}^2$ ) is added to the fitting scoring function

$$\chi_{RESP}^2 = \chi_{ESP}^2 + \chi_{restrain}^2 = \sum_i (V_i^{QM} - \sum_j \frac{q_j}{r_{ij}})^2 + \chi_{restrain}^2 \quad (\text{Eq.2.32})$$

where  $q_j$  is the charge  $r_{ij}$  is the distance.

The penalty function is a hyperbolic function defined by a weight factor,  $c$ , and the ‘‘tightness’’ of the hyperbola,  $b$ , expressed by Eq.2.33.

$$\chi_{RESP}^2 = \chi_{ESP}^2 + \chi_{restrain}^2 = \chi_{ESP}^2 + c \sum_j ((q_j^2 + b^2)^{\frac{1}{2}} - b) \quad (\text{Eq.2.33})$$

where  $c$  is the weight factor and  $b$  is the ‘‘tightness’’ of the hyperbola

The hyperbolic restraint towards to the charges that are not well-defined statistically.

Recently, a new model, W-RESP<sup>26</sup> has been proposed using a normalized  $\chi_{ESP}^2$  function by the total number of grid points ( $N$ ), for the  $\chi_{ESP}^2$  part and a weighted harmonic restraint function for the  $\chi_{restrain}^2$  part of the fitting scoring function. It showed an improvement of the performance of the nucleic acid force fields, especially the behavior of terminal base pairs in MD simulations.

## 2.1.3. QM/MM.

### 2.1.3.1 Introduction to QM/MM.

Quantum mechanics/molecular mechanics (QM/MM) method is a general hybrid method. Since there is a limitation for modeling large systems at

full QM level, this hybrid approach is an efficient way of modelling large systems such as the complete enzyme-substrate complex with the surrounding solvent environment.<sup>27</sup> In this formalism, the entire system is usually divided into two parts: (i) the key part and (ii) the rest. The key part of the system is treated with the accurate high-level QM method while the remaining part of the system is treated with the less accurate MM method. In principle, it can be divided into more than two parts (for example: QM1/QM2/MM for three parts, etc.). In such cases, the middle parts are treated with in-between accurate methods. The interaction of the key part with the remaining one can also be approximated by another method (low-cost QM or semi-empirical). It is called a dual level QM1:QM2/MM scheme.<sup>28</sup> Therefore, in addition to the choice of particular method, defining separate regions of the system to be treated with different level of theories and evaluating the interaction between the regions are of concern to this “generic” method. Computing the total energy of the entire system under this formalism can thus be in different ways.

### 2.1.3.2. Additive and subtractive schemes.

The total energy of the whole system can be calculated with either subtractive or additive schemes. In the former, it is obtained by adding the QM energy of the QM region to the energy of the entire system calculated using MM while the MM energy of the QM region is subtracted (Eq.2.34). In the latter scheme, the total energy has three terms: (i) the QM energy of the QM region, (ii) the MM energy of the MM region, and (iii) the interaction energy between two regions (Eq.2.35).

$$E = E^{MM}(\text{entire system}) + E^{QM}(\text{QM region}) - E^{MM}(\text{QM region}) \text{ (Eq.2.34)}$$

$$E = E^{QM}(\text{QM region}) + E^{MM}(\text{MM region}) + E^{Interaction}(\text{QM/MM}) \text{ (Eq.2.35)}$$

The subtractive scheme evaluates the effect of the remaining part on the key part with an inexpensive MM method. It is the so-called Integrated Molecular Orbital and Molecular Mechanics (IMOMM)<sup>29</sup> method which can be considered as the first generation of the *n*-layer ONIOM method

(ONIOM<sub>n</sub>, Our own *N*-layered Integrated molecular Orbital and molecular Mechanics).<sup>28</sup>

In general, the ONIOM method includes the IMOMM as well as the IMOMO (Integrated Molecular Orbital and Molecular Orbital) method.<sup>30</sup> One of the important schemes implemented in the ONIOM method is the electronic embedding (ONIOM-EE).<sup>31-33</sup> It computes the QM/MM electrostatic interactions and the QM density self consistently, reflecting the polarization effect from the MM remaining part on the QM key part of the system. This is crucial for computing energies of the highly charged host-guest complexes with the ONIOM (QM/MM) method.

To include the solvation effect in the ONIOM method, the explicit and implicit approaches can be used. In the former, the solvent molecules can enter and leave the QM key region during the simulation. One way of solving this issue is defining a switching shell between the QM and MM regions which is called the ONIOM-XS method.<sup>34</sup> In the latter approach, the entire system is defined as a solute and the integrated solute charge distribution is computed with the ONIOM extrapolative scheme (ONIOM-PCM).<sup>35,36</sup> As an example, the geometry of the transition state for alkyl-alkyl reductive elimination from a Au(III) phosphine complex encapsulated by the [Ga<sub>4</sub>L<sub>6</sub>]<sup>12-</sup> metallocage optimized with the 2-layer ONIOM(QM/MM)-EE-PCM method is shown below (Figure 2.6).



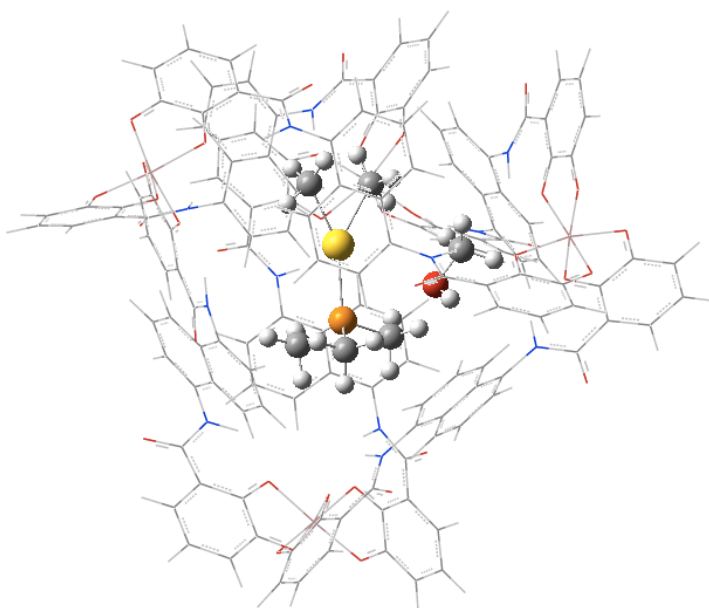


**Figure 2.6.** 2-layer ONIOM (QM/MM)-EE-PCM optimized geometry of the encapsulated transition state for alkyl-alkyl reductive elimination from  $[\text{PMe}_3\text{Au}(\text{MeOH})(\text{CH}_3)_2]^+$  complex encapsulated in  $[\text{Ga}_4\text{L}_6]^{12-}$ .

## 2.2 Exploring the conformational space.

### 2.2.1. Introduction.

Finding the lowest energy point on the energy landscape can be similar to looking for a needle in a haystack depending on the system. When we build up a molecular system as an input for simulation, it can be, in principle, in the conformational space (Figure 2.7).

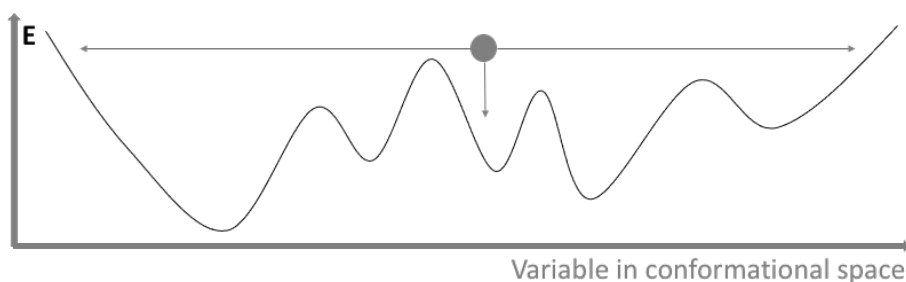


**Figure 2.7.** General representation of energy in conformational space.

Thus, exploring the conformational space is important for molecular modeling. However, it is often simple for small systems such as isolated small molecules, it can be difficult for large systems. Several effective methods have been used for this exploration: (i) Monte Carlo method, generating a thermal population of geometries according to a Boltzmann distribution (ii) simulated annealing, heating the system up and then cooling it down very slowly over time, (iii) molecular dynamics, solving classical equations of motion, and (iv) genetic algorithm, selecting and evolving “good” points and their properties.<sup>37–40</sup>

In this work, either restrained or unrestrained classical molecular dynamics has been performed for exploring the conformational space and simulating dynamic processes.

## 2.2.2 Molecular Dynamics.

### 2.2.2.1. Introduction to molecular dynamics.

The molecular dynamics simulation is considered as one of the key methods for studying a molecular process over time. Its general procedure can be described as follows (Figure 2.8):

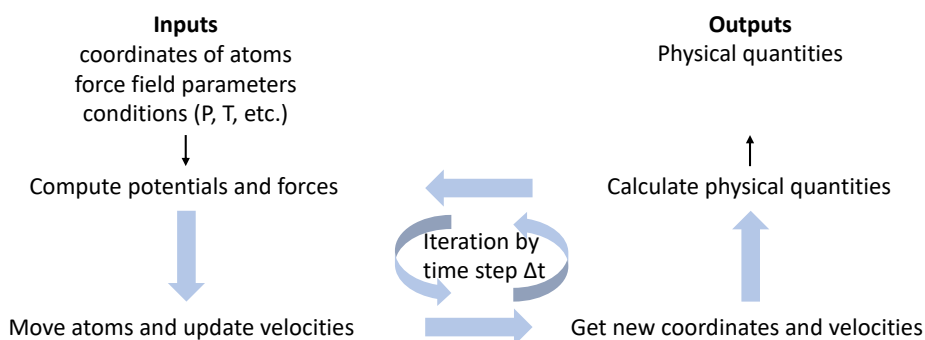


**Figure 2.8.** Schematic representation of classical molecular dynamic simulation procedure.

It starts computing the potentials and forces using classical equations, and afterwards new coordinates and velocities are obtained from which the physical quantities can be calculated. To calculate the velocity, most of the

simulation programs use the velocity verlet procedure,<sup>41</sup> which is a velocity form of the verlet algorithm.<sup>42</sup> This procedure is shown below.

1. To move atoms within a time step

$$r(t + \Delta t) = r(t) + v(t)\Delta t + \frac{1}{2}a(t)\Delta t^2 + \dots \quad (\text{Eq.2.36})$$

2. To calculate forces at  $t + \Delta t$

3. To obtain new velocities using the equation 2.37

$$v(t + \Delta t) = v(t) + \frac{\Delta t}{2}a(t) + \frac{\Delta t}{2}a(t + \Delta t) + \dots \quad (\text{Eq.2.37})$$

4. Repeat the procedure

The velocity equation (Eq.2.37) can be derived as follows:

Taylor expansion for atom position:

$$r(t + \Delta t) = r(t) + \frac{\partial r}{\partial t}(t)\Delta t + \frac{1}{2}\frac{\partial^2 r}{\partial t^2}(t)\Delta t^2 + \dots \quad (\text{Eq.2.38})$$

Taylor expansion for atom velocity:

$$v(t + \Delta t) = v(t) + \frac{\partial v}{\partial t}(t)\Delta t + \frac{1}{2}\frac{\partial^2 v}{\partial t^2}(t)\Delta t^2 + \dots \quad (\text{Eq.2.39})$$

Taylor expansion for atom acceleration:

$$\frac{\partial v}{\partial t}(t + \Delta t) = \frac{\partial v}{\partial t}(t) + \frac{\partial^2 v}{\partial t^2}(t)\Delta t + \dots \quad (\text{Eq.2.40})$$

Now, if we multiply the equation 2.40 by  $\frac{\Delta t}{2}$

$$\frac{\Delta t}{2} \cdot \frac{\partial v}{\partial t}(t + \Delta t) = \frac{\Delta t}{2} \cdot \frac{\partial v}{\partial t}(t) + \frac{\Delta t}{2} \cdot \frac{\partial^2 v}{\partial t^2}(t)\Delta t + \dots \quad (\text{Eq.2.41})$$

Then, rearrange it:

$$\frac{1}{2} \cdot \frac{\partial^2 v}{\partial t^2}(t)\Delta t^2 = \frac{\Delta t}{2} \cdot \frac{\partial v}{\partial t}(t + \Delta t) - \frac{\Delta t}{2} \cdot \frac{\partial v}{\partial t}(t) + \dots \quad (\text{Eq.2.42})$$

Finally, substitute the part of second derivative of velocity in the equation 2.42 into the equation 2.39:

$$\begin{aligned} v(t + \Delta t) &= v(t) + \frac{\partial v}{\partial t}(t)\Delta t + \frac{\Delta t}{2} \cdot \frac{\partial v}{\partial t}(t + \Delta t) - \frac{\Delta t}{2} \cdot \frac{\partial v}{\partial t}(t) + \dots \\ &= v(t) + \frac{1}{2}\frac{\partial v}{\partial t}(t)\Delta t + \frac{\Delta t}{2} \cdot \frac{\partial v}{\partial t}(t + \Delta t) + \dots \end{aligned} \quad (\text{Eq.2.43})$$

If we use the classical definition of acceleration for the equation 2.43, it is the equation 2.37 to update velocities in the velocity verlet algorithm.<sup>41</sup>

Until the system reaches to an equilibrium, the procedure may need to be iterated millions of times and it can be done using GPUs. In principle, such long plain (unrestrained) molecular dynamic simulation should guide us to the lowest energy point in certain conformational space.

### 2.2.2.2. Umbrella sampling method.

There can be significant energy barriers between different states. For these cases, restrained molecular dynamic simulations can be used for modeling the whole transition process from one state to another. In particular, umbrella sampling approach is commonly used for such purposes.<sup>43,44</sup> In this approach, a chosen variable (reaction coordinate) is fixed at certain values ( $r_1$ ,  $r_2$ , etc.) by harmonic functions ( $U_i(r)=k_r(r-r_i)^2$ , umbrella restraint). This leads to many restrained classical molecular dynamic simulations which are called umbrella windows (Figure 2.9).

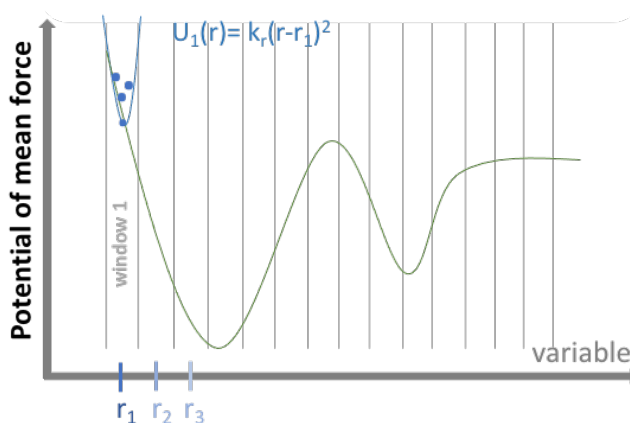


**Figure 2.9.** The generic example of umbrella sampling simulations.

The partial overlapping of the neighboring umbrella windows indicates an adequate sampling along the regions of the potential of mean force. To construct the energetics of process, either the weighted histogram analysis method or the thermodynamic integration approach can be employed.<sup>44</sup>

### 2.2.2.3 The APR method.

For the restrained molecular dynamics simulations, there are many different ways for setting the restraints up with a harmonic potential. One of them designed specifically for host-guest complexes is the APR method.<sup>45</sup> The general setup and details of the sampling simulations are shown below (Figure 2.10).

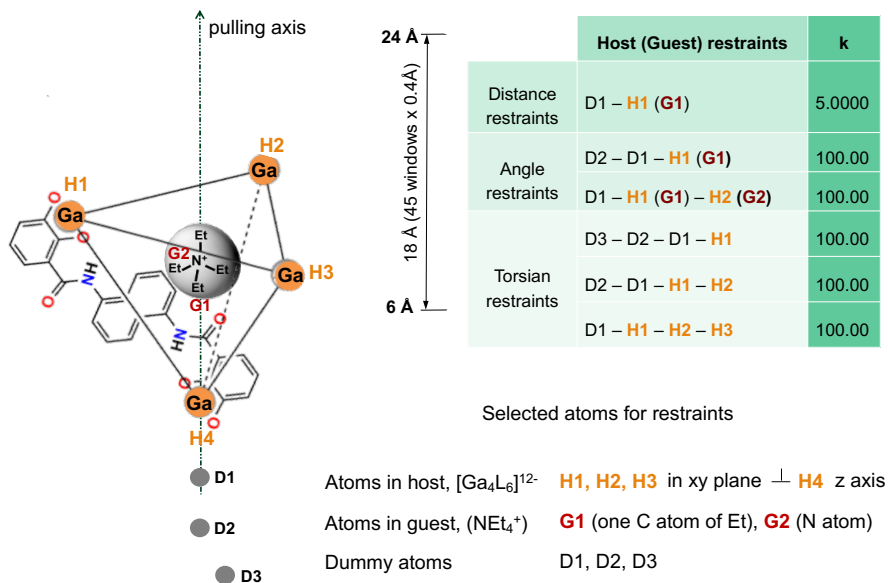


**Figure 2.10.** Setup example of the APR method for  $\text{NEt}_4^+\text{@[Ga}_4\text{L}_6]^{12-}$ .

This approach uses three dummy atoms ( $\text{D}_1$ ,  $\text{D}_2$ ,  $\text{D}_3$ ) to make all restraints of the guest and the host. Every sampling window is simulated at least 2.5 ns depending on the standard error of the mean in order to reduce computational time (Table 2.1).

**Table 2.1.** Simulation steps in each sampling window of the APR method.

1	Minimizing 50000 cycles,
2	Running 1 ps NVT at 10 K,
3	Heating the system from 10 K to 298.15 K within 100 ps,
4	Equilibrating the system under constant pressure 50 NPT cycles;
5	Production NPT from 2.5 ns to 25 ns depending on the standard error of the mean (SEM) of the restraint forces, the SEM threshold is 0.100

It has been applied successfully to host-guest and protein-ligand systems and thus suggested to evaluate and optimize force fields for host-guest binding calculations.<sup>46,47</sup>

#### 2.2.2.4. Weighed histogram analysis method.

However, the absolute binding Gibbs energy is calculated with the APR method, the energetics of whole process is not. The energetics of the dynamic process can be obtained as the potential of mean force (PMF) along the chosen variable with the weighed histogram analysis method (WHAM).<sup>48</sup> In this method, the PMF is constructed from the sampling data contain the force constant, the fixed and actual variables by solving the following equations iteratively.<sup>49</sup>

$$P(r) = \frac{\sum_{i=1}^N n_i(r)}{\sum_{i=1}^N N_i \exp\left(\frac{[F_i - U_i(r)]}{k_B T}\right)} \quad (\text{Eq.2.44})$$

where,  $P(r)$  is the unbiased probability,  $n_i(r)$  is the number of counts in histogram bin,  $U_i(r)$  is the biasing potential,  $F_i$  is the relative free energy,  $N$  is the number of simulation.

$$F_i = -k_B T \ln\left(\sum P(r) \exp\left(\frac{-U_i(r)}{k_B T}\right)\right) \quad (\text{Eq.2.45})$$

## 2.3. Specific additional aspects for metallo cage embedded catalysis.

### 2.3.1. Calculating the cavity volume of metallo cage.

The cavity of the host molecule can provide the complete change of microenvironment for the guest molecule. Its volume is one of the most important descriptions of the host. In general, it can be calculated with different methods. Several programs and online servers have been developed for this purpose. Examples include CAVER Analyst,<sup>50</sup> VOIDOO,<sup>51</sup> McVol,<sup>52</sup> CASTp,<sup>53</sup> BetaCavityWeb,<sup>54</sup> CavityPlus,<sup>55</sup> etc.<sup>56,57</sup> Most of them are designed for proteins. The CAVER Analyst is one of the few software tools that calculate the cavity volume for metal-containing systems. It calculates the cavity as empty space that can be occupied by the defined probe but from which the probe can not escape and visualized their solvent-excluded surface, SES (Figure 2.11).

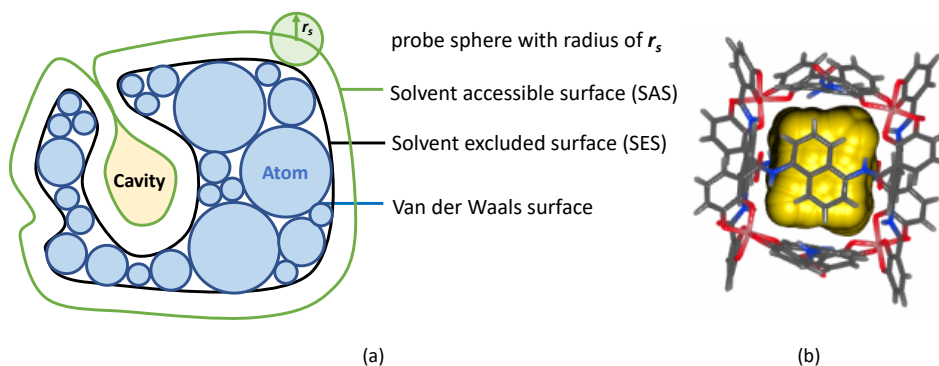


**Figure 2.11.** (a) schematic representation of the rolling probe, SAS, SES, and Van der Waals surfaces; (b) example of the visualization of the cavity calculated with default probe radii using the CAVER Analyst program.<sup>50</sup>

### 2.3.2. Counting the number of solvent molecules encapsulated.

Along with the guest molecule, the solvent molecule can be found in the cavity of the host molecule depending on their nature and size. In such cases, the encapsulated solvent molecules can be crucial for the process. Thus, determining the solvent molecules inside the host can be one of the important stages for investigating the host-guest systems. In principle, long molecular dynamic simulations should provide the information about the solvent molecules encapsulated by the host. However, a procedure that counts the solvent molecules in the cavity of the host during the MD trajectory has not currently been developed. But if we approximate the cavity for counting the solvent molecules in the host during the MD trajectory by a polyhedron defined by selected atoms of the host, it can be done using PyChimera with open-source libraries (NumPy, SciPy, ConvexHull, Delaunay).<sup>58–63</sup> In particular, we used a python script written by Dr. Jaime Rodriguez-Guerra with PyChimera. An example polyhedron is illustrated by its edges in Figure 2.12.

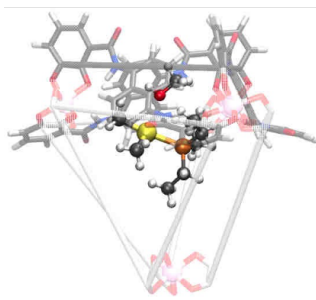


**Figure 2.12.** The selected edges of the defined polyhedron for counting the solvent molecules in the  $[\text{Ga}_4\text{L}_6]^{12-}$ .

It is defined by the C atoms connected to the O atoms bonded to Ga(III) centers of the  $[\text{Ga}_4\text{L}_6]^{12-}$  which are selected to be its vertices.



## References:

- (1) Hawking, S. A Brief History of Time: From Big Bang to Black Holes, **1993**.
- (2) Helgaker, T.; Jorgensen, P.; Olsen, J. Molecular Electronic-Structure Theory, **2000**, Wiley.
- (3) Hohenberg, P.; Kohn, W. Inhomogeneous Electron Gas. *Phys. Rev.* **1964**, *136*, B864.
- (4) Kohn, W.; Sham, L. J. Self-Consistent Equations Including Exchange and Correlation Effects. *Phys. Rev.* **1965**, *140*, A1133.
- (5) Becke, A. D. Density-Functional Thermochemistry. III. The Role of Exact Exchange. *J. Chem. Phys.* **1993**, *98*, 5648–5652.
- (6) Lee, C.; Yang, W.; Parr, R. G. Development of the Colle-Salvetti Correlation-Energy Formula into a Functional of the Electron Density. *Phys. Rev. B*, **1988**, *37*, 785–789.
- (7) Grimme, S. Supramolecular Binding Thermodynamics by Dispersion-Corrected Density Functional Theory. *Chem. Eur. J.* **2012**, *18*, 9955–9964.
- (8) Chai, J-D.; Head-Gordon, M. Long-Range Corrected Hybrid Density Functionals with Damped Atom–Atom Dispersion Corrections. *Phys.Chem.Chem.Phys*, **2008**, *10*, 6615.
- (9) Luchini, G.; Alegre-Requena, J. V.; Funes-Ardoiz, I.; Paton, R. S. GoodVibes: Automated Thermochemistry for Heterogeneous Computational Chemistry Data, *F1000Research*, **2020**, 9.
- (10) Axilrod, B. M.; Teller, E. Interaction of the van Der Waals Type Between Three Atoms. *Journal of Chemical Physics*, **1943**, *11*, 299.
- (11) Axilrod, B. M. Triple-Dipole Interaction. Theory. *Journal of Chemical Physics*, **1951**, *19*, 719.
- (12) Gaussian 09, Revision D.01, M. J. Frisch, G. W. Trucks, H. B. Schlegel, G. E. Scuseria, M. A. Robb, J. R. Cheeseman, G. Scalmani, V. Barone, B. Mennucci, G. A. Petersson, H. Nakatsuji, M. Caricato, X. Li, H. P. Hratchian, A. F. Izmaylov, J. Bloino, G. Zheng, J. L. Sonnenberg, M. Hada, M. Ehara, K. Toyota, R. Fukuda, J. Hasegawa, M. Ishida, T. Nakajima, Y. Honda, O. Kitao, H. Nakai, T. Vreven, J. A. Montgomery, Jr., J. E. Peralta, F. Ogliaro, M. Bearpark, J. J. Heyd, E. Brothers, K. N. Kudin, V. N. Staroverov, T. Keith, R. Kobayashi, J. Normand, K. Raghavachari, A. Rendell, J. C. Burant, S. S. Iyengar, J. Tomasi, M. Cossi, N. Rega, J. M. Millam, M. Klene, J. E. Knox, J. B. Cross, V. Bakken, C. Adamo, J. Jaramillo, R. Gomperts, R. E. Stratmann, O. Yazyev, A. J. Austin,

- R. Cammi, C. Pomelli, J. W. Ochterski, R. L. Martin, K. Morokuma, V. G. Zakrzewski, G. A. Voth, P. Salvador, J. J. Dannenberg, S. Dapprich, A. D. Daniels, O. Farkas, J. B. Foresman, J. V. Ortiz, J. Cioslowski, D. J. Fox, Gaussian, Inc., Wallingford CT, **2013**.
- (13) Ho, J.; Klamt, A.; Coote, M. L. Comment on the Correct Use of Continuum Solvent Models. *J. Phys. Chem A*, **2010**, *114*, 3442–13444.
- (14) Marenich, A. V; Cramer, C. J.; Truhlar, D. G. Universal Solvation Model Based on Solute Electron Density and on a Continuum Model of the Solvent Defined by the Bulk Dielectric Constant and Atomic Surface Tensions. *J. Phys. Chem. B* **2009**, *113*, 6378–6396.
- (15) Siegbahn, P. E. M.; Crabtree, R. H. Modeling the Solvent Sphere: Mechanism of the Shilov Reaction. *J Am Chem Soc*, **1996**, *118*, 4442–4450.
- (16) Díez, J.; Gimeno, J.; Lledós, A.; Suárez, F. J.; Vicent, C. Imidazole Based Ruthenium(IV) Complexes as Highly Efficient Bifunctional Catalysts for the Redox Isomerization of Allylic Alcohols in Aqueous Medium: Water as Cooperating Ligand. *ACS Catal*, **2012**, *2*, 2087-2099.
- (17) Pavlova, A.; Rösler, E.; Meijer, E. J. Mechanistic Aspects of Using Formate as a Hydrogen Donor in Aqueous Transfer Hydrogenation. *ACS Catal*, **2016**, *6*, 5350–5358.
- (18) Kelly, C. P.; Cramer, C. J.; Truhlar, D. G. Adding Explicit Solvent Molecules to Continuum Solvent Calculations for the Calculation of Aqueous Acid Dissociation Constants. *J. Phys. Chem. A* **2006**, *110*, 2493–2499.
- (19) Jones, J. E. On the Determination of Molecular Fields. II. From the Equation of State of a Gas. *Proceedings of the Royal Society of London. Series A, Containing Papers of a Mathematical and Physical Character*, **1924**, *106*, 463–477.
- (20) Salomon-Ferrer, R.; Case, D. A.; Walker, R. C. An Overview of the Amber Biomolecular Simulation Package. *WIREs Comput, Mol. Sci.* **2013**, *3*, 198-210.
- (21) Brooks, B. R.; Brucoleri, R. E.; Olafson, B. D.; States, D. J.; Swaminathan, S.; Karplus. M. CHARMM: A Program for Macromolecular Energy, Minimization, and Dynamics Calculations. *J. Comp. Chem*, **1983**, *4*, 187-217.
- (22) Scott, W. R. P.; Huenenberger, P. H.; Tironi, I. G.; Mark, A. E.; Billeter, S. R.; Fennel, J.; Torda, A. E.; Huber, T.; Krueger, P.; van Gunsteren, W. F. The GROMOS Biomolecular Simulation Program

- Package, *J. Phys. Chem. A*, **1999**, *103*, 3596–3607.
- (23) Jorgensen, W. L.; Tirado-Rives, J. The OPLS Force Field for Proteins. Energy Minimizations for Crystals of Cyclic Peptides and Crambin. *J. Am. Chem. Soc.*, **1988**, *110*, 1657–1666.
- (24) Seminario, J. M. Calculation of Intramolecular Force Fields from Second-Derivative Tensors. *Int. J. Quantum Chem.* **1996**, *60*, 1271–1277.
- (25) Bayly, C. I.; Cieplak, P.; Cornell, W. D.; Kollman, P. A. A Well-Behaved Electrostatic Potential Based Method Using Charge Restraints for Deriving. *J. Phys. Chem.* **1993**, *97*, 10269–10280.
- (26) Janeček, M.; Kührová, P.; Mlýnský, V.; Otyepka, M.; Šponer, J.; Banáš, P. W-RESP: Well-Restrained Electrostatic Potential Derived Charges. Revisiting the Charge Derivation Model. *J. Chem. Theory Comput.* **2021**, *17*, 3495–3509.
- (27) Warshel, A.; Levitt, M. Theoretical Studies of Enzymic Reactions: Dielectric, Electrostatic and Steric Stabilization of the Carbonium Ion in the Reaction of Lysozyme. *Journal of Molecular Biology*, **1976**, *103*, 227-249.
- (28) Chung, L. W.; Sameera, W. M. C.; Ramozzi, R.; Page, A. J.; Hatanaka, M.; Petrova, G. P.; Harris, T. V.; Li, X.; Ke, Z.; Liu, F.; Li, H-B.; Ding, L.; Morokuma, K. The ONIOM Method and Its Applications. *Chem. Rev.* **2015**, *115*, 5678–5796.
- (29) Maseras, F.; Morokuma, K. IMOMM: A New Integrated *ab initio* + Molecular Mechanics Geometry Optimization Scheme of Equilibrium Structures and Transition States. *J. Comput. Chem.* **1995**, *16*, 1170-1179.
- (30) Humbel, S.; Sieber, S.; Morokuma, K. The IMOMO Method: Integration of Different Levels of Molecular Orbital Approximations for Geometry Optimization of Large Systems: Test for *n*-butane Conformation and S<sub>N</sub>2 Reaction: RCl+Cl<sup>-</sup>, *J. Chem. Phys.* **1996**, *105*, 1959.
- (31) Vreven, T.; Byun, K. S.; Komafomi, I.; Dapprich, S.; Montgomery, J. A., Jr.; Morokuma, K.; Frisch, M. J. Combining Quantum Mechanics Methods with Molecular Mechanics Methods in ONIOM, *J. Chem. Theory Comput.* **2006**, *2*, 815-826.
- (32) Vreven, T.; Morokuma, K. Investigation of the S<sub>0</sub> → S<sub>1</sub> Excitation in Bacteriorhodopsin with the ONIOM(MO:MM) Hybrid Method, *Theor. Chem. Acc.* **2003**, *109*, 125-132.
- (33) Bakowies, D.; Thiel, W. Hybrid Models for Combined Quantum Mechanical and Molecular Mechanical Approaches. *J. Phys. Chem.*

- 1996**, *100*, 10580.
- (34) Kerdcharoen, T.; Morokuma, K. ONIOM-XS: An Extension of the ONIOM Method for Molecular Simulation in Condensed Phase. *Chem. Phys. Lett.* **2002**, *355*, 257-262.
- (35) Miertuš, S.; Scrocco, E.; Tomasi, J. Electrostatic Interaction of a Solute with a Continuum. A Direct Utilizaion of *ab initio* Molecular Potentials for the Prevision of Solvent Effects. *Chem. Phys.* **1981**, *55*, 117-129.
- (36) Tomasi, J.; Mennucci, B.; Cammi, R. Quantum Mechanical Continuum Solvation Models. *Chem. Rev.* **2005**, *105*, 2999-3094.
- (37) Frenkel, D.; Smit, B. Understanding Molecular Simulation: From Algorithms to Applications, *Academic Press*, **2002**.
- (38) Rapaport, D. C. The Art of Molecular Dynamics Simulation, *Cambridge University Press*, **2004**.
- (39) Kirkpatrick, S.; Gelatt Jr, C. D.; Vecchi, M. P. Optimization by Simulated Annealing. *Science*, **1983**, *220*, 671–680.
- (40) Katoch, S.; Chauhan, S. S.; Kumar, V. A Review on Genetic Algorithm: Past, Present, and Future. *Multimed Tools Appl*, **2021**, *80*, 8091–8126.
- (41) Swope, W, C.; Andersen, H. C.; Berens, P. H.; Wilson, K. R. A Computer Simulation Method for the Calculation of Equilibrium Constants for the Formation of Physical Clusters of Molecules: Application to Small Water Clusters. *The Journal of Chemical Physics. J. Chem. Phys.* **1982**, *76*, 637.
- (42) Verlet, L. Computer Experiments on Classical Fluids. I. Thermodynamical Properties of Lennard–Jones Molecules. *Physical Review*, **1967**, *159*, 98–103.
- (43) Torrie, G. M.; Valleau, J. P. Nonphysical Sampling Distributions in Monte Carlo Free-Energy Estimation: Umbrella Sampling. *J. Comput. Phys.* **1977**, *23*, 187–199.
- (44) Kästner, J. Umbrella Sampling. *Wiley Interdiscip. Rev. Comput. Mol. Sci.* **2011**, *1*, 932–942.
- (45) Yin, J.; Henriksen, N. M.; Slochower, D. R.; Gilson, M. K. The SAMPL5 Host–Guest Challenge: Computing Binding Free Energies and Enthalpies from Explicit Solvent Simulations by the Attach-Pull-Release (APR) Method. *J. Comput. Aided. Mol. Des.* **2017**, *31*, 133–145.
- (46) Heinzelmann, G.; Henriksen, N. M.; Gilson, M. K. Attach-Pull-Release Calculations of Ligand Binding and Conformational Changes on the First BRD4 Bromodomain. *J. Chem. Theory*

- Comput*, **2017**, *13*, 3260–3275.
- (47) Yin, J.; Henriksen, N. M.; Slochower, D. R.; Gilson, M. K. AMBER Advanced Tutorial 29 Computing Binding Free Energy and Binding Enthalpy Using the Attach-Pull-Release (APR) Method Example. **2016**, <https://ambermd.org/tutorials/advanced/tutorial29/>.
- (48) Kumar, S.; Rosenberg, J. M.; Bouzida, D.; Swendsen, R. H.; Kollman, P. A. The Weighted Histogram Analysis Method for Free-energy Calculations on Biomolecules. I. The Method. *J. Comput. Chem.* **1992**, *13*, 1011–1021.
- (49) Grossfield, Alan, “WHAM: The Weighted Histogram Analysis Method”, [http://membrane.urmc.rochester.edu/wordpress/?page\\_id=126](http://membrane.urmc.rochester.edu/wordpress/?page_id=126).
- (50) Kozlikova, B.; Sebestova, E.; Sustr, V.; Brezovsky, J.; Strnad, O.; Daniel, L.; Bednar, D.; Pavelka, A.; Manak, M.; Bezdeka, M.; et al. CAVER Analyst 1.0: Graphic Tool for Interactive Visualization and Analysis of Tunnels and Channels in Protein Structures. *Bioinformatics* **2014**, *30*, 2684–2685.
- (51) Kleywegt, G. J.; Jones, T. A. Detection, Delineation, Measurement and Display of Cavities in Macromolecular Structures. *Acta Crystallogr D Biol Crystallogr*, **1994**, *50*, 78–185.
- (52) Till, M. S.; Ullmann, G. M. McVol - A Program for Calculating Protein Volumes and Identifying Cavities by a Monte Carlo Algorithm. *J. Mol. Mod*, **2010**, *16*, 419-429.
- (53) Liang, J.; Edelsbrunner, H.; Fu, P.; Sudhakar, P. V.; Subramaniam, S. Analytical Shape Computation of Macromolecules: II. Inaccessible Cavities in Proteins. *Proteins*, **1998**, *33*, 18–29.
- (54) Kim, J. K.; Cho, Y.; Lee, M.; Laskowski, R. A.; Ryu, S. E.; Sugihara, K.; Kim, D. S. BetaCavityWeb: A Webserver for Molecular Voids and Channels. *Nucleic Acids Res.* **2015**, *43*, W413–W418.
- (55) Xu, Y.; Wang, S.; Hu, Q.; Gao, S.; Ma, X.; Zhang, W.; Shen, Y.; Chen, F.; Lai, L.; Pei, J. CavityPlus: A Web Server for Protein Cavity Detection with Pharmacophore Modelling, Allosteric Site Identification and Covalent Ligand Binding Ability Prediction. *Nucleic Acids Res.* **2018**, *46*, W374–W379.
- (56) Chakravarty, S.; Bhinge, A.; Varadarajan, R. A. Procedure for Detection and Quantitation of Cavity Volumes Proteins. Application to Measure the Strength of the Hydrophobic Driving Force in Protein Folding. *J Biol Chem*, **2002**, *277*, 31345–31353.
- (57) Liang, J.; Edelsbrunner, H.; Woodward, C. Anatomy of Protein

- Pockets and Cavities: Measurement of Binding Site Geometry and Implications for Ligand Design, *Protein Sci*, **1998**, *7*, 1884–1897.
- (58) Rodríguez-Guerra Pedregal, J.; Maréchal, J. D. PyChimera: Use UCSF Chimera Modules in Any Python 2.7 Project. *Bioinformatics* **2018**, *34*, 1784–1785.
- (59) Harris, C. R.; Millman, K. J.; van der Walt, S. J.; Gommers, R.; Virtanen, P.; Cournapeau, D.; Wieser, E.; Taylor, J.; Berg, S.; Smith, N. J.; Kern, R.; Picus, M.; Hoyer, S.; van Kerkwijk, M. H.; Brett, M.; Haldane, A.; Fernández del Río, J.; Wiebe, M.; Peterson, P.; Gérard-Marchant, P.; Sheppard, K.; Reddy, T.; Weckesser, W.; Abbasi, H.; Gohlke, C.; Oliphant, T. E. Array programming with NumPy, *Nature*, **2020**, *585*, 357–362
- (60) Virtanen, P.; Gommers, R.; Oliphant, T. E.; Haberland, M.; Reddy, T.; Cournapeau, D.; Burovski, E.; Peterson, P.; Weckesser, W.; Bright, J.; van der Walt, S. J.; Brett, M.; Wilson, J.; Millman, K. J.; Mayorov, N.; Nelson, A. R. J.; Jones, E.; Kern, R.; Larson, E.; Carey, C. J.; Polat, I.; Feng, Y.; Moore, E. W.; VanderPlas, J.; Laxalde, D.; Perktold, J.; Cimrman, R.; Henriksen, I.; Quintero, E. A.; Harris, C. R.; Archibald, A. M.; Ribeiro, A. H.; Pedregosa, F.; van Mulbregt, P.; and SciPy 1.0 Contributors. SciPy 1.0: Fundamental Algorithms for Scientific Computing in Python. *Nat. Methods*, **2020**, *17*, 261–272.
- (61) McKinney, W. Data Structures for Statistical Computing in Python, *Proceedings of the 9th Python in Science Conference*, **2010**, 51-56.
- (62) Andrew, A. M. Another Efficient Algorithm for Convex Hulls in Two Dimensions. *Information Processing Letters*, **1979**, *9*, 216–219.
- (63) Delaunay, Boris, Sur La Sphère Vide. *Bulletin de l'Académie Des Sciences de l'URSS, Classe Des Sciences Mathématiques et Naturelles*, **1934**, *6*, 793–800.

# Chapter 3.

## Objectives.

The main objective of this thesis is two sided. First, it aims at establishing valid protocols to study metallocage supported catalysis by computational means. Second, it aims at shedding light on several processes involved in the  $[\text{Ga}_4\text{L}_6]^{12-}$  cage. In particular, three different processes have been addressed, with their respective objectives.

### 3.1. Cationic-guest encapsulation by the $[\text{Ga}_4\text{L}_6]^{12-}$ .

Guest encapsulation by the  $[\text{Ga}_4\text{L}_6]^{12-}$  has not been described computationally in explicit solvent. The objectives of this study are:

- Establishing an accurate parametrization for calculating a binding Gibbs energy of a cationic guest encapsulated by the  $[\text{Ga}_4\text{L}_6]^{12-}$ .
- Providing molecular insights into the host-guest complexes determined experimentally.
- Determining and evaluating the mechanism of the encapsulation of  $\text{NEt}_4^+$  by the  $[\text{Ga}_4\text{L}_6]^{12-}$  in aqueous solution.

### 3.2. The C-C reductive eliminations catalyzed by the $[\text{Ga}_4\text{L}_6]^{12-}$ .

The  $[\text{Ga}_4\text{L}_6]^{12-}$ -catalyzes the alkyl-alkyl reductive elimination from Au(III) and Pt(IV) complexes.  $(\text{PEt}_3)(\text{I})\text{Au}^{\text{III}}(\text{CH}_3)_2$  represents the largest rate enhancement ( $1.9 \cdot 10^7$ ) among the metal-organic cage-catalyzed reactions. The origin of this catalysis and the influence of the phosphine ligand and metal nature have not been disclosed. The objectives of this study are:

- Identifying the origin of the  $[\text{Ga}_4\text{L}_6]^{12-}$ -catalyzed alkyl-alkyl reductive elimination from  $(\text{PEt}_3)(\text{I})\text{Au}^{\text{III}}(\text{CH}_3)_2$  and from  $(\text{PMe}_3)(\text{I})\text{Au}^{\text{III}}(\text{CH}_3)_2$ .
- Identifying the origin of the  $[\text{Ga}_4\text{L}_6]^{12-}$ -catalyzed alkyl-alkyl reductive elimination from  $(\text{PMe}_3)_2(\text{I})\text{Pt}^{\text{IV}}(\text{CH}_3)_3$ .

- Comparing the origin of catalysis for Au(III) and Pt(IV) complexes.

### 3.3. The Nazarov cyclization catalyzed by the $[\text{Ga}_4\text{L}_6]^{12-}$ .

The Nazarov cyclization of 1,4-pentadien-3-ol catalyzed by the  $[\text{Ga}_4\text{L}_6]^{12-}$  has been reported. A rate acceleration greater than  $10^6$  has been observed, but the reasons for such a huge rate acceleration remains unclear. The objectives of this study are:

- Identifying the origin of the rate acceleration in the Nazarov cyclization of 1,4-pentadien-3-ol catalyzed by the  $[\text{Ga}_4\text{L}_6]^{12-}$ .
- Analyzing the fact that the rate-determining step is modified between the uncatalyzed and  $[\text{Ga}_4\text{L}_6]^{12-}$ -catalyzed Nazarov cyclizations.
- Developing a computational strategy to evaluate the protonation step in solution and within the cavity of  $[\text{Ga}_4\text{L}_6]^{12-}$ .



## Chapter 4.

### Cationic guest encapsulation by the $[\text{Ga}_4\text{L}_6]^{12-}$ .

Guest-encapsulation is a fundamental process in supramolecular chemistry including host-guest catalysis and molecular transport.<sup>1</sup> In the last few decades, numerous encapsulation processes involving supramolecular organometallic cages have been disclosed.<sup>2,3</sup> Despite the substantial differences with their organic counterparts, to date very little modelling has been performed on those systems. They are though crucial and unresolved questions regarding the mechanism of host-guest by these systems that would benefit from molecular insights (i.e. what is the relevance of the metal of the cage in the encapsulation process, what about the general shape, etc.) Thus, accurate molecular modelling is required to account for the complexities and interactions of the process. In this work, we report our investigations on molecular modeling of cationic guest-encapsulation by the  $[\text{Ga}_4\text{L}_6]^{12-}$  in explicit aqueous solution. Guest-encapsulations for cationic and neutral molecules by the  $[\text{Ga}_4\text{L}_6]^{12-}$  have been reported experimentally and numerous energetic variables are accessible from experiments.<sup>4-8</sup> Amongst them, absolute binding affinities have been measured for the cationic species and represent an excellent starting point for modeling studies. Similar data are not available for neutral guests. In this chapter, we modelled the entire cationic guest-encapsulation process in explicit aqueous environment with force field calculations (Figure 4.1).

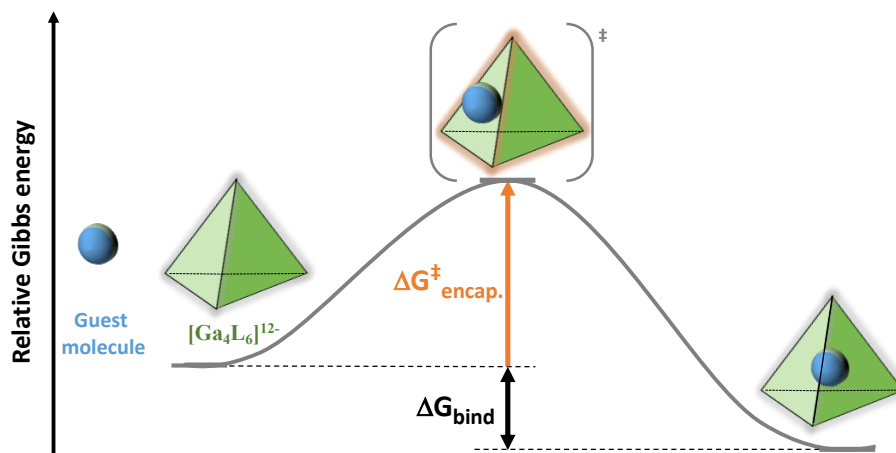


**Figure 4.1.** General representation for guest encapsulation process.

This study is three folded:

- (1) to investigate the most accurate force field parametrization procedure for calculating the absolute binding Gibbs energy ( $\Delta G_{\text{bind}}$ ) of a cationic guest molecule. We selected  $\text{NEt}_4^+$  as a case.
- (2) to analyze the difference observed experimentally between different cationic guests.
- (3) we seek the core of the process by determining the pathway of encapsulation of  $\text{NEt}_4^+$  by the  $[\text{Ga}_4\text{L}_6]^{12-}$  using the umbrella sampling method with the weighted histogram analysis method (US-WHAM).

These three items are summarized in the next subsections.

**4.1. Force field parametrization:** calculating the binding Gibbs energy of  $\text{NEt}_4^+$  in the  $[\text{Ga}_4\text{L}_6]^{12-}$ .

During the encapsulation of the cationic guest molecule by the  $[\text{Ga}_4\text{L}_6]^{12-}$  there is no chemical reaction therefore, it is an appropriate system to explore with classical force fields methods that provide with the sampling necessary to calculate accurately  $\Delta G_{\text{encapsulation}}$ . The current state-of-the-art force fields still lack a definitive parametrization approaches for most metal ions and non-standard residues.<sup>9</sup> Thus, we intensively work first on the parametrization process for the entire host and the guest molecule.  $\text{NEt}_4^+$  was selected as a guest since it presents the most favorable

encapsulation ( $-6.21 \pm 0.01$ ) compared to other species like  $\text{NMe}_4^+$ , ( $-3.42 \pm 0.001$ ) or  $\text{NPr}_4^+$ , ( $-2.75 \pm 0.03$ ) counterparts.<sup>4</sup>

The parametrization procedure starts with full QM geometry optimizations of the metallocage (host) and the  $\text{NEt}_4^+$  (guest) (Figure 4.2).

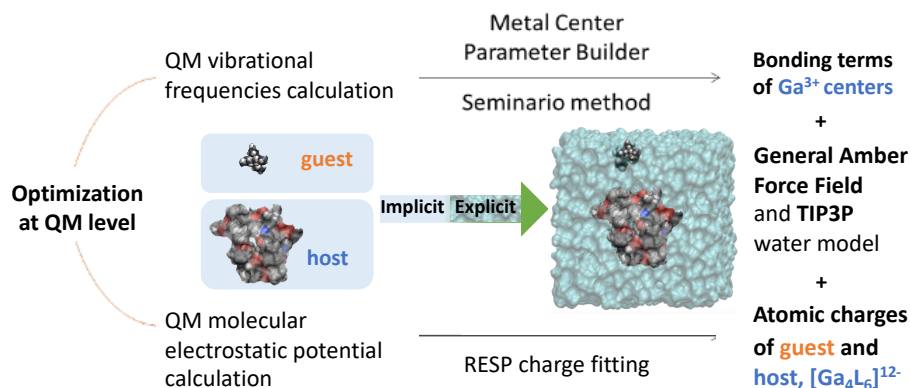


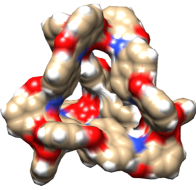
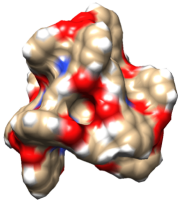
**Figure 4.2.** General scheme of the force field parametrization in this study.

For the metallocage, the python-based metal center parameter builder (MCPB.py) program<sup>10</sup> was used to derive the force constants associated with the gallium centers of the  $[\text{Ga}_4\text{L}_6]^{12-}$  from the full QM vibrational frequencies calculation. The atomic charges of the metallocage and the guest were obtained from the QM molecular electrostatic potential (MEP) calculation.<sup>11</sup> Solvation effects were accounted for using the SMD continuum solvent model in the QM calculations.<sup>12</sup>

Binding Gibbs energies were computed using the Attach-Pull-Release (APR) approach.<sup>13</sup> This approach uses the umbrella sampling technique with the thermodynamic integration method to compute the binding Gibbs energy ( $\Delta G_{\text{bind}}$ ). The umbrella sampling simulations in the APR approach are performed in two phases. The first is attaching the restraints to the guest and the second is pulling the guest out from the host. The accumulative work from each phase is computed with the thermodynamic integration approach and the work of releasing the guest to standard concentration is also computed. The standard binding Gibbs energy is calculated to be equal to the negative sum of these works. We systematically evaluated the solvation effects on the parametrization of the bonding terms for  $\text{Ga}^{3+}$  and

charges for the complete host and guest; binding Gibbs energies are obtained for each parametrization set (Table 4.1).

**Table 4.1.** Calculated binding Gibbs energies of  $\text{NEt}_4^+$  in the  $[\text{Ga}_4\text{L}_6]^{12-}$  using the APR method computed with different parametrization. All energies in kcal/mol.

	Bonding terms of $\text{Ga}^{3+}$ centers derived	Host charges calculated in	Guest charges calculated in	$\Delta G^\circ_{\text{calc.}}$	$\Delta G^\circ_{\text{exp.}}$
1		implicit water	implicit water	$-9.8 \pm 0.8$	<b>-6.2</b>
2		implicit water	vacuum	$-11.2 \pm 0.8$	
3		vacuum	vacuum	$-2.1 \pm 0.5$	
4		vacuum	implicit water	$-4.0 \pm 0.6$	
5		<b>implicit water</b>	<b>implicit water</b>	<b><math>-6.3 \pm 0.6</math></b>	
6		implicit water	vacuum	$-5.7 \pm 0.6$	
7		vacuum	vacuum	$-2.5 \pm 0.6$	
8		vacuum	implicit water	$-2.5 \pm 0.5$	
9		implicit water	AMBER-bcc	$-8.2 \pm 0.6$	

The validity of the parametrization processes was done by comparing calculations obtained with the APR approach with the experimental data. This systematic analysis shows that the parameters (the bonding terms of the gallium centers and atomic charges of the host and the guest) derived from full QM calculations with implicit solvent are the most compatible with the experimental value. In the second-best combination, the host parameters (the bonding terms of the gallium centers and atomic charges of the host only) are also derived from implicit solvent calculations. The reason behind this may be related to the fact that the optimized geometry of the metallocage in aqueous solution is significantly different from the one in vacuum.

More importantly, a common way of deriving atomic charges is calculating the charges in gas phase using the geometry optimized in implicit solvent. The result ( $+2.7 \pm 0.5$ ) obtained in this way was not comparable to the

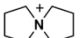
experimental value ( $-6.21 \pm 0.01$ ). Such large difference between the different parametrization protocols was not expected at the beginning of the work although, from the physico-chemical perspective, the highly anionic metallogage can be at the core of the issue.

Overall, these results bring out the importance of the solvation effects that should be taken into account in a consistent way for the parametrization in order to model thermodynamics of this host-guest system in explicit aqueous solution.

## 4.2. Assessing the force field parametrization.

Here, we examined the parametrization protocol obtained in the previous section for reproducing other experimental values available. All calculated binding Gibbs energies and their experimental values are gathered in Table 4.2.

**Table 4.2.** Binding Gibbs energies of cationic guests in the  $[\text{Ga}_4\text{L}_6]^{12-}$  computed using the APR method.

Host-Guest complex	Calculated $\Delta G^{\circ}_{\text{bind}}$	Experimental <sup>4,5</sup> $\Delta G^{\circ}_{\text{bind}}$	$\Delta\Delta G$
$\text{NEt}_4^+ \subset [\text{Ga}_4\text{L}_6]^{12-}$ , <b>2</b> $\subset$ <b>1</b>	$-6.28 \pm 0.56$	$-6.21 \pm 0.01$ (-6.29)	0.07
$\text{NMe}_4^+ \subset [\text{Ga}_4\text{L}_6]^{12-}$ , <b>3</b> $\subset$ <b>1</b>	$-1.15 \pm 0.82$	$-3.42 \pm 0.001$	2.27
$\text{PEt}_4^+ \subset [\text{Ga}_4\text{L}_6]^{12-}$ , <b>4</b> $\subset$ <b>1</b>	$-8.32 \pm 0.63$	$-6.85 \pm 0.03$	1.47
 $\subset [\text{Ga}_4\text{L}_6]^{12-}$ , <b>5</b> $\subset$ <b>1</b>	$-4.36 \pm 0.60$	$-5.59 \pm 0.01$	1.23
$\text{NPr}_4^+ \subset [\text{Ga}_4\text{L}_6]^{12-}$ , <b>6</b> $\subset$ <b>1</b>	$-0.62 \pm 0.73$	$-2.75 \pm 0.03$ (-4.25)	2.13
$\text{NMe}_2\text{Pr}_2^+ \subset [\text{Ga}_4\text{L}_6]^{12-}$ , <b>7</b> $\subset$ <b>1</b>	$-5.86 \pm 0.97$	$-4.80 \pm 0.03$	1.06

The general trend of the binding Gibbs energy of the cationic guests determined experimentally is reproduced well ( $4 > 2 > 5 > 7 > 3 > 6$  by experiments and  $4 > 2 > 7 > 5 > 3 > 6$  by calculations) despite only two guests, **5** and **7**, reverse their relative order in the calculation. The difference between the binding Gibbs energy of **5** and **7** measured experimentally is 0.79 kcal/mol while it is computationally 1.50 kcal/mol. The absolute errors of the calculated binding Gibbs energies of **5** and **7** are 1.23 and 1.06

kcal/mol, respectively. This shows that in spite of the relative order is altered, the absolute value of the binding Gibbs energy is determined with a high degree of accuracy.

Two largest absolute deviations, 2.27 and 2.13 kcal/mol, are calculated for the smallest ( $\text{NMe}_4^+$ ) and largest ( $\text{NPr}_4^+$ ) guests, respectively. This indicates that the calculation is more sensitive to guest-size than the experiment. In fact, both the computed and experimental binding Gibbs energies are more affected by the size of the guest molecule than its shape and central atom. It shows that the guest-size is a major factor in these host-guest bindings.

To further examine the influence of the guest-size, we calculated a molecular volume of the guest and internal cavity volume of the host for each of the host-guest complexes. The guest volume ranges from  $79 \text{ \AA}^3$  to  $204 \text{ \AA}^3$  (142, 79, 155, 122, 204 and  $141 \text{ \AA}^3$  for **2**, **3**, **4**, **5**, **6**, and **7** respectively); the volume of the cavity varies from  $279 \text{ \AA}^3$  to  $456 \text{ \AA}^3$  (324, 279, 306, 297, 456 and  $325 \text{ \AA}^3$  calculated for the most populated MD structures of **2c1**, **3c1**, **4c1**, **5c1**, **6c1** and **7c1** respectively). Interestingly, a linear relationship ( $R^2=0.97$ ) between the calculated binding Gibbs energy ( $\Delta G_{\text{bind}}$ ) and molecular volume of the guest ( $V_{\text{guest}}$ ) is found; the largest guest, **6**, is excluded.

$$\Delta G_{\text{bind}} = -0.09 V_{\text{guest}} + 6.08 \quad (\text{Eq 4.1})$$

This means that the larger the guest, the better the binding. It is obvious that there will be an upper limit of the guest-size ( $V_{\text{guest}}$ ) for this linear relationship owing to the size of the host cavity. However, it requires more experimental and theoretical investigations to pinpoint precisely such a limit, it is predicted to be between 156 and  $204 \text{ \AA}^3$  ( $204 \text{ \AA}^3$  is an outlier) based on these results.

In general, the absolute differences of up to 2.27 kcal/mol between experimental and calculated binding Gibbs energies of different cationic guests indicate that the parametrization procedure is at the level of accuracy to be reachable with classical force fields.

On the other hand, one might consider full QM results of at least one of the host-guest complexes for comparison. It is worth noting that full QM calculations without explicit solvent molecules overestimate the

experimental value by more than 10 kcal/mol for the binding of  $\text{NEt}_4^+$  in the  $[\text{Ga}_4\text{L}_6]^{12-}$ . It indicates that calculating the absolute binding Gibbs energy of these host-guest complexes at full QM level requires the inclusion of explicit solvent molecules, giving rise to configurational issues along with enormous computational time and resources. On other side, this method provides excellent binding Gibbs energies compared to experiment being therefore valid for such purpose.

### 4.3. Modeling the process of the encapsulation of $\text{NEt}_4^+$ by $[\text{Ga}_4\text{L}_6]^{12-}$ .

In this section, the entire encapsulation of the  $\text{NEt}_4^+$  by the  $[\text{Ga}_4\text{L}_6]^{12-}$  is modelled in explicit water solvent. The energetics of the process was obtained as the potential of mean force (PMF) along the center-of-mass (COM) distance between the  $\text{NEt}_4^+$  and  $[\text{Ga}_4\text{L}_6]^{12-}$  (Figure 4.3).

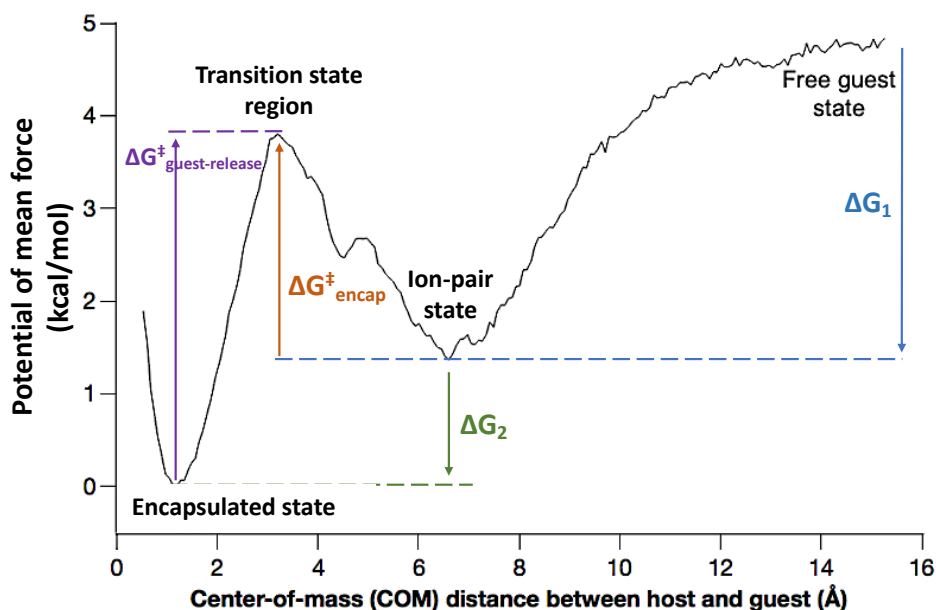


**Figure 4.3.** Potential of mean force (PMF) in explicit aqueous solution along the chosen coordinate, the distance between the center of masses of the guest,  $\text{NEt}_4^+$  and host,  $[\text{Ga}_4\text{L}_6]^{12-}$ .

The entire process was found to consist in two steps ( $\Delta G_1$  and  $\Delta G_2$  in Figure 4.3). The first step is a formation of an ion-pair complex by the

association of the  $\text{NEt}_4^+$  with the outer surface of the  $[\text{Ga}_4\text{L}_6]^{12-}$  from a “free guest state” in which they both are solvated separately. The following one involves the action of enclosing the  $\text{NEt}_4^+$  by the  $[\text{Ga}_4\text{L}_6]^{12-}$ . It is illustrated by the selected most populated structures in Figure 4.4.

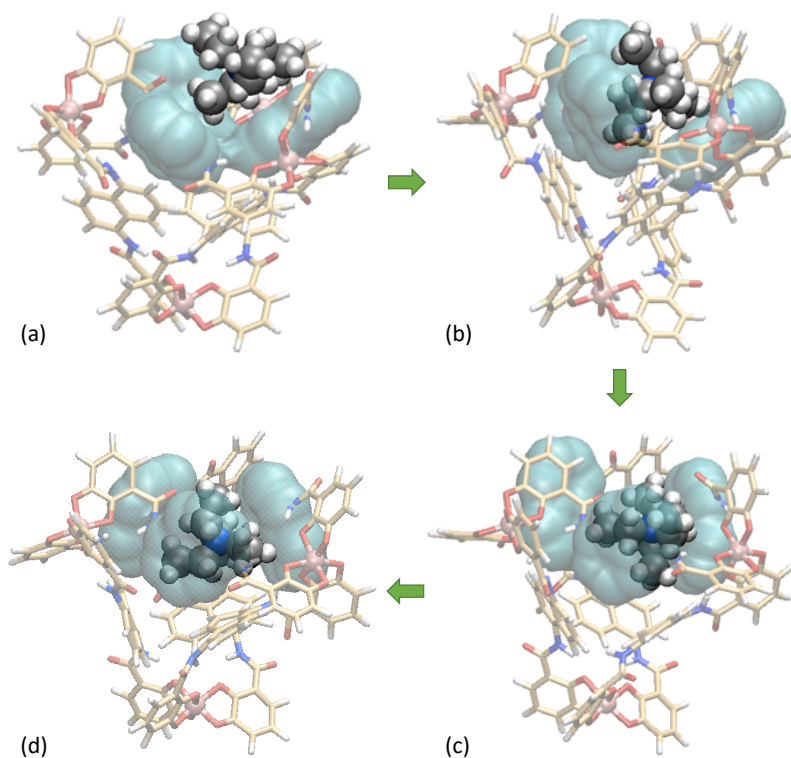


**Figure 4.4.** Most populated molecular structures for the guest-entering. (a) Ion-pair state, (b) pre-transition state, (c) transition state region, and (d) post-transition state.

The PMF shows that the ion-pair complex,  $(\text{NEt}_4^+ \cdot [\text{Ga}_4\text{L}_6]^{12-})^{11-}$ , forms at a distance of center of masses of ca. 6.6 Å between the  $\text{NEt}_4^+$  and the  $[\text{Ga}_4\text{L}_6]^{12-}$ . The geometry of the complex is shown by its most populated structure in Figure 4.4a. In this state, the  $\text{NEt}_4^+$  interacts with three naphthalene rings of one of the four faces of the tetrahedron metallocage, forming a “cone-like” structure (cyan in Figure 4.4a). The evolution of this structure through the enclosing action is depicted in Figure 4.4a-d, with some relevant data gathered in Table 4.3.



**Table 4.3.** COM distances between the  $\text{NEt}_4^+$  and the  $[\text{Ga}_4\text{L}_6]^{12-}$  and cavity volumes of the  $[\text{Ga}_4\text{L}_6]^{12-}$  at the selected points for the guest-enclosing action.

	<b>Ion-pair</b>	<b>Pre-TS</b>	<b>TS</b>	<b>Post-TS</b>
Selected structure*	“cone-like”	“blunted cone-like”	“cylinder-like”	inverse of the “blunted cone-like”
COM distance	6.6 Å	3.9 Å	3.3 Å	3.1 Å
$V_{\text{cavity}}$		233 Å <sup>3</sup>	350 Å <sup>3</sup>	238 Å <sup>3</sup>

\* three naphthalene rings of the metallocage interact with the  $\text{NEt}_4^+$  in the ion-pair state, shown in cyan in Figure 4.4.

The ion-pair state is calculated to be more stable than the free guest state by 3.4 kcal/mol which is in excellent agreement with the experimental value of 3.5 kcal/mol ( $\Delta G_1$  in Figure 4.3). The intermolecular attractive interactions can be described as  $\text{C-H}\cdots\pi$  interactions between the C-H bonds of the  $\text{NEt}_4^+$  and the naphthalene rings of the  $[\text{Ga}_4\text{L}_6]^{12-}$  and  $\text{C-H}\cdots\text{O}(\text{peptide})$  interactions between the C-H bonds of the  $\text{NEt}_4^+$  and the peptide oxygen of the organic linkers of the  $[\text{Ga}_4\text{L}_6]^{12-}$ .

From the computed PMF, the transition state and the encapsulated state are found to be at the COM distance of ca. 3.3 Å and ca. 1.1 Å between the  $\text{NEt}_4^+$  and the  $[\text{Ga}_4\text{L}_6]^{12-}$ , respectively. The encapsulated state is found to be more stable than the ion-pair state by 1.4 kcal/mol which is also in agreement with the experimental value of 2.7 kcal/mol ( $\Delta G_2$  in Figure 4.3).

In conclusion, this work provides a parametrization procedure for modeling the energetics and mechanism of encapsulation of a cationic guest by the  $[\text{Ga}_4\text{L}_6]^{12-}$  and highlights the importance of the solvation effect in the derivation of the non-standard force field parameters. It also explains the difference in binding affinity determined experimentally between different cationic guests by revealing a relationship between the binding Gibbs energy and molecular volume of the guest with an upper limit. Overall, the work shows that classical molecular dynamics with properly

derived non-standard parameters is sufficient for investigations of encapsulation by supramolecular organometallic cages on account of all computed results in this study are in good agreement with the corresponding experimental data.

## References:

- (1) Lehn, J. M. *Supramolecular Chemistry: Receptors, Catalysts, and Carriers*. **1985**, *227*, 849–856.
- (2) Amouri, H.; Desmarests, C.; Moussa, J. Confined Nanospaces in Metallocages: Guest Molecules, Weakly Encapsulated Anions, and Catalyst Sequestration. *Chem. Rev.* **2012**, *112*, 2015–2041.
- (3) Ryan, H. P.; Haynes, C. J. E.; Smith, A.; Grommet, A. B.; Nitschke, J. R. Guest Encapsulation within Surface-Adsorbed Self-Assembled Cages. *Adv. Mater.* **2021**, *33*, 2004192.
- (4) Pluth, M. D.; Raymond, K. N. Reversible Guest Exchange Mechanisms in Supramolecular Host-Guest Assemblies. *Chem. Soc. Rev.* **2007**, *36*, 161–171.
- (5) Sgarlata, C.; Raymond, K. N. Untangling the Diverse Interior and Multiple Exterior Guest Interactions of a Supramolecular Host by the Simultaneous Analysis of Complementary Observables. *Anal. Chem.* **2016**, *88*, 6923–6929.
- (6) Davis, A. V.; Raymond, K. N. The Big Squeeze: Guest Exchange in an  $M_4L_6$  Supramolecular Host. *J. Am. Chem. Soc.* **2005**, *127*, 7912–7919.
- (7) Davis, A. V.; Fiedler, D.; Seeber, G.; Zahl, A.; Van Eldik, R.; Raymond, K. N. Guest Exchange Dynamics in an  $M_4L_6$  Tetrahedral Host. *J. Am. Chem. Soc.* **2006**, *128*, 1324–1333.
- (8) Biro, S. M.; Bergman, R. G.; Raymond, K. N. The Hydrophobic Effect Drives the Recognition of Hydrocarbons by an Anionic Metal-Ligand Cluster. *J. Am. Chem. Soc.* **2007**, *129*, 12094–12095.
- (9) Monticelli, L.; Tieleman, D. P. Force Fields for Classical Molecular Dynamics. *Methods Mol. Biol. Biomol. Simulations* **2012**, *924*, 197–213.
- (10) Li, P.; Merz, K. M. MCPB.Py: A Python Based Metal Center Parameter Builder. *J. Chem. Inf. Model.* **2016**, *56*, 599–604.
- (11) Wang, J.; Wang, W.; Kollman, P. A.; Case, D. A. Automatic Atom Type and Bond Type Perception in Molecular Mechanical Calculations. *J. Mol. Graph. Model.* **2006**, *25*, 247–260.
- (12) Marenich, A. V.; Cramer, C. J.; Truhlar, D. G. Universal Solvation Model Based on Solute Electron Density and on a Continuum Model of the Solvent Defined by the Bulk Dielectric Constant and Atomic Surface Tensions. *J. Phys. Chem. B* **2009**, *113*, 6378–6396.
- (13) Yin, J.; Henriksen, N. M.; Slochower, D. R.; Gilson, M. K. The SAMPL5 Host–Guest Challenge: Computing Binding Free Energies and Enthalpies from Explicit Solvent Simulations by the Attach-Pull-Release (APR) Method. *J. Comput. Aided. Mol. Des.* **2017**, *31*, 133–145.

Publication 1

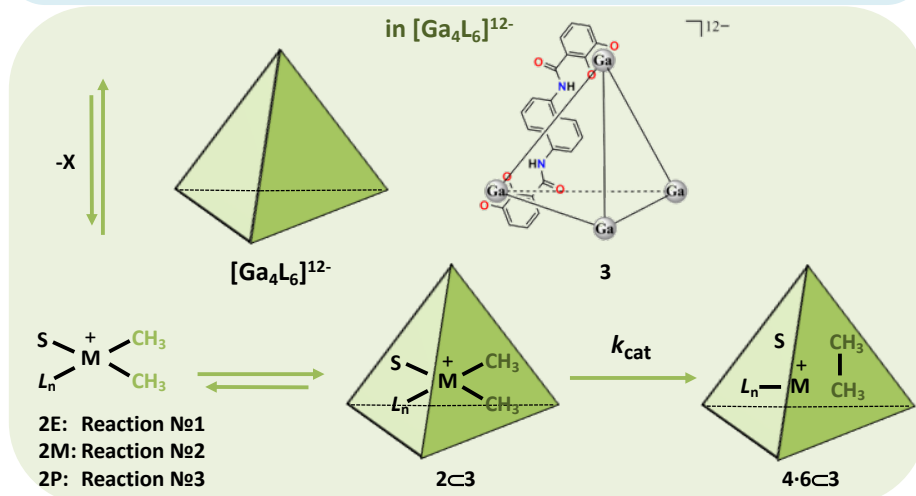
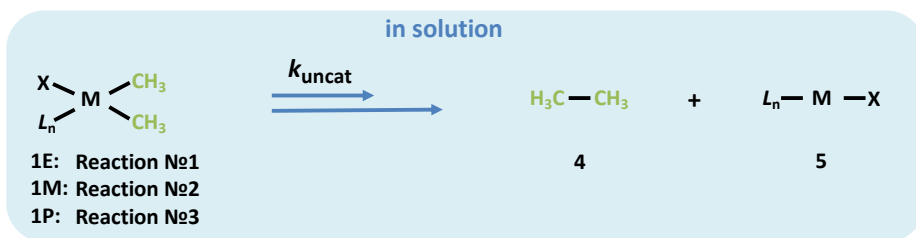
<https://doi.org/10.1021/acs.jcim.1c00348>

## Chapter 5.

### C-C reductive eliminations catalyzed by the $[\text{Ga}_4\text{L}_6]^{12-}$ .

Catalysis is crucial to many chemical and biological processes. Over the last few decades, it has featured a new sub-field stemmed from the development of supramolecular chemistry inspired by nature, so-called supramolecular catalysis.<sup>1-4</sup> In the design and synthesis of supramolecular systems, metal-organic cages come to prominence as a host environment; several are able to catalyze chemical transformations by encapsulation as a molecular reactor.<sup>5-8</sup> Indeed, a few remarkable examples of such catalysis conducted under homogeneous conditions have shown “enzyme-like” characteristics (rate accelerations  $>10^6$ ), indicating a promising direction for the artificial enzymes.<sup>9,10</sup> One of them is an alkyl-alkyl reductive elimination from a Au(III) and Pt(IV) complexes encapsulated by the  $[\text{Ga}_4\text{L}_6]^{12-}$ . The measured rate acceleration for the gold reaction was up to  $1.9 \cdot 10^7$ .<sup>9</sup> Despite these experimental findings, theoretical modelling is still required to identify the origin of the rate accelerations and provide further insights into the reaction mechanism.

In this chapter, we report the summary of our investigations on the origin of rate accelerations of alkyl-alkyl reductive eliminations from Au(III) and Pt(IV) complexes in the  $[\text{Ga}_4\text{L}_6]^{12-}$ . Three alkyl-alkyl reductive eliminations will be discussed both in solution and in the  $[\text{Ga}_4\text{L}_6]^{12-}$  (Scheme 5.1).



Reaction	Rate acceleration		Transition metal complex
№ 1	$k_{\text{cat}}/k_{\text{uncat}} = 1.9 \cdot 10^7$	1E	M = Au, X = I, S = CH <sub>3</sub> OH, L <sub>n=1</sub> = PEt <sub>3</sub>
№ 2	$k_{\text{cat}}/k_{\text{uncat}} = 5 \cdot 10^5$	1M	M = Au, X = I, S = CH <sub>3</sub> OH, L <sub>n=1</sub> = PMe <sub>3</sub>
№ 3	$k_{\text{cat}}/k_{\text{uncat}} = 2.6 \cdot 10^4$	1P	M = Pt, X = I, S = CH <sub>3</sub> OH, L <sub>n=3</sub> = (PMe <sub>3</sub> ) <sub>2</sub> ; CH <sub>3</sub>

**Scheme 5.1.** General schematic representation for three alkyl-alkyl reductive eliminations studied in this chapter.

In addition to the origin of the rate acceleration in the  $[\text{Ga}_4\text{L}_6]^{12-}$ , the influence of the phosphine ligand size (PEt<sub>3</sub> vs PMe<sub>3</sub>) and the influence of the metal nature (Au(III) vs Pt(IV)) for these processes will be discussed by comparing reactions 1 and 2, and 2 and 3, respectively (Scheme 5.1). Each reductive elimination in solution as well as in the metallocage is modelled by full QM calculations guided by classical MD simulations.

### 5.1. Origin of the rate acceleration in C-C reductive elimination from *cis*-iododimethyl(triethylphosphine)gold(III) complex encapsulated in the $[\text{Ga}_4\text{L}_6]^{12-}$ .

### 5.1.1. Reaction in solution.

We start with modeling the reductive elimination from *cis*-iododimethyl(triethylphosphine)gold(III) complex,  $(\text{PEt}_3)\text{Au}(\text{I})(\text{CH}_3)_2$ , **1E**, in solution (Scheme 5.1). An initial halide dissociation of **1E** in methanol solvent was experimentally proposed, forming a cationic gold intermediate.<sup>9,11</sup> In order to model this intermediate, a relative Gibbs energy of two species, one with a vacant site,  $[(\text{PEt}_3)\text{Au}(\text{CH}_3)_2]^+$ , **1E-I** (“T-shaped”), and the other with explicit solvent coordinated,  $[(\text{PEt}_3)\text{Au}(\text{MeOH})(\text{CH}_3)_2]^+$ , **2E** (square planar), were calculated in methanol continuum solvent environment. The calculations show that the latter species is 10 kcal/mol more stable than the former and it is only 0.8 kcal/mol higher in Gibbs energy than the **1E**. This indicates that **2E** is the cationic intermediate, readily accessible in solution (Figure 5.1).

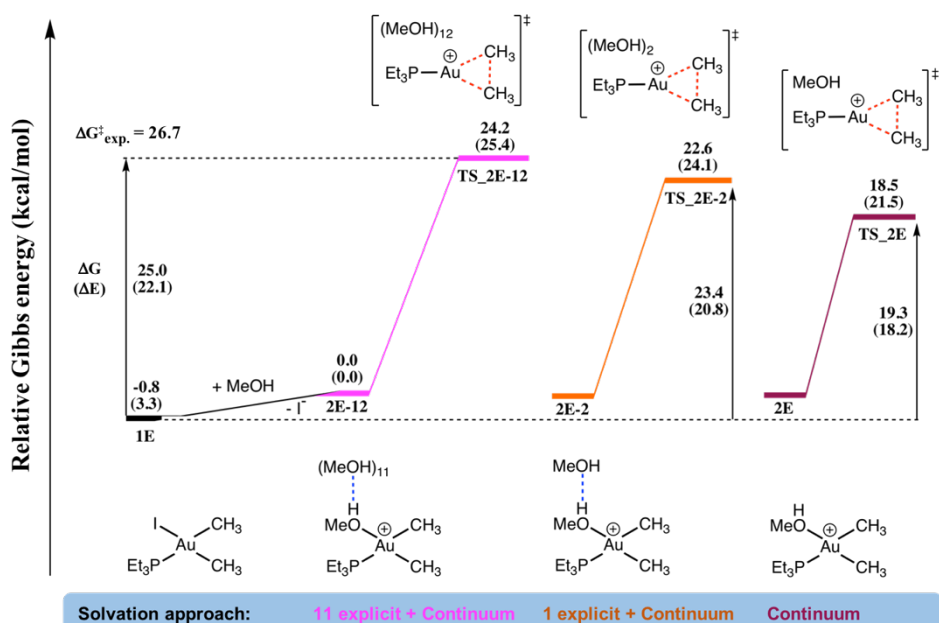


**Figure 5.1.** Calculated Gibbs energy barriers (potential energy barriers in parenthesis) for the reductive elimination from **2E** with 0, 1, and 11 additional explicit methanol solvent molecules. All calculations performed at B3LYP-D3 level with the SMD continuum solvent method. All energies in kcal/mol.

From **2E**, the alkyl-alkyl reductive elimination is calculated to have Gibbs energy barriers of 18.5 kcal/mol with continuum solvent model. In addition

to the continuum solvent, when one methanol solvent molecule is included explicitly, it is calculated to be 22.6 kcal/mol, and when considering an explicit solvation sphere of 5.5 Å around the gold complex which consists of eleven additional methanol solvent molecules, it increases to 24.2 kcal/mol. For the latter, the overall Gibbs energy barrier is thus 25.0 kcal/mol from **1E**, which is in good agreement with the experimental value of 26.7 kcal/mol (Figure 5.1). These results indicate that cluster solvation approach (mixed explicit-continuum solvent) is necessary to model this reaction in solution.

### 5.1.2. Reaction in the metallocage.

In order to study the reaction in the metallocage, we started performing classical molecular dynamic (MD) simulations for the experimental system to obtain an initial view of the system encapsulated by the metallocage.

The results reported in the fourth chapter point out that proper force field parametrization for molecular dynamic simulations should consider the influence of implicit solvent on this highly anionic metallocage. Therefore, the metallocage was firstly optimized with implicit methanol solvent at full QM level, and then using this geometry the atomic charges of the metallocage and the bonding terms of the Ga centers of the metallocage were derived with the parametrization procedure proposed in the fourth chapter.

Classical MD simulations were performed with a periodic simulation box under experimental conditions (temperature, pressure, and concentration). The first simulation contains all experimental species explicitly: **1E-I** (the “T-shaped” complex) and iodide ion, both encapsulated in the metallocage,  $(\mathbf{1E-I} + \mathbf{I}) \subset [\text{Ga}_4\text{L}_6]^{12-}$ , 12  $\text{K}^+$  counter ions to neutralize the system, and more than 3800 explicit methanol solvent molecules. The simulation box with an edge of  $\sim 68\text{\AA}$  accounts for the experimental concentration of 5mM  $[\text{Ga}_4\text{L}_6]^{12-}$  in methanol. During the simulation, the iodide ion left the cavity of the metallocage in the first 2 ns and never re-entered; around 7  $\text{K}^+$  counter ions are located within a distance lower than 11 Å from the center of mass of the metallocage most of the time. Based on these results, the overall charge of the metallocage surrounded by  $\text{K}^+$  counter ions is



approximately -4. Similar behavior was measured on the experimental system in which a cationic guest,  $\text{NEt}_4^+$ , was encapsulated in the metallocage.<sup>12,13</sup>

Importantly, the simulation shows that a methanol solvent molecule can be encapsulated by the metallocage along with the **1E-I**. Thus, we also performed two other classical MD simulations, one with **1E-I** encapsulated in the metallocage ( $\mathbf{1E-I} \subset [\text{Ga}_4\text{L}_6]^{12-}$ ) and the other with **2E** encapsulated in the metallocage ( $\mathbf{2E} \subset [\text{Ga}_4\text{L}_6]^{12-}$ ), to discern the number of solvent methanol molecules in the metallocage (Figure 5.2).

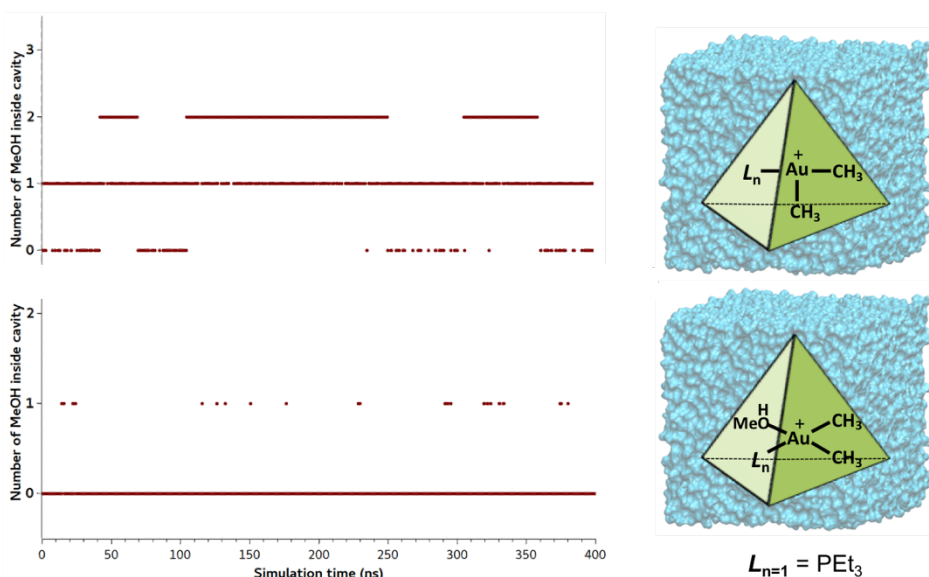


**Figure 5.2.** Number of solvent molecules in the metallocage along with **1E-I** (top) and **2E** (bottom) during 400 ns classical molecular dynamic simulations in explicit methanol solvent.

The simulations show that up to two methanol solvent molecules can be encapsulated in the metallocage. A ratio of one and two methanol molecules encapsulated in the metallocage was 97.75 : 2.25 for the simulation with  $\mathbf{2E} \subset [\text{Ga}_4\text{L}_6]^{12-}$  (bottom in Figure 5.2). This indicates that  $\mathbf{2E} \subset \mathbf{3}$  is the most suitable model system. With these results, we proceed to study the reductive elimination in the metallocage at full QM level (Figure 5.3).

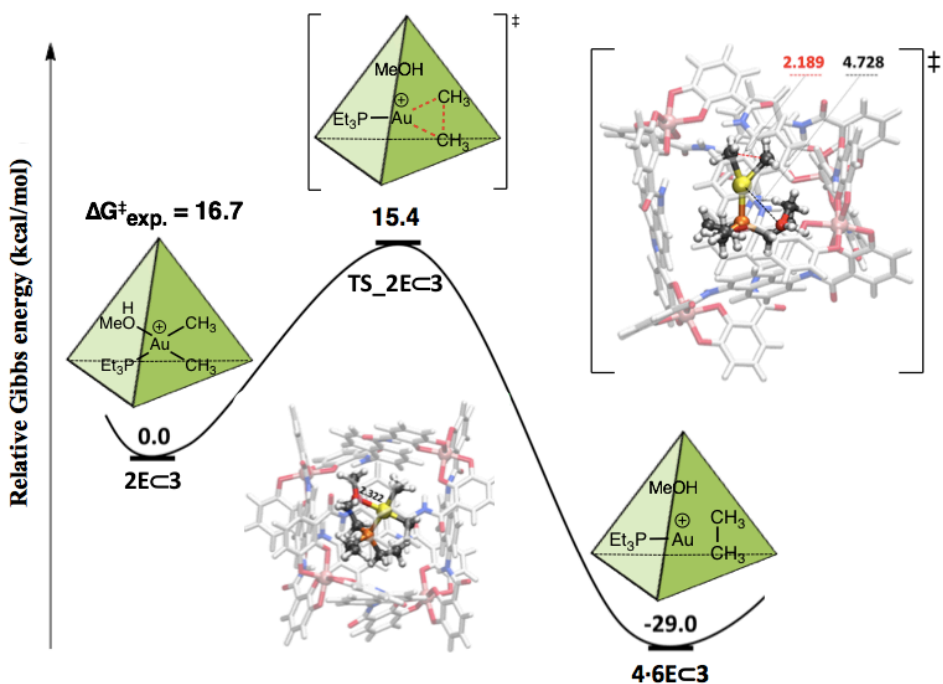


**Figure 5.3.** Gibbs energy profile of the reductive elimination in the metallocage.

The transition state of the reductive elimination in the metallocage, **TS\_2E $\subset$ 3**, is calculated to be 15.4 kcal/mol higher in Gibbs energy than the encapsulated reactant state, **2E $\subset$ 3**. This is in good agreement with the experimental value of 16.7 kcal/mol. For the other two systems with none and with two methanol solvent molecules in the metallocage, the Gibbs energy barriers are calculated to be 10.0 kcal/mol and 19.7 kcal/mol, respectively. These results indicate that explicit consideration of solvent methanol molecules in the metallocage significantly affects the calculated Gibbs energy barrier of this reaction. Moreover, model systems including seven and eleven potassium counter ions, **2E $\subset$ 3K7** and **2E $\subset$ 3K11**, are considered to evaluate the effect of the potassium counter ions surrounding the metallocage on the Gibbs energy barrier of the reductive elimination. Interestingly, for these two model systems, the Gibbs energy barriers of the reductive elimination are very similar with values of 15.4 kcal/mol and 15.1 kcal/mol, respectively (Table 5.1).

**Table 5.1.** Calculated Gibbs energy barriers for the system **2E<sub>c</sub>3** including a different number of K<sup>+</sup> counterions.

Transition states		Number of K <sup>+</sup>	Total charge	$\Delta G^\ddagger_{\text{calc}}$	$\Delta G^\ddagger_{\text{exp}}$
Name	C–C distance (Å)				
TS_2E <sub>c</sub> 3	2.19	0	– 11	15.4	
TS_2E <sub>c</sub> 3K7	2.16	7	– 4	15.4	16.7
TS_2E <sub>c</sub> 3K11	2.16	11	0	15.1	

These results suggest that the explicit solvation inside the metallocage is important whereas explicit counter ions outside the metallocage is not relevant for calculating Gibbs energy barrier of this reaction.

### 5.1.3. Origin of the catalysis.

During the encapsulation process a significant change in the first solvation shell of the gold complex takes place. This change in microsolvation can affect the Gibbs energy barrier of the process. Performing the reductive elimination inside the cage can also modify the barrier. The reductive elimination in the metallocage can be divided into two formal processes, microsolvation and encapsulation (Figure 5.4).

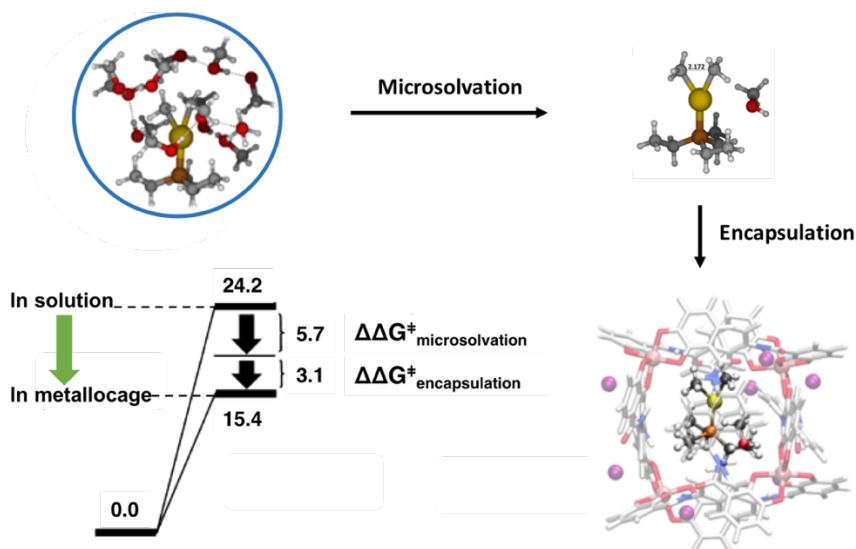


**Figure 5.4.** Reduction of the Gibbs energy barrier in the metallocage compared to in solution.

The microsolvation effect, observed by removing explicit solvent methanol molecules around the gold complex upon the encapsulation, decreases the Gibbs energy barrier by 5.7 kcal/mol (from 24.2 kcal/mol in **TS\_2E-12** to 18.5 kcal/mol in **TS\_2E**, in Figure 5.1). The encapsulation effect diminishes the Gibbs energy barrier by 3.1 kcal/mol (from 18.5 kcal/mol in **TS\_2E** to 15.4 kcal/mol in **TS\_2E $\subset$ 3**). The overall reduction of the Gibbs energy barrier in the metallocage compared to solution is 8.8 kcal/mol.

To further quantify possible contribution terms to the overall reduction of the Gibbs energy barrier, a decomposition analysis on the Gibbs energy barrier was performed; we followed a similar scheme than that employed by Himo et al. in their work with molecular capsules.<sup>14</sup> This type of analysis was very useful to distinguish strain (geometric distortion by encapsulation) and interaction terms (interaction between host and guest) from thermal contributions.

The analyses of the two formal processes, microsolvation and encapsulation are summarized in Table 5.2.

**Table 5.2.** Decomposition of Gibbs energy barriers in strain, interaction and thermal contributions for two formal processes, microsolvation and encapsulation.

	Strain $\Delta\delta E^{\ddagger}_{\text{strain}}$	Interaction $\Delta\delta E^{\ddagger}_{\text{inter}}$	Thermal $\Delta\delta Th^{\ddagger}$	$\Delta\Delta G^{\ddagger}$
<b>Microsolvation</b>	-2.2	-1.7	-1.8	-5.7
<b>Encapsulation</b>	1.2	-9.0	4.7	-3.1
<b>Total</b>	-1.0	-10.7	2.9	-8.8

Overall, these results show that the interaction term is large, whereas the strain term is moderate for lowering the energy barrier. Thermal contributions ( $\Delta\delta Th^{\ddagger}$ ) do not favor this reaction in the metallocage.

## 5.2. Origin of the rate acceleration in C-C reductive elimination from *cis*-iododimethyl(trimethylphosphine)gold(III) complex encapsulated in the [Ga<sub>4</sub>L<sub>6</sub>]<sup>12-</sup>.

In this subsection, the alkyl-alkyl reductive eliminations from a *cis*-iododimethyl(trimethylphosphine)gold(III) complex, **1M**,  $(\text{Me}_3\text{P})\text{Au}(\text{I})(\text{CH}_3)_2$  in solution and in the  $[\text{Ga}_4\text{L}_6]^{12-}$  metallocage are investigated; then the influence of the phosphine ligand size ( $\text{PEt}_3$  vs  $\text{PMe}_3$ ) on the Gibbs energy barrier of the reductive eliminations in solution and in the  $[\text{Ga}_4\text{L}_6]^{12-}$  is discussed.

### 5.2.1. Reaction in solution.

In methanol solution, an initial halide dissociation of **1M** was also proposed experimentally, forming a cationic gold intermediate.<sup>9,11</sup> Formation of this intermediate from a starting neutral gold complex, **1M**, is calculated to be 1.8 kcal/mol higher in Gibbs energy. The Gibbs energy barrier for the reductive elimination from the cationic gold intermediate, **2M-12**, is 24.4 kcal/mol. The overall Gibbs energy barrier is thus 26.2 kcal/mol from **1M** which is in excellent agreement with the experimental value of 27.2 kcal/mol (Figure 5.5).<sup>9</sup>

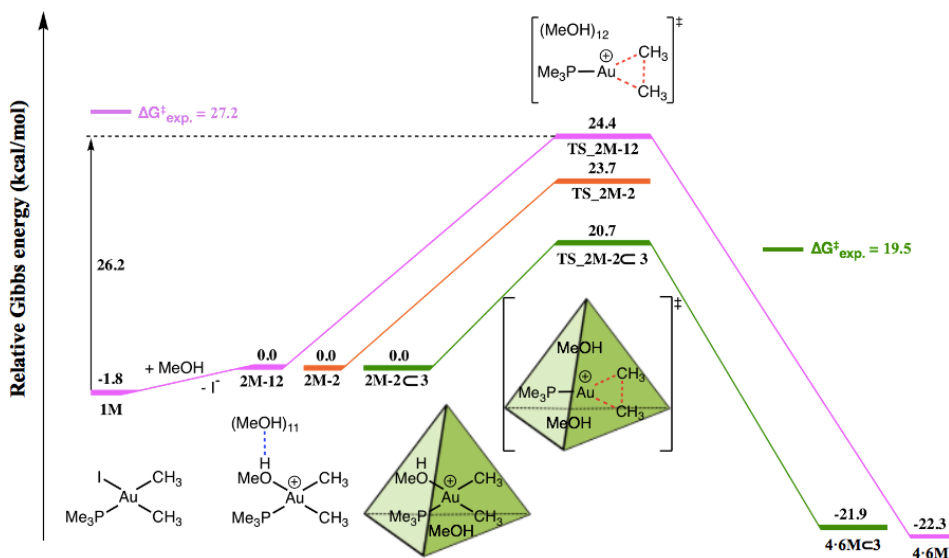


**Figure 5.5.** Gibbs energy profiles for the reductive elimination in solution and in metallocage (in kcal/mol).

### 5.2.2. Reaction in the metallocage.

Two classical MD simulations, one with **1M-I** (gold complex without iodide ligand) encapsulated in the metallocage (**1M-I**  $\subset$   $[\text{Ga}_4\text{L}_6]^{12-}$ ) and the other with **2M** encapsulated in the metallocage (**2M**  $\subset$   $[\text{Ga}_4\text{L}_6]^{12-}$ ) were performed to define the number of solvent methanol molecules in the metallocage. Both simulations show that there are two methanol molecules in the metallocage most of the time.

Thus, a model system includes two solvent methanol molecules in the metallocage, **2M-2C3**, was considered for full QM calculations. The transition state of the reductive elimination in the metallocage, **TS\_2M-2C3**, is calculated to be 20.7 kcal/mol higher in Gibbs energy than the encapsulated reactant state, **2M-2C3**. It is in good agreement with the experimental value of 19.5 kcal/mol (Figure 5.5).<sup>9,11</sup>

### 5.2.3. Origin of the catalysis and the influence of phosphine ligand (**PEt<sub>3</sub>** vs **PMe<sub>3</sub>**) on the rate acceleration.

By describing the entire environmental change from solution into the metallocage by two formal processes, microsolvation and encapsulation, the overall reductions of the Gibbs energy barriers inside the metallocage are summarized for two reductive eliminations from  $[(\text{PEt}_3)\text{Au}(\text{MeOH})(\text{CH}_3)_2]^+$  and from  $[(\text{PMe}_3)\text{Au}(\text{MeOH})(\text{CH}_3)_2]^+$  in Figure 5.6. The latter includes an additional solvent methanol molecule inside the metallocage due to the smaller size of the phosphine ligand of the cationic gold complex, as was suggested by classical molecular dynamic simulations. This difference has a large influence on the microsolvation formal process: 5.7 kcal/mol for the **PEt<sub>3</sub>** ligand and 0.7 kcal/mol for the **PMe<sub>3</sub>** ligand.

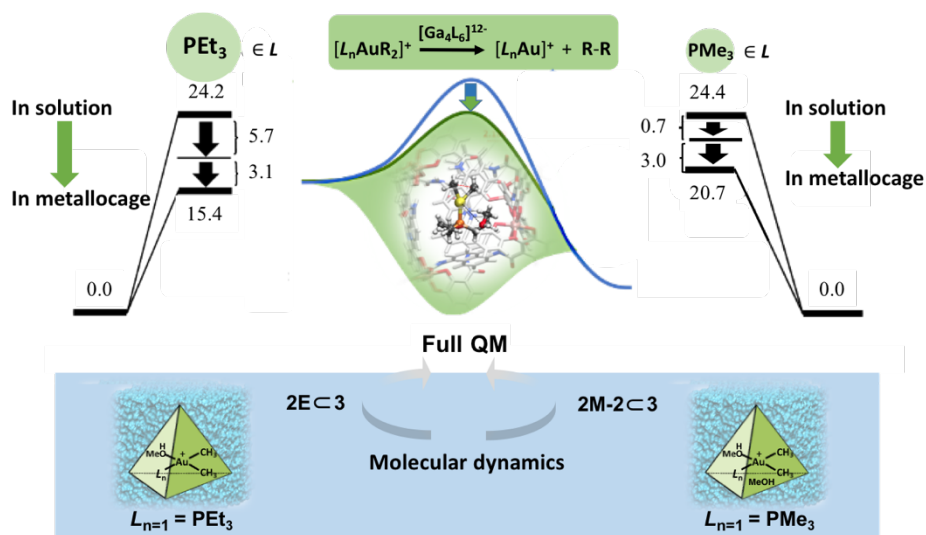


**Figure 5.6.** Overview of the Gibbs energy barrier reduction over encapsulation for both Au(III) complexes bearing  $\text{PEt}_3$  and  $\text{PMe}_3$ , respectively. Modelled at full QM level guided by classical molecular dynamics.

The encapsulation effects are calculated to be similar for both complexes with values of 3.1 kcal/mol and 3.0 kcal/mol, respectively. It is thus of interest to analyze how these encapsulation effects are comparable because the number of solvent molecules inside the metallocage are different, one and two, respectively. The analysis shows that the interaction term is significantly reduced from -9.0 kcal/mol to -1.9 kcal/mol upon encapsulation of another solvent methanol molecule by the metallocage. The strain term and the thermal term, however, become more favorable (Table 5.3).

**Table 5.3.** Decomposition analyses on encapsulation of the Gibbs energy barriers of reductive eliminations from gold complexes with  $\text{PEt}_3$  and  $\text{PMe}_3$  ligands. All energies in kcal/mol.

Ligand	Solvent inside	Interaction term	Strain term	Thermal term	$\Delta\Delta G^\ddagger_{\text{encapsulation}}$
$\text{PEt}_3$	1	-9.0	1.2	4.7	3.1
$\text{PMe}_3$	2	-1.9	-1.6	0.5	3.0

To summarize, the additional solvent methanol molecule encapsulated by the metallocage hampers the alkyl-alkyl reductive elimination from  $[(\text{PMe}_3)\text{Au}(\text{MeOH})(\text{CH}_3)_2]^+$ . The microsolvation inside the metallocage is found to be mostly responsible of the difference in rate acceleration of the reductive eliminations from  $[(\text{PET}_3)\text{Au}(\text{MeOH})(\text{CH}_3)_2]^+$  and from  $[(\text{PMe}_3)\text{Au}(\text{MeOH})(\text{CH}_3)_2]^+$ . For the former, the microsolvation effect is a major part of the overall reduction of the Gibbs energy barrier of the reductive elimination, whereas for the latter it is the encapsulation effect.

### 5.3. Origin of the rate acceleration in C-C reductive elimination from *trans*-iodo (bistrimethylphosphine)trimethylplatinum(IV) complex encapsulated in the $[\text{Ga}_4\text{L}_6]^{12-}$ .

In this last section, the alkyl-alkyl reductive eliminations from a *trans*-iodo (bistrimethylphosphine)trimethylplatinum(IV) complex, **1P**,  $(\text{Me}_3\text{P})_2\text{Pt}(\text{I})(\text{CH}_3)_3$  in solution and in the  $[\text{Ga}_4\text{L}_6]^{12-}$  metallocage are investigated. The influence of the nature of the transition metal (Au(III) vs Pt(IV)) on the Gibbs energy barrier of the reductive eliminations in solution and in the  $[\text{Ga}_4\text{L}_6]^{12-}$  is discussed latter.

#### 5.3.1. Reaction in solution.

The dissociation of halide from the neutral octahedral Pt(IV) complex, **1P**, forming a cationic platinum intermediate in solution, was experimentally proposed.<sup>9,11</sup> Formation of the cationic intermediate,  $[(\text{Me}_3\text{P})_2\text{Pt}(\text{MeOH})(\text{CH}_3)_3]^+$ , **2P**, is calculated to have a relative Gibbs energy of -2.6 kcal/mol compared to **1P** in methanol solution. From this intermediate, to model the reductive elimination with cluster solvation approach (mixed explicit-continuum solvent), five systems were considered: **2P**, **2P-2**, **2P-3**, **2P-4** and **2P-5** including none, two, three, four and five explicit solvent methanol molecules, respectively. The calculated Gibbs energy barriers are 23.8 kcal/mol, 26.2 kcal/mol, 24.4 kcal/mol, 24.4 kcal/mol and 24.3 kcal/mol, respectively, (Figure 5.7).



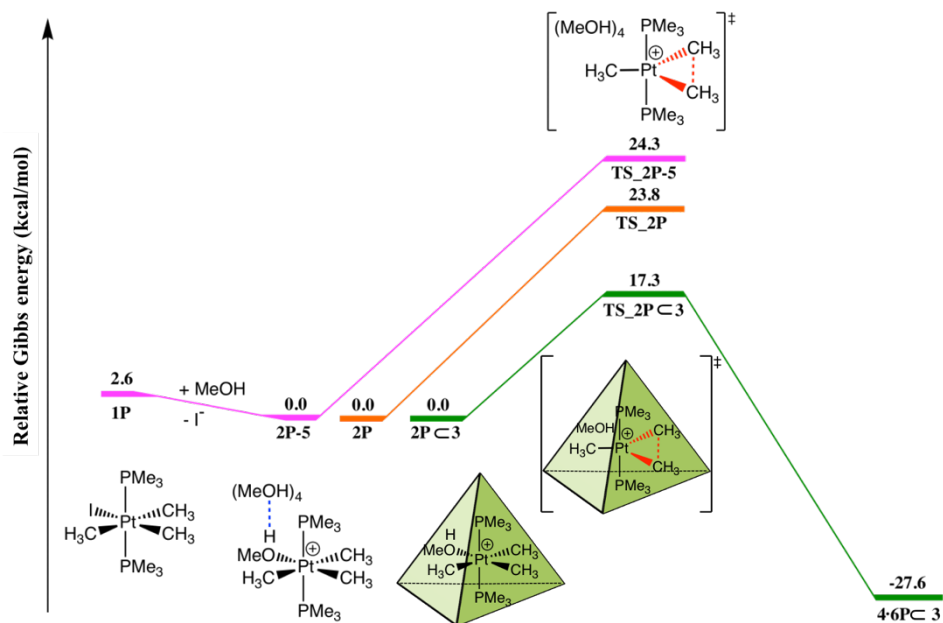


**Figure 5.7.** Gibbs energy profiles for the reductive elimination from *trans*-Pt(IV) complex in solution and in metallogage. All energies in kcal/mol.

These results suggest that those systems including more explicit solvent methanol molecules does not significantly modify the barrier. In order to compare the calculated Gibbs energy barrier with the experimental value, the reductive elimination from a *cis*-isomer of **2P-5**, *cis*-**2P-5**, was also modelled. The calculated Gibbs energy barrier is 26.9 kcal/mol, in excellent agreement with its experimental value of 27.0 kcal/mol.<sup>9,11</sup>

### 5.3.2. Reaction in the metallogage.

Classical molecular dynamic simulation with **2P** encapsulated in the metallogage ( $2P \subset [Ga_4L_6]^{12-}$ ) shows that most of the time there is no additional solvent methanol molecules in the metallogage. Therefore, **2P ⊂ 3**, system that includes only a coordinated MeOH molecules was considered as a starting point of full QM calculations. For this model system, the Gibbs energy barrier for the encapsulated reductive elimination is of 17.3 kcal/mol, which is in good agreement with the experimental value of 19.8 kcal/mol (Figure 5.7).<sup>11</sup>

### 5.3.3. Origin of the catalysis and the influence of the nature of metal (Au(III) vs Pt(IV)) on the rate acceleration.

The overall reduction of the Gibbs energy barrier of the reductive elimination in the metallocage compared to that in solution is calculated to be 7.0 kcal/mol. The microsolvation effect is 0.5 kcal/mol and the encapsulation effect is 6.5 kcal/mol. The encapsulation effect was thus analyzed by the decomposition analysis of the Gibbs energy barrier to further quantify the strain, the interaction and the thermal contributions to the overall lowering of the Gibbs energy barrier. The analysis shows that upon encapsulation the reactant is strained by 3.2 kcal/mol ( $2\mathbf{P} \rightarrow 2\mathbf{P}^*$ ) while the transition state is strained by 3.4 kcal/mol, ( $\text{TS}_{2\mathbf{P}} \rightarrow \text{TS}_{2\mathbf{P}^*}$ ). Thus, the strain contribution is calculated to be negligible ( $\Delta\Delta E_{\text{strain}}^\ddagger = 0.2$  kcal/mol). The interaction term is calculated to be -7.9 kcal/mol as the main contribution to lowering the Gibbs energy barrier in the metallocage while the thermal term is moderate in this reaction (Figure 5.8).

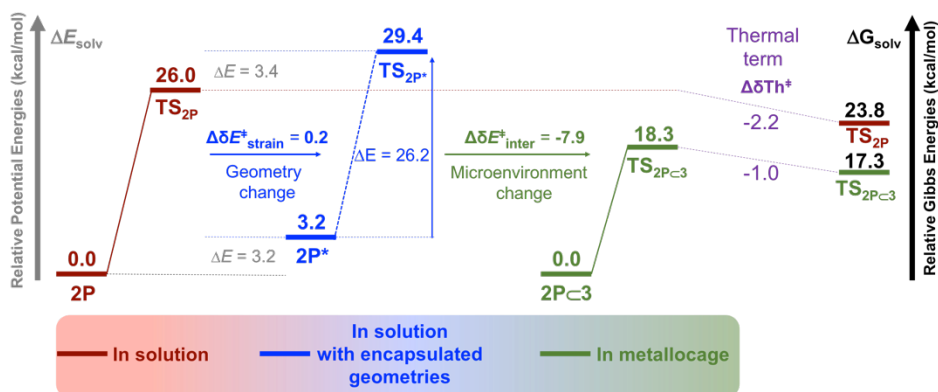


**Figure 5.8.** Decomposition analysis of Gibbs energy and potential energy barriers for the reductive elimination from *trans*-Pt(IV) complex,  $2\mathbf{P}$ , upon encapsulation by  $[\text{Ga}_4\text{L}_6]^{12-}$ . All energies in kcal/mol.

Each term is compared for both the Au(III) and Pt(IV) systems through  $2\mathbf{E}$  and  $2\mathbf{P}$  complexes, respectively (Table 5.4). The number of solvent molecules in the  $[\text{Ga}_4\text{L}_6]^{12-}$  are equal for both reactions.

**Table 5.4.** Decomposition analyses upon encapsulation of the Gibbs energy barriers of the reductive eliminations from Au(III) and Pt(IV) complexes in the  $[\text{Ga}_4\text{L}_6]^{12-}$ . All energies in kcal/mol.

Metal	Solvent inside	$\Delta\delta E^\ddagger_{\text{inter}}$	$\Delta\delta E^\ddagger_{\text{strain}}$	$\Delta\delta E^\ddagger_{\text{encap}}$	$\Delta\delta Th^\ddagger$	$\Delta\Delta G^\ddagger_{\text{encap}}$	$\Delta\Delta G^\ddagger_{\text{microsolv}}$
Au(III)	1	-9.0	1.2	-7.8	4.7	3.1	5.7
Pt(IV)	1	-7.9	0.2	-7.7	1.2	6.5	0.5

To summarize, for the Au(III) complex, the overall reduction of the Gibbs energy barrier is 8.8 kcal/mol in which the microsolvation has a major contribution (5.7 out of 8.8 kcal/mol), whereas for the Pt(IV) complex, it is 7.0 kcal/mol in which the encapsulation is essential (6.5 out of 7.0 kcal/mol).

In conclusion, these studies help to deepen our understanding of the catalysis in alkyl-alkyl reductive eliminations from high valent transition metal complexes encapsulated by the  $[\text{Ga}_4\text{L}_6]^{12-}$ . The effect of the microsolvation on the rate acceleration determined in the  $[\text{Ga}_4\text{L}_6]^{12-}$  is evaluated showing that the smaller the number of solvent molecules in the  $[\text{Ga}_4\text{L}_6]^{12-}$ , the larger the rate enhancement in the  $[\text{Ga}_4\text{L}_6]^{12-}$ . When the numbers of solvent molecules encapsulated by the  $[\text{Ga}_4\text{L}_6]^{12-}$  are equal, the electronic effects of the encapsulation (i.e. the electronic effect of the metallocage on the encapsulated system) on the rate acceleration are nearly identical for the Au(III) and Pt(IV) complexes; the entropic (thermal) contributions, however, are notably different. The decomposition of the Gibbs energy barrier, in terms of the interaction, strain and thermal parts, shows that the interaction between the metal complex and  $[\text{Ga}_4\text{L}_6]^{12-}$  is the main contribution to the overall lowering of the Gibbs energy barrier.

## References:

- (1) Raynal, M.; Ballester, P.; Vidal-Ferran, A.; Van Leeuwen, P. W. N. M. Supramolecular Catalysis. Part 1: Non-Covalent Interactions as a Tool for Building and Modifying Homogeneous Catalysts. *Chem. Soc. Rev.* **2014**, *43*, 1660–1733.
- (2) Raynal, M.; Ballester, P.; Vidal-Ferran, A.; Van Leeuwen, P. W. N. M. Supramolecular Catalysis. Part 2: Artificial Enzyme Mimics. *Chem. Soc. Rev.* **2014**, *43*, 1734–1787.
- (3) Brown, C. J.; Toste, F. D.; Bergman, R. G.; Raymond, K. N. Supramolecular Catalysis in Metal–Ligand Cluster Hosts. *Chem. Rev.* **2015**, *115*, 3012–3035.
- (4) Sciortino, G.; Norjmaa, G.; Maréchal, J. D.; Ujaque, G. “Catalysis by Metal Organic Cages: A Computational Perspective”. *Supramolecular Catalysis-New Directions and Developments*, ISBN 978-3-527-34902-9; van Leeuwen, W.N.M., Raynal, M., Eds; Wiley- VCH: W.
- (5) Cook, T. R.; Stang, P. J. Recent Developments in the Preparation and Chemistry of Metallacycles and Metallacages via Coordination. *Chem. Rev.* **2015**, *115*, 7001–7045.
- (6) Fang, Y.; Powell, J. A.; Li, E.; Wang, Q.; Perry, Z.; Kirchon, A.; Yang, X.; Xiao, Z.; Zhu, C.; Zhang, L.; et al. Catalytic Reactions within the Cavity of Coordination Cages. *Chem. Soc. Rev.* **2019**, *48*, 4707–4730.
- (7) Hong, C. M.; Bergman, R. G.; Raymond, K. N.; Toste, F. D. Self-Assembled Tetrahedral Hosts as Supramolecular Catalysts. *Acc. Chem. Res.* **2018**, *51*, 2447–2455.
- (8) Stang, P. J.; Olenyuk, B. Self-Assembly, Symmetry, and Molecular Architecture: Coordination as the Motif in the Rational Design of Supramolecular Metallacyclic Polygons and Polyhedra. *Acc. Chem. Res.* **1997**, *30*, 502–518.
- (9) Kaphan, D. M.; Levin, M. D.; Bergman, R. G.; Raymond, K. N.; Toste, F. D. A Supramolecular Microenvironment Strategy for Transition Metal Catalysis. *Science*. **2015**, *350*, 1235–1238.
- (10) Hastings, C. J.; Pluth, M. D.; Bergman, R. G.; Raymond, K. N. Enzymelike Catalysis of the Nazarov Cyclization by Supramolecular Encapsulation. *J. Am. Chem. Soc.* **2010**, *132*, 6938–6940.
- (11) Levin, M. D.; Kaphan, D. M.; Hong, C. M.; Bergman, R. G.; Raymond, K. N.; Toste, F. D. Scope and Mechanism of

- Cooperativity at the Intersection of Organometallic and Supramolecular Catalysis. *J. Am. Chem. Soc.* **2016**, *138*, 9682–9693.
- (12) Andersen, U. N.; Seeber, G.; Fiedler, D.; Raymond, K. N.; Lin, D.; Harris, D. Characterization of Self-Assembled Supramolecular [Ga<sub>4</sub>L<sub>6</sub>] Host-Guest Complexes by Electrospray Ionization Mass Spectrometry. *J. Am. Soc. Mass Spectrom.* **2006**, *17*, 292–296.
- (13) Caulder, D. L.; Powers, R. E.; Parac, T. N.; Raymond, K. N. The Self-Assembly of a Pre-designed Tetrahedral M<sub>4</sub>L<sub>6</sub> Supramolecular Cluster. *Angew. Chem., Int. Ed.* **1998**, *37*, 1840–1843.
- (14) Daver, H.; Harvey, J. N.; Rebek Jr., J.; Himo, F. Quantum Chemical Modeling of Cycloaddition Reaction in a Self-Assembled Capsule. *J. Am. Chem. Soc.* **2017**, *139*, 15494–15503.

**Publication 2**

<https://doi.org/10.1021/jacs.9b04909>

**Publication 3**

<https://doi.org/10.1002/chem.201905608>

**Publication 4**

**<https://doi.org/10.1002/chem.202102250>**



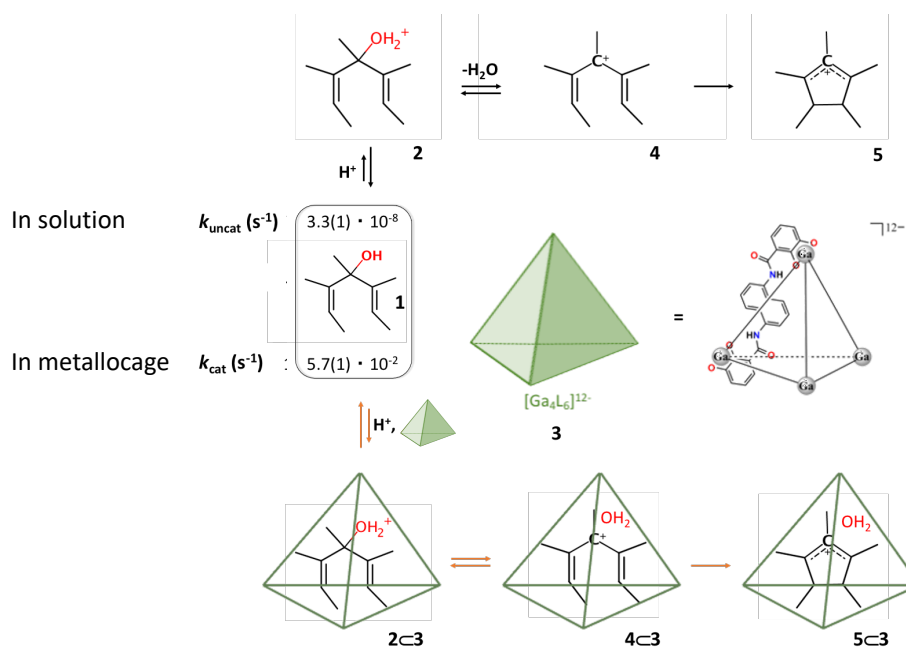
## Chapter 6.

### The Nazarov cyclization catalyzed by the $[\text{Ga}_4\text{L}_6]^{12-}$ .

In this chapter, we report our investigations on the origin of the “enzyme-like” rate acceleration observed for the Nazarov cyclization of 1,4-pentadien-3-ol catalyzed by the  $[\text{Ga}_4\text{L}_6]^{12-}$ . Based on experiments three factors (preorganization, basicity, and TS stabilization) have been considered as possible contributions to the observed rate enhancement.<sup>1</sup> Until now, neither experimental nor computational results have been reported to evaluate the contribution of each of these factors. Interestingly, experimental studies have shown that the reaction has a single rate determining step in solution, whereas it has two rate determining steps in the  $[\text{Ga}_4\text{L}_6]^{12-}$ .<sup>2</sup> Understanding how encapsulation affects all of these factors is the key to explain this observation.

The general pipeline for the computational study of this process is as follows:

- (1) simulating the reaction without the metallocage (black arrow in Scheme 6.1)
- (2) modeling the reaction within the metallocage (orange arrow in Scheme 6.1)
- (3) discussing the origin of the catalysis and the effect of encapsulation on the key steps in the reaction pathway.



**Scheme 6.1.** The general scheme of the Nazarov cyclization of 1,4-pentadien-3-ol (black arrow) in solution and (orange arrow) in the  $[\text{Ga}_4\text{L}_6]^{12-}$ .

### 6.1. Reaction in solution.

Experimental studies have determined that the reaction proceeds with the following sequential steps: (i) protonation of the substrate, **1**, 1,4-pentadien-3-ol, (ii) water loss from the substrate, (iii)  $4\pi$  electrocyclic ring closure of the pentadienyl carbocation.<sup>1,2</sup> The reaction was conducted at 45°C in the mixture of water and dimethyl sulfoxide (1:1) with  $\text{K}_3\text{PO}_4$  (pH=8.0).<sup>2</sup> Thus, the protonation step inevitably entails a hydronium ion produced by the autoionization of water. The equilibria between the substrate and its protonated form, species **1** and **2**, is related to the pKa of the protonated species. Since pKa calculations of ions in water can lead to significant deviations from experimental results, we took advantage of an estimated pKa value of -5.0 for the protonated substrate, **2**, which corresponds to a Gibbs energy of 18.9 kcal/mol from **1**, reported in the previous experimental study.<sup>2</sup>

In order to explore the conformational space and find the most stable conformers of **1** and **2**, conformational analyses were conducted. It shows

that the “U-shaped” conformation (appropriate position for cyclization) is only 0.8 kcal/mol and 0.5 kcal/mol higher in Gibbs energy than the most stable one (“L-shaped”) for **1** and **2**, respectively. Thus, there is an equilibrium between these two conformers in aqueous solution.

Water can play a vital role in reactivity and therefore employing hybrid explicit-continuum methods are highly recommended, especially in ion-involved reactions such as proton-involved.<sup>3–8</sup> The number of water molecules that need to be included explicitly in the model system is not an easy task. In this case, we employed the less number of water molecules that give convergence of the difference in Gibbs energy between **1** and **2**. Therefore, the “L-shaped”, **2'**, and “U-shaped”, **2**, conformers of the protonated substate are modelled including three explicit water molecules, **2'-w3** and **2-w3**, respectively. The **2-w3** is calculated to be 0.3 kcal/mol higher in Gibbs energy than the **2'-w3**, with a relative Gibbs energy of 19.2 kcal/mol (Figure 6.2).

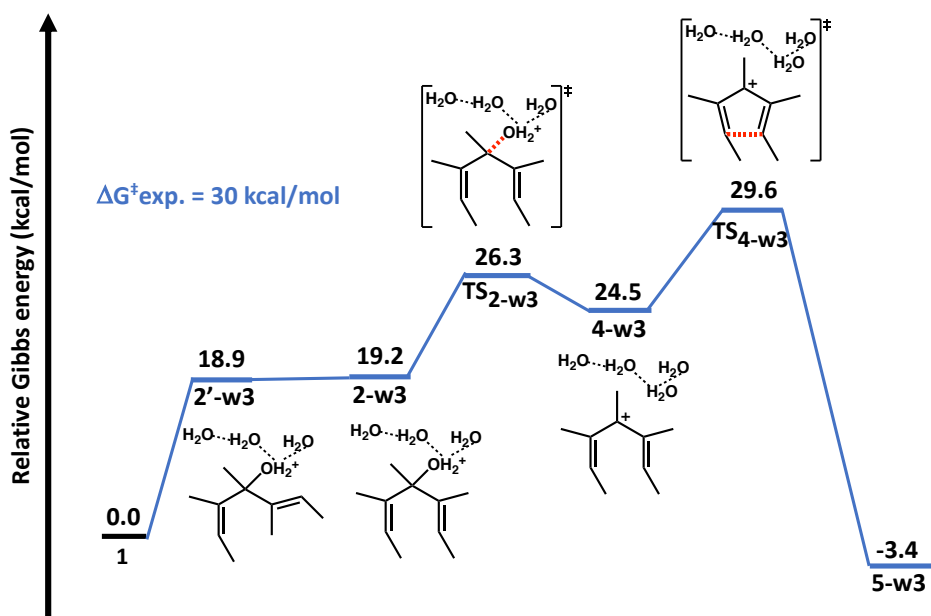


**Figure 6.2.** Gibbs energy profile of the Nazarov cyclization of 1,4-pentadien-3-ol in aqueous solution.

It is followed by the “water loss” from the protonated substrate. The transition state for this step, **TS<sub>2-w3</sub>**, is calculated to be 26.3 kcal/mol uphill

from the substrate, forming a pentadienyl carbocation intermediate, **4-w3**, which is 24.5 kcal/mol higher in Gibbs energy than the substrate. Their optimized structures are shown in Figure 6.3. The subsequent step is the electrocyclic ring closure, **TS<sub>4-w3</sub>**, which is calculated to have a Gibbs energy barrier of 29.6 kcal/mol from the substrate, in excellent agreement with the experimental value of 30.0 kcal/mol.<sup>2</sup> Overall, the reaction without the metallocage has a single rate determining step that is the electrocyclization in agreement with experimental observations.

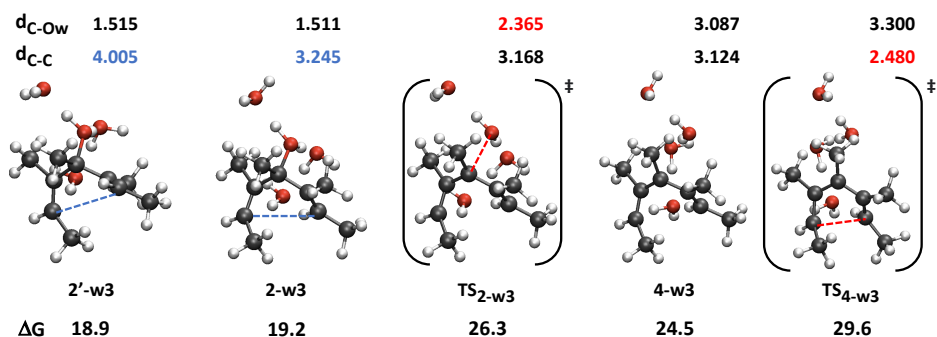


**Figure 6.3.** Optimized geometries of the protonated substrate, intermediate and transition states.

## 6.2. Reaction in the metallocage.

Experimental results have revealed that the reaction in the presence of metallocage proceeds with a rate acceleration of  $1.7 \cdot 10^6$  compared to that in solution; the same sequential steps in the reaction mechanism are expected.<sup>1,2</sup> We evaluated and analyzed the effect of the encapsulation on each of the reaction steps described previously trying to determine the contributions to the rate enhancement.

The encapsulation effect on the protonation step can be analyzed by examining either the protonation, **1** to **2**, and encapsulation of the protonated substrate by the metallocage, **2** to **2C3**, (blue arrows in Figure 6.4) or the encapsulation of the substrate, **1** to **1C3**, and its protonation inside the metallocage, **1C3** to **2C3**, (black arrows in Figure 6.4).

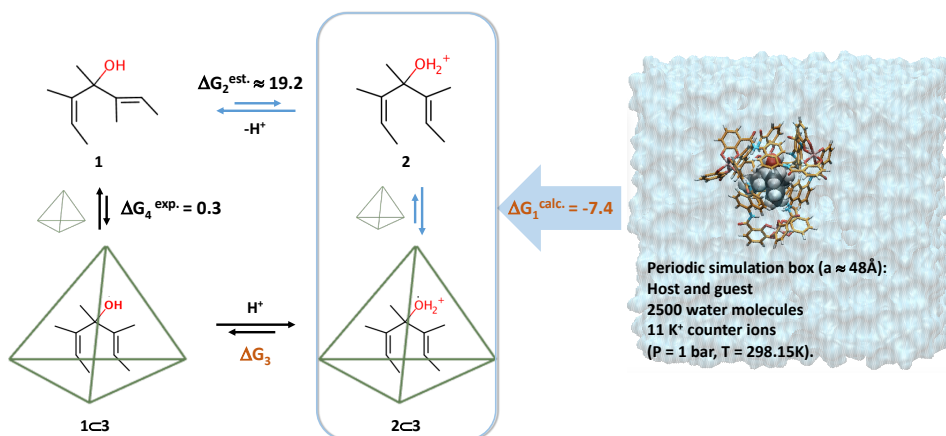


**Figure 6.4.** Thermodynamic cycle for the encapsulation of the protonated substrate in the  $[\text{Ga}_4\text{L}_6]^{12-}$ .

The binding Gibbs energy of **1** in the metallocage was determined experimentally to be 0.3 kcal/mol from the guest self-exchange rate of **1c3**, suggesting the protonation of **1** in the  $[\text{Ga}_4\text{L}_6]^{12-}$ .<sup>2</sup> Nevertheless, calculating the relative stability of **1c3** vs **2c3** ( $\Delta G_3$ , related to the pKa of the protonated substrate in the metallocage) can be inaccurate owing to the absence of numerical data measured for the solvation of proton in the  $[\text{Ga}_4\text{L}_6]^{12-}$ . Therefore, we evaluated the effect of the encapsulation on the protonated substrate by computing the binding Gibbs energy of **2** in the metallocage and using the thermodynamic cycle depicted in Figure 6.4. In this way, it can be calculated with a computational protocol validated against experimental data by a benchmarking study on the encapsulation of cationic guest molecules by the  $[\text{Ga}_4\text{L}_6]^{12-}$  discussed in the fourth chapter.<sup>9</sup> The binding Gibbs energy of **2** in the metallocage is calculated to be -7.4 kcal/mol. Thus, the formation of the protonated substrate in the metallocage  $\Delta G_3$ , is 11.5 kcal/mol ( $\Delta G_3 = \Delta G_2 + \Delta G_1 - \Delta G_4$ ) higher in Gibbs energy than the initial encapsulated substrate, **1c3**, (Figure 6.5).

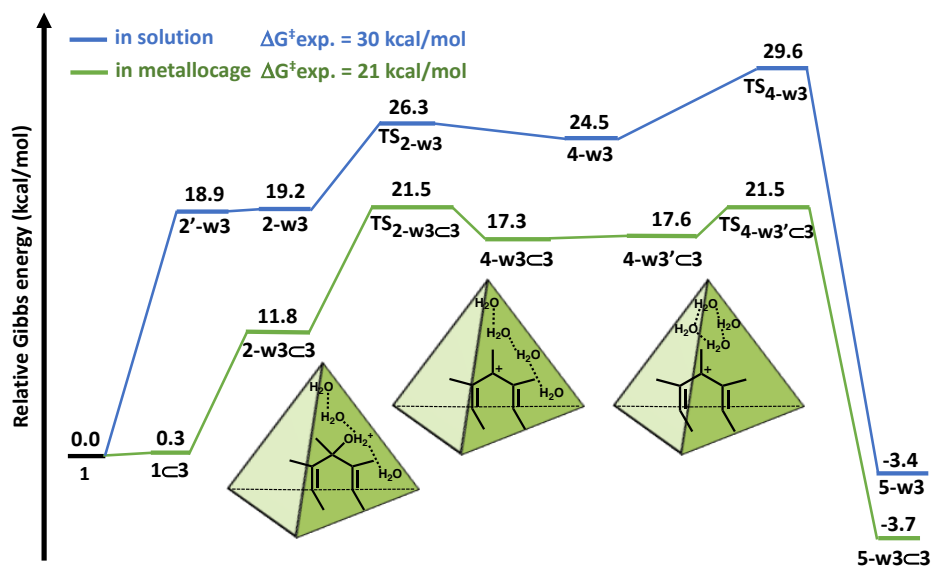


**Figure 6.5.** Gibbs energy profiles of the Nazarov cyclization of 1,4-pentadien-3-ol in the metallocage and in solution.

At this point, a classical molecular dynamic simulation of the protonated substrate encapsulated by the metallocage in explicit solvent was performed in order to determine the number of explicit water molecules in the metallocage. The simulation shows that there are three water molecules together with the protonated substrate in the metallocage. Based on this result, we continued our investigation of the encapsulated reaction at full QM level working on model systems, **species-w3c3**, that include three water molecules explicitly along with the substrate in the metallocage. In order to identify the most stable geometry, a conformational search was conducted by considering plausible conformers and configurations including different solvent arrangements and hydrogen bonding patterns. The calculations show that the “U-shaped” conformer of the protonated substrate is the most stable one in the metallocage. The calculated Gibbs energy differences between **2'-w3** (L-shaped) and **2-w3** (U-shaped) are 0.3 kcal/mol and  $-4.2$  kcal/mol without and with the metallocage respectively. Thus, the conformational equilibrium/relative stability of the protonated substrate is altered upon encapsulation.

The encapsulated protonated substrate, **2-w3c3**, evolves to water loss through transition state **TS<sub>2-w3c3</sub>**, which is calculated to be 21.5 kcal/mol higher in Gibbs energy compared to the substrate (Figure 6.5). It forms a host-guest intermediate **4-w3c3**; there is another configuration **4-w3'c3** with a different solvent rearrangement, needed for the subsequent step. Both configurations are very similar in Gibbs energy, whose values are 17.3 kcal/mol and 17.6 kcal/mol relative to the reactants (Figure 6.6).

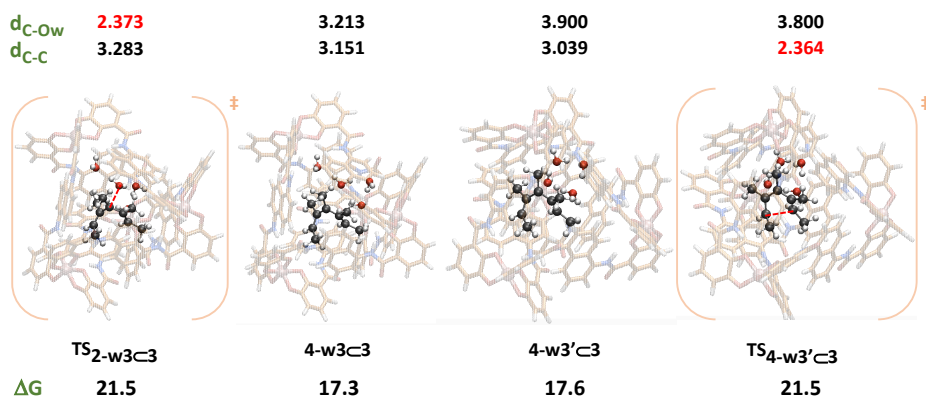


**Figure 6.6.** Optimized geometries of the encapsulated intermediates and transition states.

The ensuing step is the electrocyclization of the pentadienyl carbocation in the metallocage, which has the calculated Gibbs energy barrier of 21.5 kcal/mol from the substrate, **TS<sub>4-w3'c3</sub>**. These results show that the water loss and the electrocyclization are both rate limiting steps of the encapsulated reaction, in very good agreement with experiment. The overall calculated Gibbs energy barrier of 21.5 kcal/mol for the reaction in the metallocage also matches the experimental value of 21.0 kcal/mol.<sup>2</sup>

### 6.3. Origin of the catalysis and effect of the encapsulation.

The overall reduction of the Gibbs energy barrier of the reaction in the metallocage can be analyzed in terms of how intermediates and transition states are stabilized or destabilized upon encapsulation. The overall barrier

in solution is 29.6 kcal/mol whereas in the metallocage is 21.5 kcal/mol, showing a catalytic effect upon encapsulation.

The calculated relative Gibbs energy barriers of the non-encapsulated (without the metallocage) and encapsulated reactions (with the metallocage) are 10.7 kcal/mol (29.6-18.9) and 9.7 kcal/mol (21.5-11.8) from the corresponding protonated substrates, respectively (Figure 6.5). Thus, the actual stabilization of the barrier for the process by encapsulation once the substrate is protonated is rather low, -1.0 kcal/mol. The effect of the encapsulation on each of the two steps, water loss and electrocyclization is as follows:

(a) The transition state of the water loss from the protonated substrate has a Gibbs energy barrier of 7.1 kcal/mol and 9.7 kcal/mol in solution and in the metallocage, respectively. It is thus increased by 2.6 kcal/mol upon the encapsulation. Regarding the backward process, the water recombination, the barrier is also risen from 1.8 kcal/mol in solution to 4.2 kcal/mol in the metallocage, respectively. Therefore, the water loss step from the protonated substrate is destabilized by the encapsulation.

(b) The transition state of the electrocyclization has a Gibbs energy barrier of 5.1 kcal/mol and 3.9 kcal/mol from the carbocationic intermediate in solution and in the metallocage, respectively. Thus, this transition state is stabilized by 1.2 kcal/mol upon the encapsulation. It is interesting that both transition states are affected by the encapsulation, but in opposite manner. As far as the protonated substrate is concerned, the calculated binding Gibbs energy of the protonated substrate in the metallocage is -7.4 kcal/mol. Therefore, the relative Gibbs energy of this intermediate in the reaction profile for the encapsulated process decreases by this amount of energy. It turns out to be the main contribution to the overall decrease of the Gibbs energy barrier of the reaction in the metallocage, showing the importance of the cation-stabilizing ability of the  $[\text{Ga}_4\text{L}_6]^{12-}$  on this catalysis.

Furthermore, the possibility of involvement of other conformations of the substrate in the encapsulated reaction pathway is investigated by exploring the conformational Gibbs energy landscape of the pentadienyl carbocation, **4**, in the metallocage with an adaptively biased molecular dynamic (AMBER-NFE-ABMD) simulation.<sup>10-12</sup> It shows that the interconversion



between the “U-shaped”, **4**, and “L-shaped”, **4'**, conformers of the pentadienyl carbocation in the metallocage has a Gibbs energy barrier of more than 18 kcal/mol indicating that the overall Gibbs energy barrier of the reaction would exceed 30 kcal/mol. This shows that the only conformer of the substrate involved in the encapsulated reaction pathway is the “U-shaped” conformation which is the most stable one in the metallocage. Therefore, the preorganization of the substrate in the metallocage is found to be fundamental to this rate acceleration.

In conclusion, the Nazarov cyclization of 1,4-pentadien-3-ol encapsulated by the supramolecular organometallic cage,  $[\text{Ga}_4\text{L}_6]^{12-}$ , originates from the substrate preorganization and proceeds with selected transition state and intermediate stabilizations. The formation of the first cationic intermediate, the protonated substrate, is stabilized by 7.4 kcal/mol upon encapsulation and afterwards the rate determining transition state which is the electrocyclization is slightly stabilized by 1.0 kcal/mol. Notwithstanding these stabilizations, the reverse effect on the transition state of the water loss from the protonated substrate arises upon encapsulation. In essence, the cation-stabilizing ability featured by the metallocage is at the core of this host-guest catalysis.

## References:

- (1) Hastings, C. J.; Pluth, M. D.; Bergman, R. G.; Raymond, K. N. Enzymelike Catalysis of the Nazarov Cyclization by Supramolecular Encapsulation. *J. Am. Chem. Soc.* **2010**, *132*, 6938–6940.
- (2) Hastings, C. J.; Bergman, R. G.; Raymond, K. N. Origins of Large Rate Enhancements in the Nazarov Cyclization Catalyzed by Supramolecular Encapsulation. *Chem. Eur. J.* **2014**, *20*, 3966–3973.
- (3) Siegbahn, P. E. M.; Crabtree, R. H. Modeling the Solvent Sphere: Mechanism of the Shilov Reaction. *J Am Chem Soc*, **1996**, *118*, 4442–4450.
- (4) Díez, J.; Gimeno, J.; Lledós, A.; Suárez, F. J.; Vicent, C. Imidazole Based Ruthenium(IV) Complexes as Highly Efficient Bifunctional Catalysts for the Redox Isomerization of Allylic Alcohols in Aqueous Medium: Water as Cooperating Ligand. *ACS Catal*, **2012**, *2*, 2087-2099.
- (5) Pavlova, A.; Rösler, E.; Meijer, E. J. Mechanistic Aspects of Using Formate as a Hydrogen Donor in Aqueous Transfer Hydrogenation. *ACS Catal*, **2016**, *6*, 5350–5358.
- (6) Bryantsev, V. S.; Diallo, M. S.; Goddard, W. A. Calculation of Solvation Free Energies of Charged Solutes Using Mixed Cluster/Continuum Models. *J. Phys. Chem. B* **2008**, *112*, 9709–9719.
- (7) Daver, H.; Algarra, A. G.; Rebek Jr., J.; Harvey, J. N.; Himo, F. Mixed Explicit-Implicit Solvation Approach for Modeling of Alkane Complexation in Water-Soluble Self-Assembled Capsules. *J. Am. Chem. Soc.* **2018**, *140*, 12527–12537.
- (8) Kelly, C. P.; Cramer, C. J.; Truhlar, D. G. Adding Explicit Solvent Molecules to Continuum Solvent Calculations for the Calculation of Aqueous Acid Dissociation Constants. *J. Phys. Chem. A* **2006**, *110*, 2493–2499.
- (9) Norjmaa, G.; Vidossich, P.; Maréchal, J.-D.; Ujaque, G. Modeling Kinetics and Thermodynamics of Guest Encapsulation into the  $[M_4L_6]^{12-}$  Supramolecular Organometallic Cage. *J. Chem. Inf. Model.* **2021**, *61*, 4370–4381.
- (10) Babin, V.; Roland, C.; Sagui, C. Adaptively Biased Molecular Dynamics for Free Energy Calculations. *J. Chem. Phys.* **2008**, *128*, 134101.
- (11) Babin, V.; Karpusenka, V.; Moradi, M.; Roland, C.; Sagui, C.

- Adaptively Biased Molecular Dynamics: An Umbrella Sampling Method with a Time-Dependent Potential. *Int. J. Quant. Chem.* **2009**, *109*, 3666-3678.
- (12) Moradi, M.; Babin, V.; Roland, C.; Sagui, C. The Adaptively Biased Molecular Dynamics Method Revisited: New Capabilities and an Application. *J. Phys. Conf. Ser.* **2015**, *640*, 012020.

## Chapter 7.

### General conclusions.

In this thesis, computational methods including molecular dynamics simulations and quantum chemical calculations have been employed to investigate supramolecular catalysis. Encapsulation and catalytic reactions carried out over the  $[\text{Ga}_4\text{L}_6]^{12-}$  metallocage were investigated. In particular, the encapsulation process for several cationic guests were studied, and the C-C bond formation from Au(III) and Pt(IV) complexes, as well as the Nazarov reaction in solution and encapsulated were investigated.

In the first part, the binding affinities determined experimentally for a set of cationic guest molecules encapsulated by the  $[\text{Ga}_4\text{L}_6]^{12-}$  are numerically reproduced by classical molecular dynamic simulations based on APR method with an absolute error of up to ca. 2.0 kcal/mol. A parametrization procedure for deriving non-standard parameters (for the metal atoms) is proposed; deriving those parameters from calculations in solution turned out to be crucial to obtain accurate binding energies.

For the  $[\text{Ga}_4\text{L}_6]^{12-}$ -catalyzed alkyl-alkyl reductive eliminations from Au(III) and Pt(IV) complexes, the analysis of the rate acceleration is performed in terms of microsolvation and encapsulation terms. Microsolvation effects are found to be different for these two metal complexes, becoming much larger for Au(III) complexes than for Pt(IV) complex. A decomposition analysis is performed on the encapsulation term; thus, it is analyzed in based on strain and interaction terms. The interaction between the metal complex and metallocage is the main contribution to the rate acceleration upon encapsulation. Moreover, encapsulated complexes may include solvent molecules. A significant influence of the encapsulated solvent molecules is disclosed showing that the smaller number of solvent molecules encapsulated, the larger electronic contribution to the rate enhancement. The overall reduction of the Gibbs energy barrier is comparable for both metal complexes, but their

contribution in terms of microsolvation and encapsulation is quite different.

For the  $[\text{Ga}_4\text{L}_6]^{12-}$ -catalyzed Nazarov cyclization, several factors as the pre-organization of the substrate and the protonation are fundamental to this catalysis. Encapsulation induces pre-organization of the substrate, with the U-shaped pro-reactive form stabilized over the L-shaped form, conversely to solution. The protonation of the substrate is substantially stabilized by the  $[\text{Ga}_4\text{L}_6]^{12-}$  indicating a shift of the basicity of the alcohol substrate over encapsulation in the  $[\text{Ga}_4\text{L}_6]^{12-}$ . The shift of the basicity of the alcohol substrate in the  $[\text{Ga}_4\text{L}_6]^{12-}$  is the main factor in the observed rate enhancement. Regarding the effect of encapsulation on the water loss and cyclization steps, the first slightly increases the barrier whereas the second is stabilized, compared to solution. This shows that both are rate determining steps, in very good agreement with experiment.

Overall, we can conclude that the use of computational methods is a relevant tool for the understanding and elucidating of mechanisms of metallocage-involved catalytic processes.



